

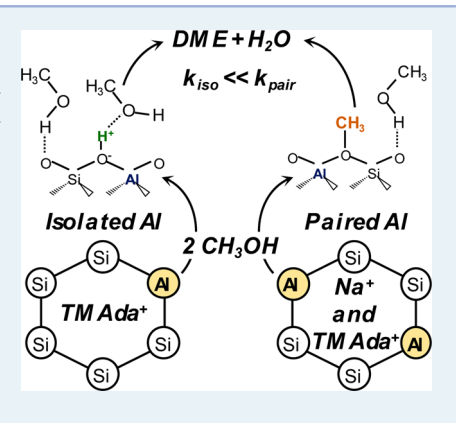
Introducing Catalytic Diversity into Single-Site Chabazite Zeolites of Fixed Composition via Synthetic Control of Active Site Proximity

John R. Di Iorio, Claire T. Nimlos, and Rajamani Gounder*

Charles D. Davidson School of Chemical Engineering, Purdue University, 480 Stadium Mall Drive, West Lafayette, Indiana 47907, United States

Supporting Information

ABSTRACT: We report a synthesis-structure-function relation describing how different routes to crystallize single tetrahedral-site (T-site) zeolites of fixed composition lead to different arrangements of framework Al atoms and, in turn, of extraframework proton active site ensembles that markedly influence turnover rates of a Brønsted acid-catalyzed reaction. Specifically, synthetic routes are reported that result in systematic changes in the arrangement of aluminum atoms (Al–O(–Si–O)_x–Al) in isolated (x > 2) and paired (x = 1, 2) configurations within chabazite (CHA) zeolite frameworks of effectively fixed composition (Si/Al = 14–17). Precursor solutions containing different structure-directing agents and aluminum sources crystallize CHA zeolites with one organic N,N,N-trimethyl-1-adamantylammonium cation occluded per CHA cage, and with amounts of occluded Na⁺ cations that increase linearly with paired framework Al content (0–44%). Ammonia and divalent cobalt ion titrations are used to quantify total and paired Brønsted acid sites, respectively, and normalize rates of methanol dehydration to dimethyl ether. First-



order and zero-order methanol dehydration rate constants (per H^+ , 415 K) systematically increase with the fraction of paired protons in CHA zeolites and are ~10× higher at paired protons. Such behavior reflects faster dissociative (surface methoxymediated) pathways that prevail at paired protons over slower associative (methanol dimer-mediated) pathways at isolated protons, consistent with *in situ* infrared spectra. These findings demonstrate that zeolites of fixed elemental composition, even when crystalline frameworks contain one unique T-site, can exhibit catalytic diversity when prepared via different synthetic routes that influence their atomic arrangements.

KEYWORDS: zeolite, Al distribution, synthesis, methanol dehydration, Brønsted acid catalysis, in situ IR spectroscopy

1. INTRODUCTION

In a landmark contribution to catalysis by aluminosilicate zeolites, Haag and co-workers reported that hexane cracking rates (per g, 811 K) increased linearly with total Al density (per g) in MFI, a low-symmetry framework containing 12 (orthorhombic) or 24 (monoclinic) unique tetrahedral sites (T-sites). This report suggested that MFI zeolites contained a single type of active Brønsted acid site (H+), whose catalytic behavior was independent of composition (Si/Al = 10-10000) and topographic location, as would be expected for a single-site catalyst.² Turnover rates and selectivities of hydrocarbon reactions have since been recognized to depend on the location of H⁺ sites within a given zeolite framework, despite similarities in their acid strength described rigorously by deprotonation energy (DPE),³ because the topology of microporous cavities influences the Gibbs free energies of confined intermediates and transition states through van der Waals interactions.⁴ Efforts to deconvolute the catalytic behavior of active sites located within different voids of a given zeolite have required either preferential titration of protons within certain voids or acquisition of zeolites of different provenance, a viable strategy because Al incorporation within specific T-sites during crystallization is difficult to control, other than in a few

emerging cases (FER, ⁵ MFI⁶). The catalytic consequences of T-site location within such zeolites may be further convoluted by effects of site proximity, which is determined by atomic arrangements that are difficult to control systematically and independently of bulk composition.⁷

Distinct ensembles of proton active sites in a zeolite arise from differences in the arrangement $(Al-O(-Si-O)_x-Al)$ of framework Al atoms (Al_f) between isolated (x>2) or paired configurations (x=1,2), with the latter identified functionally by their ability to exchange divalent cations. Proton proximity effects on catalysis have been studied in MFI zeolites by varying their bulk composition (Si/Al), and turnover rates (per H⁺) of hydrocarbon cracking are generally reported to increase with total Al content (Al_{tot}) . Changes in bulk composition only influence Al proximity *on average*, however, given that framework Al arrangements show nuanced dependences on the conditions and reagent sources used during zeolite crystallization. As a result, the routes used to synthesize MFI zeolites influence framework Al arrangement, but in a manner

Received: April 20, 2017 Revised: August 16, 2017 Published: August 17, 2017

6663

Table 1. Characterization Data and Methanol Dehydration Rate Constants for CHA Zeolites Synthesized at Different Compositions and with Different Fractions of Paired Al Sites in OH⁻ and F⁻ Media, and Kinetic Data Estimated for Isolated and Paired Protons

Synthetic Details							ngement	Rate Co (415	
Sample ^a	Si/Al _f	H^+/Al_f^b	Organic Content/wt % ^c	Crystal Size/ μ m ^d	Occluded Na ⁺ /Al _{tot} ^e	Al _{iso} /Al _{tot}	Al _{pair} /Al _{tot}	$k_{ m first}^{\ \ g}$	$k_{\rm zero}^{h}$
CHA-OH(14,0%)	14	0.95	18.4	2	< 0.01	1.00	0.00	22 ± 4	14 ± 2
CHA-OH(17,0%)	17	1.00	22.5	2	< 0.01	1.00	0.00	23 ± 4	12 ± 2
CHA-OH(27,0%)	27	1.00	21.3	6	< 0.01	1.00	0.00	9 ± 2^{i}	11 ± 2
CHA-F(18,0%)	18	1.02	22.9	1	< 0.01	1.00	0.00	24 ± 4	13 ± 2
CHA-OH(16,6%)	16	0.93	n.m.*	0.8	n.m.*	0.94	0.06	22 ± 3	25 ± 4
CHA-OH(15,18%)	15	1.01	21.6	1	0.05	0.82	0.18	36 ± 7	28 ± 4
CHA-OH(16,24%)	16	1.16^{j}	20.1	1	n.m.*	0.76	0.24	32 ± 8	22 ± 2
CHA-OH(17,30%)	17	0.97	21.0	1	0.25	0.70	0.30	40 ± 8	34 ± 8
CHA-OH(14,44%)	14	1.00	19.8	0.3	0.26	0.56	0.44	85 ± 17	40 ± 6
Isolated protons ^k	-	-	-	-	-	-	-	18	16
Paired protons ^k	-	-	-	-	-	-	-	130	70

"As explained in Section 4.2, samples are referred to by [countercation] – [framework] – [mineralizing agent] (Si/Al_f, % paired Al). Error in H⁺/Al_f from NH₃ TPD experiments is ± 0.05 . Expected organic content for one TMAda⁺ per CHA cage: 22.7 wt %. Estimated from SEM micrographs. Error in crystal diameter is ± 0.5 μ m. Na/Al_{tot} retained on the synthesized zeolite product. Error in Na⁺/Al_{tot} values is 12%. Ferror in Al_{iso}/Al_{tot} and Al_{pair}/Al_{tot} is 10%. Units of k_{first} : 10⁻³ mol DME (mol H⁺ s kPa)⁻¹. Error determined from least-squares regression for each sample. Units of k_{zero} : 10⁻³ mol DME (mol H⁺ s)⁻¹. Error determined from least-squares regression for each sample. Values of k_{first} for CHA–OH(27,0%) are corrupted by intraparticle mass transfer. H⁺/Al_{tot} = 1.02 for CHA–OH(16,24%), suggestive of reversible Al structural changes upon hydration to acquire NMR spectra. First-order and zero-order methanol dehydration rate constants on isolated and paired protons in CHA zeolites predicted from Figure 6. *n.m., not measured.

that is neither randomly determined nor prescribed by any deterministic rules. Thus, while the pairing of protons in MFI (Si/Al = 13–140) has been proposed to increase alkene oligomerization and alkane cracking turnover rates, concomitant changes in Al distribution among different T-sites and void environments (i.e., straight and sinusoidal channels, and their intersections) have precluded unambiguous kinetic assessments of proton proximity in MFI zeolites.

Here, we focus on the chabazite (CHA) topology, a highsymmetry framework containing a single crystallographically unique T-site. The CHA framework contains double sixmembered ring building units that interconnect to form eightmembered ring windows (0.38 nm diam.), which limit diffusion into larger cavities (1.2 nm \times 0.72 nm \times 0.72 nm; 12 T atoms per CHA cage). The presence of a single T-site in the CHA framework promises to clarify how synthesis routes influence Al proximity independent of T-site location and, in turn, how proton proximity can influence Brønsted acid catalysis. First, we extend methods to synthesize CHA zeolites of effectively fixed composition (Si/Al = 14-17), but with systematically varying framework Al arrangements that span the limit of site isolation (0% paired Al) to nearly half of the sites (44%) in paired configurations. Then, we use seven CHA samples with varying paired Al content to show that first-order and zero-order rate constants (per total H⁺, 415 K) for the Brønsted acid-catalyzed methanol dehydration to dimethyl ether (DME) are nearly one order of magnitude larger on paired than on isolated protons. IR spectra measured during steady-state dehydration catalysis enable direct observation of surface methoxy species (~1457 cm⁻¹),¹⁵ providing evidence that paired protons in CHA zeolites can access alternate methanol dehydration pathways that do not propagate at isolated protons under these conditions. These results constitute a synthesis-structurefunction relation for proton proximity effects in CHA zeolites, and they demonstrate that catalytic diversity can arise from differences in the atomic arrangement of active sites in single Tsite zeolites of fixed composition.

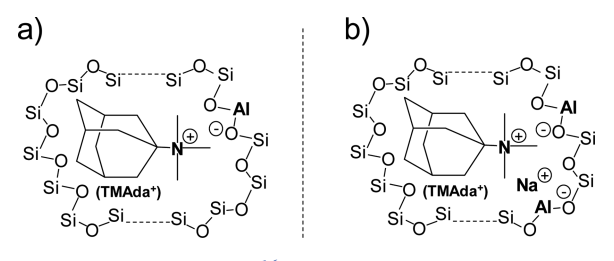
2. RESULTS AND DISCUSSION

2.1. Synthesis of CHA zeolites with different Al arrangements. We recently reported that structure-directing agents (SDAs) of different cationic charge density can be used to systematically change the distribution of isolated and paired framework Al atoms in CHA zeolites (SSZ-13).16 Proximal protons that compensate paired Al sites were quantified by measuring Co²⁺ exchange isotherms, which were validated by (i) collecting UV-visible spectra that showed Co²⁺ d-d transitions (~19,500 cm⁻¹) with undetectable cobalt oxide formation, (ii) quantifying residual H⁺ sites after Co²⁺ exchange using NH₃ titration methods (2 H⁺ replaced per Co²⁺), and (iii) quantifying paired Al sites with another divalent cation (Cu²⁺)¹⁶ predicted by density functional theory to selectively titrate paired Al sites in CHA frameworks (i.e., arrangements of 2 Al in a 6-MR).¹⁷ The use of chemical titrants that directly probe the functional behavior of proximal protons, and directly quantify such sites, avoids inaccuracies in assessing the proximity of their structural surrogates. Although framework Al proximity in zeolites can be probed by NMR techniques, Al separated by one or two Si atoms in certain frameworks (e.g., MFI) can lead to protons stabilized within different voids, which do not function as proximal protons within the same void environment.

Here, we extend previously reported synthetic methods to prepare CHA zeolites of effectively fixed composition (Si/Al $_{\rm f}$ = 14–17) with nearly half of their Al atoms (44%) in paired configurations. Unless otherwise specified, each zeolite contained nearly complete Al incorporation within framework locations (Al $_{\rm f}$ /Al $_{\rm tot}$ > 0.95; 27 Al MAS NMR, Section S.2, Supporting Information), and compensating H $^{+}$ sites present in similar amounts (H $^{+}$ /Al $_{\rm f}$ > 0.95 by NH $_{3}$ titration, Table 1). Relevant characterization data for CHA zeolites are summarized in Table 1, with all characterization data and detailed methods provided in Section S.2 of the Supporting Information.

CHA zeolites containing predominantly isolated Al atoms, which are unable to exchange divalent cations (e.g., Co²⁺, Cu²⁺) but can quantitatively exchange monovalent cations (e.g., H⁺, Na⁺, NH₄⁺), were crystallized at different compositions (Si/Al = 15-30) in the presence of organic N,N,N-trimethyl-1adamantylammonium cations (TMAda+) as the sole SDA and hydroxide as the counteranion.¹⁶ The ability of TMAda+ cations to isolate framework Al atoms in CHA was verified by seven replicate crystallization experiments. 16 The adamantyl group (~0.7 nm diam.) imposes steric constraints that limit occupation of each CHA cage (0.72 nm diam.) by only one TMAda+ molecule (Table 1, TGA experiments detailed in Section S.2, Supporting Information), 18 while the single cationic charge at the quaternary ammonium center imposes electrostatic constraints that direct placement of one anionic framework Al center (Scheme 1a).

Scheme 1. Schematic Representation of the Organization of Si and Al Atoms in the Crystallizing Polyanionic CHA Framework To Form (a) Isolated Al with Only TMAda⁺ or (b) Paired Al in the Presence of TMAda⁺ and Na^{+a}



^aAdapted from Di Iorio et al. ¹⁶

Despite the occlusion of a single TMAda+ molecule within each CHA cage, the bulk compositions of the crystallized zeolites do not reflect the incorporation of 1 Al atom per cage (Si/Al = 11; 12 T atoms per cage), indicating that anionic lattice defects (Si-O⁻) form to compensate cationic charges of some TMAda+ molecules. CHA zeolites crystallized within a limited composition range (Si/Al = 15-30) in hydroxide media, reflecting crystallization barriers imposed by a disparity in Coulombic interactions between occluded TMAda+ cations and the solid aluminosilicate polyanion. 20 TMAda+ alone is unable to stabilize CHA frameworks with high Al density (Si/ Al_f < 11) because each cage (12 T atoms) contains one occluded TMAda+ cation.18 TMAda+ is also ineffective at stabilizing CHA frameworks with low Al density (Si/Al_f > 30) because anionic lattice defects are required to form in order to balance excess cationic charges introduced by occluded cationic SDA molecules.²¹ The electrostatic balance between occluded cations and anionic framework Al centers implies that using different mineralizers (OH-, F-), which facilitate reversible formation of Si-O and Al-O bonds during crystallization,² should not influence framework Al arrangement within this composition range (Si/Al = 15-30). This hypothesis was tested by preparing precursor solutions in fluoride media containing TMAda+ as the sole SDA. These solutions crystallized CHA zeolites (Si/Al=18) that were also unable to exchange Co²⁺ (details in Section S.2, SI), demonstrating the ability of TMAda+ cations to direct the incorporation of isolated framework Al atoms in CHA zeolites within this composition range (Si/Al = 15-30), irrespective of the counteranion used as the mineralizer (OH⁻, F⁻).

CHA zeolites of fixed composition, but with systematically varying fractions of paired Al, were synthesized by varying the ratio of high (Na⁺) and low (TMAda⁺) charge density cations in the precursor solution, at fixed total cation content ((Na⁺+TMAda⁺)/Al). Our previous synthesis experiments used the same aluminum source (Al(OH)₃) and resulted in CHA zeolites (Si/Al = 14–16) with varying percentages of paired Al (0–18%) that correlated linearly with the total amount of Na⁺ retained on the crystallized zeolite product (Figure 1). This correlation suggests that a second anionic

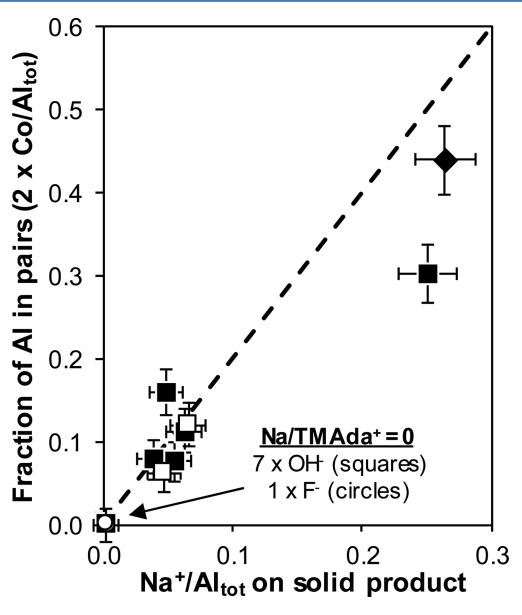


Figure 1. Fraction of Al in pairs as a function of Na⁺ retained on CHA products of fixed composition (Si/Al_f = 14–18) crystallized in OH⁻ (squares) media with Na⁺/TMAda⁺ ≤ 1 (filled), Na⁺/TMAda⁺ > 1 (open), and F⁻ (open circle) media using Al(OH) $_3$ and Al(O-i-Pr) $_3$ (diamond) as aluminum sources. The dashed line represents the parity line (slope = 2) expected if each Na⁺ cation formed a paired Al site. Eight independent CHA samples crystallized using only TMAda⁺ are plotted at the origin.

framework Al center, compensated by an extraframework Na⁺ cation, is incorporated proximal to a framework Al center compensating the ammonium group in a TMAda+ cation occluded within a CHA cage, an assembly that preserves dispersive contacts between nonpolar siloxane portions of the zeolite framework and the hydrophobic adamantyl group of TMAda⁺ (Scheme 1b). Al precursors that differ in reactivity and dissolution rate 11 have been used to influence Al pairing in MFI zeolites crystallized from solutions containing TPA+ cations, although without a discernible dependence on a single synthesis parameter and also often resulting in changes to bulk composition (Si/Al = 25-60). Therefore, we attempted to vary paired Al content further by crystallizing CHA using other Al sources (AlCl₃, Al(NO₃)₃, NaAlO₂, Al₂O₃, Al(O-i-Pr)₃) in hydroxide media with equimolar amounts of Na⁺ and TMAda⁺, holding other synthesis parameters constant. Most samples contained proton fractions (H+/Al < 0.6) or micropore volumes (<0.14 cm³ g⁻¹) that were abnormally low (data in Section S.2, Supporting Information), except those synthesized using Al(O-i-Pr)₃ (Si/Al_f = 14, 0.16 cm³ g⁻¹, H⁺/Al_f = 1.00, Table 1). This CHA zeolite contained more than twice the paired Al content (44%) as reported previously for CHA (Si/Al = 15) synthesized using Al(OH)₃, ¹⁶ yet also incorporated a

larger amount of Na^+ during synthesis ($Na^+/Al_{tot} = 0.26$, Figure 1).

Taken together, these results suggest that the amount of Na⁺ retained on CHA zeolite products, when crystallized from mixtures of low charge density organic TMAda+ cations and high charge density inorganic Na+ cations, can serve as a predictive descriptor of the number of paired Al sites formed (Figure 1). This synthesis-structure relation is particularly useful given the stochastic nature of zeolite crystallization that can form nonuniform products upon replication of the same procedure. Indeed, two replicate crystallizations of CHA zeolites using Al(OH)₃ as the aluminum source (Na⁺/ TMAda⁺ = 1) led to detectable variations in paired Al content (18–30%), but which also correlated with the Na⁺ incorporated into the crystalline product (Figure 1). These findings support the hypothesis that Na+ becomes occluded in extraframework locations proximal to the cationic charge in TMAda+, so as to direct the formation of paired framework Al. 16 They also indicate that the cationic charge density of occluded SDA molecules influences the anionic charge density introduced by Al3+ substitution within pure-silica zeolite lattices, concepts related to those proposed in charge density mismatch theory. 20,23,24

The methods to prepare this suite of CHA zeolites represent progress toward predictive synthetic control of active site arrangement, and the resulting materials can be used as model catalysts to facilitate connections between structure and function in zeolite catalysis. The CHA zeolites containing only isolated Al atoms at varying composition should behave as single-site catalysts, promising to clarify experimental kinetic and spectroscopic assessments of proton active sites by experiment, which can be modeled more faithfully by theory. The CHA zeolites of fixed composition but varying paired Al content enable studying the catalytic consequences of proton proximity in zeolites, independent of structural heterogeneities arising from the multiplicity of T-sites. As discussed next, a structure-function relation is developed for isolated and paired protons in CHA zeolites using methanol dehydration to dimethyl ether (DME), a versatile probe reaction of the intrinsic acid strength and reactivity of solid Brønsted acids.²⁵

2.2. Methanol dehydration to dimethyl ether: a Brønsted acid probe reaction. The dehydration of methanol to dimethyl ether can proceed through two different pathways on solid Brønsted acids, as reported in detail by Carr et al.25 The associative dehydration pathway involves adsorption of gas-phase methanol at a H⁺ site to form a hydrogen-bonded methanol monomer (Step 1, Scheme 2). Adsorption of a second methanol forms a protonated methanol dimer, in which the proton is solvated away from the zeolite lattice and coordinated between the two nucleophilic oxygen atoms (Step 2, Scheme 2). Protonated dimers can rearrange to form an intermediate (Step 3, Scheme 2) that can decompose into water and an adsorbed dimethyl ether species (Step 4, Scheme 2), which desorbs to regenerate the H⁺ site (Step 5, Scheme 2). Methanol monomers and protonated dimers are the most abundant reactive intermediates (MARI) under experimental conditions investigated previously on mediumpore and large-pore zeolites (10-MR and larger) and polyoxometallate clusters (433 K, >0.2 kPa CH₃OH),²⁵ resulting in the following rate expression (full derivation in Section S.3, Supporting Information):

Scheme 2. Elementary Steps in the Associative Methanol Dehydration Pathway^a

^aAdapted from Carr et al.²⁵

$$r_{DME,A} = \frac{k_{first,A} P_{CH_3OH}}{1 + \frac{k_{first,A}}{k_{zero,A}} P_{CH_3OH}}$$
(1)

In eq 1, $k_{\rm first,A}$ and $k_{\rm zero,A}$ are apparent first-order and zero-order rate constants, respectively, for the associative methanol dehydration pathway.

Alternatively, the dissociative dehydration pathway involves formation of methanol monomers (Step 1, Scheme 3), which initially eliminate water to form a surface methoxy group (Step 2, Scheme 3). Adsorption of a second methanol at an adjacent framework oxygen forms a surface methanol-methoxy pair (Step 3, Scheme 3). Addition of the surface methoxy to the nucleophilic oxygen atom of the coadsorbed methanol forms an adsorbed dimethyl ether species (Step 4, Scheme 3), which desorbs to regenerate the H⁺ site (Step 5, Scheme 3). An additional step involving formation of methanol dimers (Step 2, Scheme 2) inhibits the formation of surface methoxy groups that propagate the dissociative cycle.

The assumption of methanol monomers, protonated dimers, and surface methoxy-methanol pairs as MARI leads to the following rate expression, which predicts that rates become inhibited at high methanol pressures (full derivation in Section S.3, Supporting Information):

$$r_{DME,D} = \frac{k_{first,D} P_{CH_3OH}}{1 + \frac{k_{first,D}}{k_{zero,D}} P_{CH_3OH} + \frac{k_{first,D}}{k_{inhibit,D}} P_{CH_3OH}^2}$$
(2)

In eq 2, $k_{\rm first,D}$ and $k_{\rm zero,D}$ are first-order and zero-order rate constants, respectively, for the dissociative dehydration pathway, and $k_{inhibit,D}$ is an inhibition rate constant that reflects formation of an unreactive methanol dimer.

In situ IR spectra of H-MFI during steady-state methanol dehydration catalysis (433 K, 0.2–16 kPa CH₃OH) do not show deformation modes for surface methoxy species (~1457

Scheme 3. Elementary Steps in the Dissociative Methanol Dehydration Pathway^a

^aAdapted from Carr et al.²⁵

cm⁻¹) involved in the dissociative pathway, yet show hydrogenbonding modes for adsorbed CH₃OH monomers (~2380 cm⁻¹) and protonated CH₃OH dimers (~2620 cm⁻¹) involved in the associative pathway. 15 Further, periodic density functional theory (DFT) calculations indicate that DME formation proceeds with lower free energy barriers via the associative pathway on isolated H⁺ sites in MFI zeolites (by ~ 50 kJ mol⁻¹, vdW-DF functional).²⁷ Kinetic measurements were benchmarked in this study by comparing values for three commercially sourced H-MFI samples (Zeolyst) to literature reports (details in Section S.3, Supporting Information). 15,26 Methanol dehydration rates on H-MFI (per H⁺, 415 K) increased linearly (<1 kPa) and became invariant (>15 kPa) with increasing methanol pressure, as predicted by the associative dehydration rate expression (eq 1). Moreover, first-order and zero-order rate constants (Figure 2) and apparent activation enthalpies and entropies (Section S.3, Supporting Information) agreed quantitatively with literature values. 15 The equivalence of measured rate constants, and specifically activation enthalpies and entropies in both kinetic regimes, indicates that the dehydration turnover rates measured here on MFI zeolites (per H+, 415 K) are measurements of equivalent catalytic phenomena reported by Jones et al. 15,26 Such quantitative kinetic benchmarking, in turn, validates the direct comparison of dehydration rate data reported here for MFI and CHA zeolites (at 415 K) to literature precedent.²⁸

2.3. Methanol dehydration catalysis on CHA zeolites containing only isolated H⁺ sites. Methanol dehydration rates on H-CHA zeolites were measured under differential conversion, reflected in DME formation rates (per H⁺) that were invariant with space velocity at fixed methanol pressure (Section S.5, Supporting Information). The presence of internal mass transport phenomena was investigated by performing a Koros–Nowak test²⁹ on CHA zeolites containing only isolated protons with varying framework Al composition (Si/Al_f = 14–

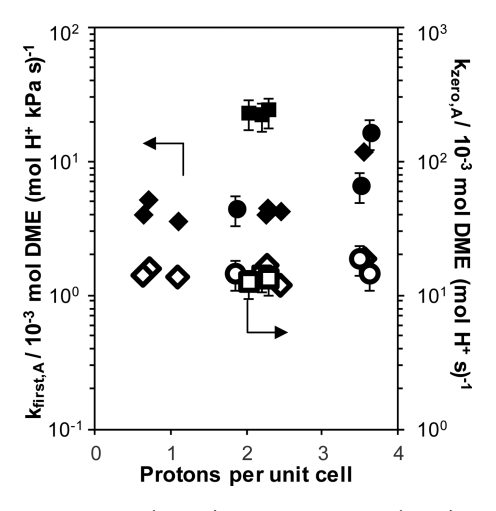


Figure 2. First-order (closed) and zero-order (open) associative methanol dehydration rate constants (per H^+) as a function of H^+ density (per unit cell) on H-zeolites. Data shown for H-CHA samples crystallized in OH^- and F^- media (Si/Al = 14-18) to contain only isolated protons at 415 K, (squares), for commercial H-MFI samples (Si/Al = 17-43, Zeolyst) at 415 K (circles), and for H-MFI samples (Si/Al = 17-120, inclusive of commercial Zeolyst samples) reported by Jones et al. ²⁶ at 433 K (diamonds).

27). Zero-order rate constants (per H⁺, 415 K) were similar (within 20%; Table 1) on CHA zeolites containing only isolated H⁺ sites but varying Al content (Si/Al_f = 14-27), as expected for a kinetic regime in which active sites are saturated with reactant-derived intermediates and thus insensitive to intraparticle gradients in reactant concentration. In contrast, first-order rate constants (per H⁺, 415 K) decreased with decreasing H⁺ site concentration (Table 1), behavior contrary to that predicted by the Koros-Nowak criterion for intraparticle reactant diffusion limitations.²⁹ These results suggest that intraparticle transport may become more restricted in CHA zeolites with lower Al content, which has been reported previously to lead to concomitant increases in crystallite size.³⁰ Indeed, SEM micrographs and dynamic light scattering measurements (Section S.2, Supporting Information) indicate that crystallite sizes increase from 1.5 to 6 μ m (Table 1) with decreasing Al content ($Si/Al_f = 14-27$) among the samples studied here. Figure 3 shows the intraparticle effectiveness factor (η) for a first-order reaction in a spherical pellet as a function of the Thiele modulus (ϕ) , with values estimated for these CHA zeolites (details and derivation of Thiele moduli and effectiveness factors in Section S.5, Supporting Information). CHA zeolites with Si/Al_f = 14-18 (ϕ = 0.7-0.9) are characterized by effectiveness factors near unity ($\eta = 0.9-1.1$), indicating that intraparticle concentration gradients are absent and that rates measured on these samples are kinetic in origin. CHA zeolites with $Si/Al_f = 27$ ($\phi = 3.5$), however, are characterized by effectiveness factors below unity ($\eta = 0.5$), indicating that intraparticle transport processes corrupt rates measured on this sample; thus, it was not studied further.

Methanol dehydration rates on isolated protons in H-CHA (per H^+ , 415 K) increased linearly (<1 kPa) before reaching a maximum and ultimately decreasing (>10 kPa) with increasing methanol pressure (Figure 4 and Section S.3, Supporting Information), in contrast with the behavior observed on H-MFI. Reversible inhibition observed at high pressures (>10 kPa) cannot be accounted for by the dissociative pathway, as isolated protons in H-CHA zeolites do not stabilize surface

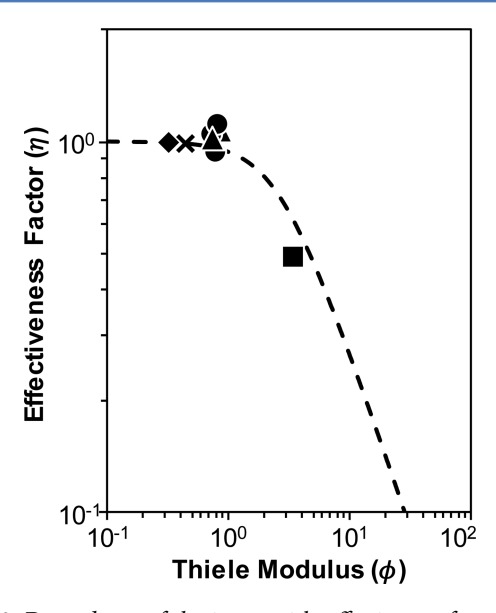
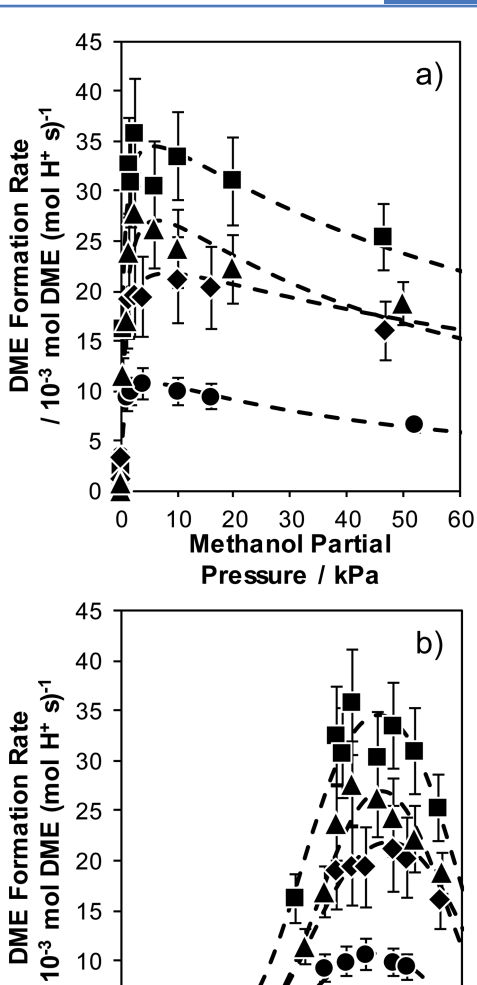


Figure 3. Dependence of the intraparticle effectiveness factor on the Thiele modulus for methanol dehydration on H-CHA zeolites with Si/ $Al_f=14-18$ with 0% (circles), 18-30% (triangles), and 44% (diamond) paired Al. Data also shown for H-CHA with Si/ $Al_f=27$ (square), and H-CHA synthesized with CTAB (cross). Dashed line is the effectiveness factor predicted for a first-order reaction in a spherical pellet (Section S.5, Supporting Information).

methoxy groups under these reaction conditions (415 K, 0.77 kPa; Figure 5) and thus catalyze methanol dehydration via the associative pathway. Competitive adsorption of product water with methanol at H+ sites is also unable to account for the apparent inhibition observed at high methanol pressures, both because measured dehydration rates were invariant with reactant space velocity, and because the rate inhibition measured from deliberate water cofeeding experiments is weaker than the observed inhibition (details in Section S.6, Supporting Information). The kinetic inhibition observed at high methanol pressures occurs with the concomitant formation of methanol clusters (~3370 cm⁻¹)³¹ detected by in situ IR (Section S.6, Supporting Information). Physisorbed methanol molecules contributing to larger clusters appear to be occluded within CHA voids, but not within MFI voids under similar reaction conditions. Analogous inhibition of dehydration rates (per H⁺, 415 K) at high methanol pressures is also observed on H-AEI zeolites (Section S.6, Supporting Information), which is an eight-membered ring, window-cage framework of similar topology to CHA, suggesting that extraneous physisorbed methanol is stabilized within such cavities at these reaction conditions (>10 kPa, 415 K) and inhibits DME formation rates. Therefore, turnover rates (r_{DME}) on H-CHA zeolites were regressed to a modified rate expression (eq 3) that includes an ad-hoc correction ($k_{inhibit}$) to account for the inhibition observed at higher methanol pressures in order to estimate first-order (k_{first}) and zero-order (k_{zero}) dehydration rate constants (derivation of rate law in Section S.3, Supporting Information).

$$r_{DME,A} = \frac{k_{first,A} P_{CH_3OH}}{1 + \frac{k_{first,A}}{k_{zero,A}} P_{CH_3OH} + \frac{k_{first,A}}{k_{inhibit,A}} P_{CH_3OH}^2}$$
(3)

Zero-order rate constants for the associative pathway reflect free energy differences between DME formation transition



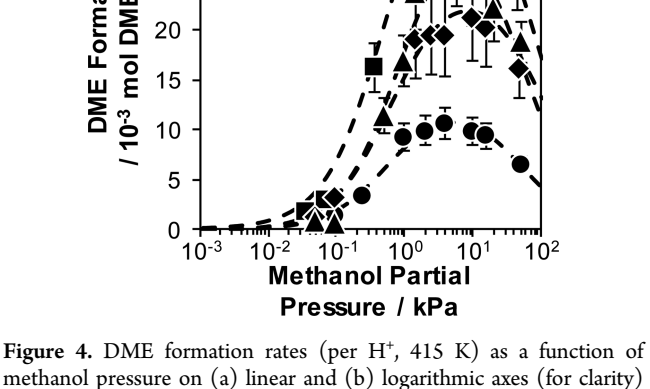


Figure 4. DME formation rates (per H⁺, 415 K) as a function of methanol pressure on (a) linear and (b) logarithmic axes (for clarity) for H-CHA with 0% (circles), 18% (diamonds), 30% (triangles), and 44% (squares) paired Al. Dashed lines represent best fits of the methanol dehydration rate expression (eq 3) regressed to the data.

states and protonated methanol dimer precursors of different cationic charge distribution but of similar size; thus, they are sensitive to differences in acid strength but are effectively insensitive to van der Waals interactions with confining environments. ^{25,32} Zero-order rate constants for the associative pathway on isolated H⁺ sites in CHA are similar (within 25%, 415 K) to those in H-MFI (Figure 2), suggesting that isolated protons in CHA are similar in acid strength to those in MFI. These findings are consistent with DFT-predicted DPE values, a probe-independent measure of Brønsted acid strength, for H⁺ sites at isolated Al atoms in zeolites that become insensitive to T-site geometry and zeolite topology (DPE: 1185-1215 kJ mol⁻¹)³ when rigorously ensemble-averaged among the different O atoms at each framework Al center. The insensitivity of acid strength to the location of Al atoms, when isolated within an insulating silica lattice, reflects the similar stabilities of conjugate anions formed upon deprotonation and their weak dependence on local geometry.

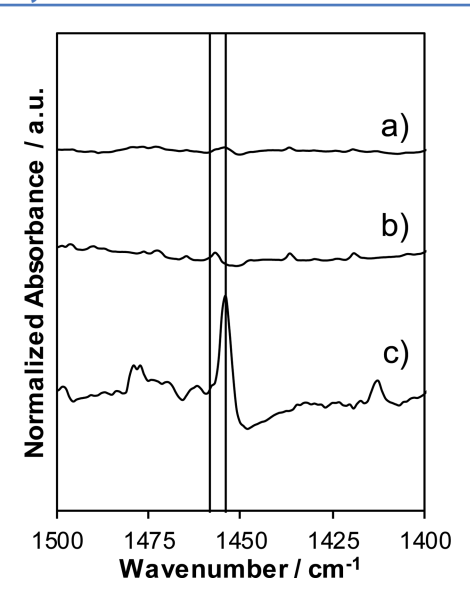


Figure 5. In situ IR spectra of (a) H-CHA ($Si/Al_f = 14$) containing only isolated protons and (b) H-MFI (Si/Al = 43, Zeolyst) under 0.77 kPa CH₃OH at 415 K. Vertical dashed lines indicate the location of surface (1457 cm^{-1}) and (c) gas-phase (1454 cm^{-1}) methoxy deformation modes.

First-order rate constants for the associative pathway reflect free energy differences between DME formation transition states and hydrogen-bonded methanol monomer precursors of different cationic charge distribution and size; thus, they are sensitive to differences in both acid strength and confinement. 25,32 First-order rate constants for the associative pathway were nearly an order of magnitude larger (415 K) on isolated H⁺ sites in H-CHA than in H-MFI (Figure 2), reflecting preferential stabilization of larger transition states over smaller methanol monomers within the more confining environments of CHA, given the similar acid strength of isolated protons in zeolitic frameworks. The dependence of methanol dehydration first-order rate constants reported for zeolites of widely varying pore size $(0.5-1.2 \text{ nm free sphere diameter})^{32}$ allows estimating the effective reaction volume in H-CHA from its first-order rate constant and suggests that methanol dehydration in CHA zeolites occurs within void sizes characteristic of 6-MR and 8-MR (Section S.3, Supporting Information). Additionally, first-order and zero-order rate constants (per H⁺, 415 K) on isolated H⁺ sites in CHA zeolites synthesized in fluoride media (Figure 2) are equivalent to those on CHA zeolites synthesized in hydroxide media, providing evidence that these samples contain only isolated framework Al atoms and protons of indistinguishable acid strength.

2.4. Methanol dehydration catalysis on H-CHA zeolites containing paired protons. Methanol dehydration rates are shown as a function of methanol pressure in Figure 4 for H-CHA zeolites of fixed composition (Si/Al_f = 14–17), but with systematically increasing percentages of paired Al (0–44%). All rates were uncorrupted by intraparticle transport artifacts ($\eta > 0.95$; Figure 3), and kinetic data for all samples can be found in Section S.3 of the Supporting Information. Methanol dehydration rates on each H-CHA zeolite containing paired protons decreased at higher methanol pressures (>10 kPa, Figure 4) concomitant with the formation of methanol clusters (\sim 3370 cm⁻¹; Section S.4, Supporting Information) at high methanol pressures, as observed for H-CHA zeolites containing only isolated protons. Methanol dehydration

turnover rates on H-CHA (415 K), normalized per total proton, increased systematically with the fraction of protons compensating paired framework Al sites, over the entire range of methanol pressures studied.

Turnover rates measured on a given H-CHA zeolite were regressed to eq 3 in order to estimate first-order and zero-order rate constants, which are plotted in Figure 6 as a function of

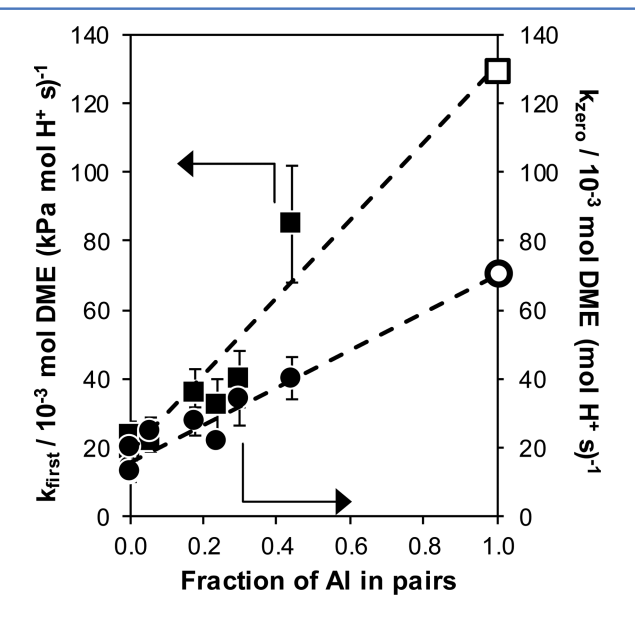


Figure 6. First-order (squares) and zero-order (circles) rate constants (415 K, per H^+) on CHA zeolites (Si/Al_f = 14–18) as a function of the fraction of Al in pairs. Dashed lines are linear regressions to the data points (solid). Extrapolated dehydration rate constants for paired protons are shown as open symbols.

paired Al content. Rate constants were described using a weighted average of contributions (via eq 3) from isolated and paired protons on each sample, which allowed estimation of their individual first-order and zero-order rate constants (discussion in Section S.3, Supporting Information); these are shown by the values extrapolated to 0% and 100% paired Al in Figure 6 and listed in Table 1. This kinetic treatment indicates that first-order and zero-order rate constants (per H⁺, 415 K) in H-CHA are nearly an order of magnitude larger on paired protons than on isolated protons (Figure 6, Table 1).

Coincidentally, the crystallite sizes of CHA zeolites generally decreased with increasing paired Al content (Table 1). Possible contributions of ameliorated intraparticle transport restrictions to the turnover rate enhancements observed with increased paired Al content were further probed by synthesizing a CHA zeolite of similar composition (Si/Al = 16; TMAda⁺ as the sole SDA), but with a smaller crystallite size using the hexadecyltrimethylammonium bromide (CTAB) surfactant to arrest crystal growth.³³ SEM micrographs of this CHA zeolite showed crystallites of ~800 nm diameter (Section S.2, Supporting Information), which contained a small fraction of paired Al sites (6% paired Al) that presumably result from the presence of an additional quaternary amine (CTAB) during crystallization. Methanol dehydration rate constants (per H⁺, 415 K) measured on this sample (Table 1, Figure 6) are equivalent to values expected from the correlation between dehydration rate constants and paired Al content measured on larger CHA crystallites (1–2 μ m; Figure 6). Intraparticle concentration gradients are also predicted to be negligible within 800 nm

diameter CHA crystallites (η > 0.95; Figure 3). These results support the conclusion that methanol dehydration turnover rates measured here on CHA zeolites of fixed composition (Si/Al = 15; <2 μ m diam) are kinetic in origin, and that turnover rate enhancements reflect contributions from larger fractions of paired proton ensembles. The order-of-magnitude larger rate constants at paired protons may reflect lower apparent Gibbs free energy differences for the associative dehydration pathway, or the stabilization of intermediates that mediate dissociative dehydration pathways.

In situ IR spectra of H-CHA zeolites containing paired protons (Section S.4, Supporting Information) showed formation of hydrogen-bonded methanol monomers at low pressures (<1 kPa) and protonated methanol dimers at higher pressures (>3 kPa), as observed for H-MFI and H-CHA zeolites containing only isolated protons. Yet, H-CHA zeolites containing paired protons also showed surface methoxy deformation modes (~1457 cm⁻¹) at low methanol pressures (<3 kPa; Figure 7), which appear as shoulders that overlap with

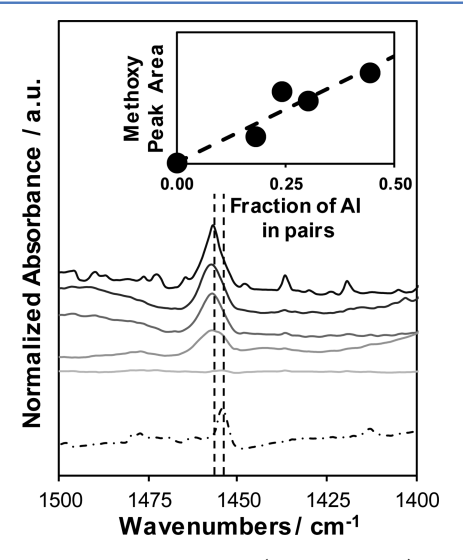


Figure 7. *In situ* IR spectra of H-CHA (Si/Al $_{\rm f}$ = 14–17) containing 0–44% paired Al (light to dark) under 0.77 kPa CH $_{\rm 3}$ OH (415 K). Dashed lines indicate the location of surface (1457 cm $^{-1}$) and gasphase (1454 cm $^{-1}$; dash-dotted spectrum) methoxy deformation modes. The inset shows the integrated area of the surface methoxy peak as a function of the fraction of Al in pairs.

deformation modes of gaseous methanol (1454 cm⁻¹) at higher pressures (>3 kPa). Integrated areas of surface methoxy deformation modes in CHA zeolites of similar total proton content, measured in the first-order kinetic regime at fixed CH₃OH pressure (0.77 kPa, 415 K), increased linearly with paired Al content (Figure 7, inset), consistent with stabilization of surface methoxy species at paired protons. These quantitative spectral data provide direct evidence that the dissociative dehydration pathway can prevail on paired protons in H-CHA, which appears to accelerate observed dehydration turnovers by an order of magnitude (415 K) relative to those mediated by the associative pathway on isolated protons (Figure 6).

3. CONCLUSIONS

These data constitute a predictive synthesis-structure—function relation for the proximity of framework aluminum atoms, and of their charge-compensating extraframework proton active sites, in single T-site CHA zeolite lattices. Synthesis and structure were connected by crystallizing CHA zeolites using low charge density organic TMAda+ cations and high charge density inorganic Na+ cations as cooperative SDAs, in which the amount of Na⁺ retained within crystallized products correlated with the number of paired Al sites formed, which were quantified using validated Co2+ titration methods. Structure and catalytic function were connected by measuring kinetic rate constants of methanol dehydration to dimethyl ether on CHA zeolites of similar composition but varying paired Al content. Paired protons accelerate dehydration turnover rates by an order of magnitude (415 K) relative to isolated protons, because paired protons appear to stabilize surface methoxy species involved in an alternate dehydration mechanism. An order-of-magnitude difference in methanol dehydration rate constants, here reflecting the distinct catalytic behavior of isolated and paired protons in CHA zeolites, is quantitatively reminiscent of the difference in first-order dehydration rate constants conferred by the diverse confining voids of MFI intersections (~0.7 nm diam.) and FAU supercages (~1.3 nm diam.).³²

Predictive synthetic control of the arrangement of framework Al atoms in zeolites of fixed composition, especially for those containing a single crystallographically unique T-site, provides opportunities to synthesize materials with tunable catalytic and structural properties, while maintaining a constant bulk density of active sites, if so desired. These synthetic protocols can be used to influence the speciation of extraframework Cu ions, which behave as active sites for the selective catalytic reduction (SCR) of nitrogen oxides with ammonia, because Cu²⁺ cations exchange preferentially at paired Al sites while [CuOH]⁺ species exchange at isolated Al sites in CHA zeolites.¹⁷ Isolated framework Al atoms appear less susceptible to hydrothermal dealumination, according to ²⁹Si NMR studies of steam-treated FAU zeolites that show preferential removal of Al atoms in next-nearest neighbor configurations ((Si-O)₂-Si-(O-Al)₂: δ = -95 ppm).³⁴ Moreover, the different C₁ intermediates prevalent at distinct proton active site ensembles in CHA zeolites of similar composition, under identical operating conditions, may have implications for methanol conversion routes in small-pore zeolites, such as methanol-to-olefins (MTO) and methanol-to-hydrocarbons (MTH) catalysis. CHA molecular sieves (e.g., SAPO-34, SSZ-13) convert methanol selectively to ethene and propene, 35,36 but deactivate upon formation of polycyclic aromatic species within CHA cages that hinder product diffusion; 36,37 the proximity of H+ sites within CHA zeolites, varied by changing bulk composition, has been proposed to influence the time-on-stream stability during MTO catalysis.³⁸ Surface methoxy groups have also been implicated as intermediates in hydride transfer reactions with adsorbed olefins, 39,40 and in the initiation of C-C bond formation via carbonylation with carbon monoxide or formaldehyde present either as impurities in reactant feeds or formed in situ.41,42

Within the context of aluminosilicate zeolites, these findings represent progress toward developing methods that may enable systematic and predictable control of the arrangement of matter at the atomic scale. The consequent and marked effects of active site proximity on methanol dehydration rate constants among high-symmetry (1 T-site) CHA zeolites of effectively fixed composition, at first glance, contrast the alpha test results of Haag and co-workers, in which hexane cracking rates appeared insensitive to the diverse active site ensembles likely

present among low-symmetry (12 T-site) MFI zeolites of widely varying composition. This apparent discord can be reconciled by many possibilities, such as if the crystallization procedures of MFI samples studied led to similar Al arrangements, if the alpha test is insensitive to acid site proximity, or if acid site ensembles differ in catalytic function among different zeolite topologies. Nevertheless, the data reported here provide a provocative contrast to the landmark demonstration of Haag and co-workers. They demonstrate that catalytic diversity for the same reaction can be introduced into zeolites of fixed structure and composition, even for frameworks containing a single lattice T-site, through synthetic control of the atomic arrangement of matter.

4. EXPERIMENTAL METHODS

4.1. Synthesis and preparation of MFI and CHA zeolites. MFI zeolites (CBV8014, Si/Al = 43; CBV5524G, Si/Al = 30) were obtained from Zeolyst International in their NH₄-form and converted to their H-form according to the procedures described below. CHA zeolites synthesized without Na $^+$ in hydroxide media and Si-CHA were prepared by following previously reported procedures. Full details of synthetic procedures can be found in Section S.1 of the Supporting Information.

CHA zeolites were prepared using different Al precursors by adapting procedures described by Deka et al.,44 which is a modified version of the original synthesis reported by Zones.⁴⁵ A synthesis molar ratio of 1 SiO₂/ 0.033 Al₂O₃/ 0.25 TMAdaOH/0.125 Na₂O/44 H₂O was used to obtain a Si/Al = 15 and Na⁺/TMAda⁺ = 1 in the synthesis solution. A typical synthesis involved adding an aqueous TMAdaOH solution (25 wt %, Sachem) to deionized H_2O (18.2 $M\Omega$) in a perfluoroalkoxy alkane jar (PFA, Savillex Corp.) and stirring the solution under ambient conditions for 15 min. Next, either aluminum hydroxide (Al(OH)₃, grade 0325, SPI Pharma), aluminum nitrate nonahydrate (Al(NO₃)₃, 98 wt %, Sigma-Aldrich), aluminum chloride (AlCl₃, 99 wt %, Sigma-Aldrich), alumina (Al₂O₃, 99.5 wt %, Alfa Aesar), sodium aluminate (NaAlO₂, technical grade, Alfa Aesar), or aluminum isopropoxide (Al(O-i-Pr)₃, 98 wt %, Sigma-Aldrich) was added to the aqueous TMAdaOH solution. Then, a 5 M sodium hydroxide solution (NaOH: 16.7 wt % NaOH in deionized water; NaOH pellets 98 wt %, Alfa Aesar) was added dropwise to the synthesis mixture and stirred under ambient conditions for 15 min. Finally, colloidal silica (Ludox HS40, 40 wt %, Sigma-Aldrich) was added and the mixture was covered and stirred for 2 h under ambient conditions. All synthesis reagents were used without further purification. The synthesis solution was then transferred to a 45 mL Teflon-lined stainless steel autoclave (Parr Instruments) and placed in a forced convection oven (Yamato DKN-402C) at 433 K and rotated at 40 rpm for 6 days.

CHA zeolites were also synthesized in fluoride media using only TMAda $^+$ as the SDA and without Na $^+$ present following the procedure reported by Eilertsen et al., 30 using a molar ratio of 1 SiO $_2$ / 0.0167 Al $_2$ O $_3$ / 0.5 TMAdaOH/0.5 HF/3 H $_2$ O. In a typical synthesis, Al $_2$ O $_3$ was added to an aqueous TMAdaOH solution in a PFA jar and the mixture was stirred for 15 min under ambient conditions. Then, tetraethylorthosilicate (TEOS, 98 wt %, Sigma-Aldrich) was added to the mixture, and the contents were covered and stirred for 2 h at ambient conditions until a homogeneous solution was obtained. Next, ethanol (200 proof, Koptec) was added to the synthesis

solution and left uncovered to allow ethanol and excess water to evaporate in order to reach the target molar ratios. Once the synthesis solution had reached the desired H₂O/SiO₂ ratio, concentrated hydrofluoric acid (HF; 48 wt %, Sigma-Aldrich) was added dropwise to the synthesis and homogenized for 15 min by hand. Caution: when working with hydrofluoric acid use appropriate personal protective equipment, ventilation, and other safety measures. Upon addition of HF, the solution immediately became a thick paste. The mixture was then left to sit uncovered under ambient conditions for 30 min to allow any residual HF to evaporate before transferring the solution to a 45 mL Teflon-lined stainless steel autoclave and heated in a forced convection at 423 K under rotation at 40 rpm for 6 days.

CHA zeolites were synthesized with 800 nm crystallite diameters following the procedure reported by Li et al.,³³ but omitting the NaOH addition. First, a Na⁺-free CHA synthesis solution was prepared (Section S.1, Supporting Information), placed in a 45 mL Teflon-lined stainless steel autoclave and heated in a forced convection oven at 433 K while rotating at 40 rpm for 1 day. The autoclave was removed from the oven and quenched in a room temperature water bath for 4 h. After cooling to ambient conditions, hexadecyltrimethylammonium bromide (CTAB, 99 wt %, Sigma-Aldrich) was added to the synthesis mixture to act as a crystal growth inhibitor.^{33,46} The CTAB containing synthesis mixture was then returned to the autoclave and heated at 433 K and rotated at 40 rpm for 9 additional days.

Zeolite crystallization products were isolated via centrifugation and washed thoroughly with deionized water (18.2 M Ω) and acetone (99.9 wt %, Sigma-Aldrich) in alternating steps (70 cm³ solvent g⁻¹ per wash) until the pH of the supernatant remained constant between washes, followed by a final water wash to remove residual acetone. Solids were recovered via centrifugation, dried at 373 K under stagnant air for 24 h, and then treated in flowing dry air $(1.67 \text{ cm}^3 \text{ s}^{-1} \text{ g}^{-1}, 99.999\% \text{ UHP},$ Indiana Oxygen) at 853 K (0.0167 K s⁻¹) for 10 h. Residual Na+ was removed by converting to the NH₄-form via ionexchange using 150 cm³ of an aqueous 1 M NH₄NO₃ solution (8.0 wt % in H₂O; 99.9 wt %, Sigma-Aldrich) per gram zeolite, and stirring for 24 h under ambient conditions. Solids were recovered via centrifugation and washed four times with deionized water (70 cm³ g⁻¹ per wash). Recovered NH₄-form zeolites were then dried at 373 K under stagnant air for 24 h, and converted to their H-form by treatment in flowing dry air (1.67 cm³ s⁻¹ g⁻¹, 99.999% UHP, Indiana Oxygen) at 773 K (0.0167 K s⁻¹) for 4 h.

4.2. Characterization of CHA and MFI zeolites. Detailed experimental procedures and characterization data for all samples can be found in Section S.2 of the Supporting Information. Error reported for elemental analysis of Al, Na, and Co, and NH₃ TPD was determined for each data point by error propagation of experimentally measured variables to the calculated value.

CHA and MFI crystal topologies were measured using powder X-ray diffraction (XRD) and confirmed by comparison with an experimental reference and the CHA and MFI diffraction patterns reported in the International Zeolite Association (IZA) structure database. Argon (87 K) and nitrogen (77 K) adsorption isotherms were used to estimate micropore volumes of CHA and MFI zeolites, respectively. Elemental composition (Al, Na, Co) of each zeolite was measured using atomic absorption spectroscopy (AAS). Thermogravimetric analysis (TGA) was used to measure the

organic content of synthesized CHA zeolite products. The crystal sizes of all CHA zeolites were estimated from scanning electron microscopy (SEM) micrographs and averaged over a distribution of individual crystal sizes taken from different regions of the SEM sample stage. The number of H⁺ sites on CHA and MFI zeolites was quantified by temperatureprogrammed desorption (TPD) of samples after aqueous ionexchange with NH₄⁺ cations, while the number of H⁺ sites remaining after Cu or Co-exchange of CHA zeolites was quantified from TPD of samples using gas-phase NH3 titrations with purging treatments to remove all non-Brønsted bound NH₃ from samples, as reported elsewhere. 48,49 27 Al magic angle spinning nuclear magnetic resonance (MAS NMR) spectra were recorded under ambient conditions on H-CHA zeolite samples to quantify their fraction of framework and extraframework Al.

 ${\rm Co}^{2+}$ titrations were performed on H-CHA zeolites via ion-exchange with 150 cm³ of an aqueous 0.25 M Co(NO₃)₂ (4.6 wt % Co(NO₃)₂; 99 wt %, Sigma-Aldrich) solution per gram of zeolite for 4 h at ambient conditions under stirring. The pH of the solution was not controlled and reached a stable value of ~3.3 after 4 h. After ion-exchange, the samples were recovered using centrifugation, washed four times with deionized water (70 cm³ per g solids per wash), and dried at 373 K under stagnant air for 24 h. Co-exchanged CHA zeolites were then treated in flowing dry air (1.67 cm³ s⁻¹ ${\rm g}_{\rm cat}^{-1}$, 99.999% UHP, Indiana Oxygen) at 773 K (0.0167 K s⁻¹) for 4 h.

Samples in Table 1 are referred to according to the formula: [countercation]-[zeolite framework]-[mineralizing agent] (Si/Al_f, % paired Al). In this nomenclature, the countercation is the extraframework titrant introduced by the ion-exchange step immediately preceding analysis (e.g., NH_4^+ or Co^{2+}) or after conversion to the H-form (e.g., H^+), while no countercation is used to describe zeolites in their directly synthesized form. The zeolite framework is either CHA or MFI, the mineralizing agent is either OH $^-$ or F $^-$, the Si/Al_f ratio is determined from elemental analysis (AAS) and 27 Al NMR, and the % paired Al is determined from Co $^{2+}$ titration (100*2*Co/Al). For example, an H-form CHA zeolite synthesized in hydroxide media with a bulk composition of Si/Al_f = 15 and 20% paired Al would have the sample name: H-CHA-OH(15,20%).

4.3. Measurement of methanol dehydration rates and titration of Brønsted acid sites during catalysis. Rates of methanol dehydration were measured at differential conversion (<10%) in a tubular packed-bed quartz reactor (7 mm inner diameter) with plug-flow hydrodynamics at 415 K. Catalyst samples were pelleted and sieved to retain particles between 180 and 250 μ m. The catalyst charged to the reactor was varied between 0.005 and 0.030 g to maintain differential conversions, and were diluted with Si-CHA (180-250 μ m) to ensure a minimum of 0.025 g of total solids were charged to the reactor. The catalyst bed was supported in the reactor between two quartz wool plugs. Reactor temperatures were controlled using a resistively heated three-zone furnace (Series 3210, Applied Test Systems) and Watlow controllers (EZ-Zone Series). The temperature of the catalyst bed was measured with a K-type thermocouple in direct contact with the external surface of the quartz tube and positioned at the center of the catalyst bed. Methanol (99.9 wt %, Sigma-Aldrich) partial pressures were controlled using a syringe pump (Legato 100, KD Scientific) and injected into flowing He (UHP, Indiana Oxygen) and sent to the reactor through heated transfer lines maintained at >373 K using resistive heating tape (BriskHeat Co.) and insulating

wrap. Prior to contact with methanol, samples were treated in a 5% $\rm O_2/He$ flow (50 cm³ g $^{-1}$ s $^{-1}$, 99.999%, Indiana Oxygen) by heating to 773 K (0.033 K s $^{-1}$) and holding for 4 h. After cooling to reaction temperature (415 K), the gas stream was switched to He flow (150 cm³ g $^{-1}$ s $^{-1}$) while methanol, at a fixed partial pressure, was sent to a gas chromatograph (Agilent 6890GC) via heated transfer lines (>373 K) for bypass calibration. Concentrations of reactants and products were measured using a gas chromatograph equipped with a flame ionization detector (HP Plot-Q KCl column, 0.53 mm ID \times 30 m \times 40 μ m film, Agilent). Only dimethyl ether and water were observed as products at all reaction conditions on all catalysts. Methane (25% CH₄/Ar, 99.999%, Indiana Oxygen) was introduced into the reactor effluent stream at a constant flow rate (0.083 cm³ s $^{-1}$) and used as an internal standard.

The total number of Brønsted acid sites in H-MFI zeolites was measured during steady state methanol dehydration catalysis using *in situ* titration with pyridine on the same reactor unit described above. Steady-state dehydration rates (3.5 kPa CH₃OH, 415 K) were achieved prior to the introduction of pyridine titrants. Pyridine (99.8 wt %, Sigma-Aldrich) was dissolved in methanol and evaporated into a flowing He stream (100 cm³ g⁻¹ s⁻¹) using a syringe pump to attain the desired concentration of reactant and titrant (3.5 kPa methanol, 0.5 Pa pyridine). The total number of protons titrated was calculated by extrapolation of dehydration rates, measured as a function of the cumulative pyridine dosed to the bed, to values of zero and assuming a 1:1 pyridine:H⁺ stoichiometry (Section S.3, Supporting Information).

The internal reproducibility error on methanol dehydration rates for each sample and set of conditions was less than 10%. The uncertainties reported here for methanol dehydration rates on CHA and MFI zeolites were determined for each data point by propagation of error in each experimentally measured variable (e.g., temperature, methanol partial pressure, catalyst mass, proton site content) to calculated rates, in order to provide representative uncertainties for values that may be reproduced by an independent researcher. The uncertainties in first-order and zero-order rate constants were determined from error analysis of a least-squares regression to the measured rate data, accounting for uncertainties in rate measurements.

4.4. Measurement of in situ IR spectra on CHA and MFI zeolites. In situ IR spectra were collected on a Nicolet 4700 spectrometer with a HgCdTe detector (MCT, cooled to 77 K by liquid N_2) by averaging 64 scans at a 2 cm⁻¹ resolution collected between 4000 and 400 cm⁻¹ range, taken relative to an empty cell background reference collected under dry He flow (0.33 cm³ s⁻¹, UHP, Indiana Oxygen) at 415 K. CHA catalysts were pressed into self-supporting wafers (0.01-0.02 g cm⁻²) and sealed within a custom-built quartz IR cell with CaF₂ windows; a detailed description of the IR cell design can be found elsewhere. 50,51 Wafer temperatures were measured within 2 mm of each side of the wafer by K-type thermocouples (Omega). The quartz IR cell was interfaced to a syringe pump (Legato 100, KD Scientific) via a stainless-steel transfer line (0.25 in. diameter) that was maintained >353 K using resistive heating tape (BriskHeat Co.) and insulating wrap, in order to deliver liquid reactants to the IR cell. Prior to each IR experiment, the catalyst wafer was treated in flowing dry air (13.3 cm³ s⁻¹ g⁻¹) purified by an FTIR purge gas generator (Parker Balston, < 1 ppm of CO₂, 200 K H₂O dew point) to 773 K (0.083 K s⁻¹) for 4 h, and then cooled under flowing He $(13.3 \text{ cm}^3 \text{ s}^{-1} \text{ g}^{-1})$ to 415 K. Methanol was introduced into the

heated gas stream under steady-state flow, and methanol partial pressures were varied nonsystematically between 0.1 and 22 kPa. IR spectra were recorded after equilibration of the surface was achieved (~30 min) and peak intensities remained constant for 15 min. All IR spectra were baseline-corrected and normalized to combination and overtone zeolite T-O-T vibrational modes (1750–2100 cm $^{-1}$) only when comparing between different parent CHA samples, because adsorption of methanol on the zeolite surface caused a systematic change to the T-O-T band area with changing methanol pressure. An IR spectrum of an empty IR cell under 2 kPa steady-state methanol pressure (13.3 cm 3 s $^{-1}$ g $^{-1}$ He) was used as a reference for gas-phase methanol vibrational modes observed in spectra of catalyst wafers recorded under steady-state methanol pressure.

ASSOCIATED CONTENT

Supporting Information

The Supporting Information is available free of charge on the ACS Publications website at DOI: 10.1021/acscatal.7b01273.

Synthesis of CHA zeolites (Section S.1), Characterization of CHA and MFI zeolites (Section S.2), Methanol dehydration catalysis and kinetic treatments (Section S.3), Measurement of *in situ* IR spectra on CHA and MFI zeolites (Section S.4), Evaluation of mass transfer in CHA zeolites (Section S.5), Origin of kinetic inhibition in CHA zeolites (Section S.6) (PDF)

AUTHOR INFORMATION

Corresponding Author

*E-mail: rgounder@purdue.edu.

ORCID

John R. Di Iorio: 0000-0002-7519-5100 Rajamani Gounder: 0000-0003-1347-534X

Notes

The authors declare no competing financial interest.

■ ACKNOWLEDGMENTS

We acknowledge the financial support from the National Science Foundation under award number 1552517-CBET. We thank Sachem, Inc., for providing the organic structure-directing agent used to synthesize CHA zeolites, and Mark Davis (Caltech) and Michiel Dusselier (KU Leuven) for providing the AEI zeolite sample. We also thank John Harwood (Purdue Interdepartmental NMR Facility) for assistance collecting NMR spectra, Michael Cordon for assistance collecting SEM micrographs, and Hyun Chang Kim and You-Yeon Won (Purdue) for DLS measurements. Finally, we thank David Hibbitts (Florida), Juan Carlos Vega-Vila, and Jason Bates for technical discussions and feedback on this manuscript.

REFERENCES

- (1) Haag, W.; Lago, R.; Weisz, P. Nature 1984, 309, 589-591.
- (2) Boudart, M. Chem. Rev. 1995, 95, 661-666.
- (3) Jones, A. J.; Iglesia, E. ACS Catal. 2015, 5, 5741-5755.
- (4) Gounder, R.; Iglesia, E. Chem. Commun. 2013, 49, 3491-3509.
- (5) Pinar, A. B.; Gomez-Hortiguela, L.; Perez-Pariente, J. Chem. Mater. 2007, 19, 5617–5626.
- (6) Yokoi, T.; Mochizuki, H.; Namba, S.; Kondo, J. N.; Tatsumi, T. *J. Phys. Chem. C* **2015**, *119*, 15303–15315.
- (7) Dědeček, J.; Sobalík, Z.; Wichterlová, B. Catal. Rev.: Sci. Eng. 2012, 54, 135–223.

- (8) Janda, A.; Bell, A. T. J. Am. Chem. Soc. 2013, 135, 19193-19207.
- (9) Mlinar, A. N.; Zimmerman, P. M.; Celik, F. E.; Head-Gordon, M.; Bell, A. T. *J. Catal.* **2012**, 288, 65–73.
- (10) Song, C.; Chu, Y.; Wang, M.; Shi, H.; Zhao, L.; Guo, X.; Yang, W.; Shen, J.; Xue, N.; Peng, L.; Ding, W. *J. Catal.* **2017**, 349, 163–174.
- (11) Dedecek, J.; Balgová, V.; Pashkova, V.; Klein, P.; Wichterlová, B. Chem. Mater. **2012**, 24, 3231–3239.
- (12) Gábová, V.; Dědeček, J.; Čejka, J. Chem. Commun. **2003**, 1196–
- (13) Pashkova, V.; Klein, P.; Dedecek, J.; Tokarová, V.; Wichterlová, B. *Microporous Mesoporous Mater.* **2015**, 202, 138–146.
- (14) Bernauer, M.; Tabor, E.; Pashkova, V.; Kaucký, D.; Sobalík, Z.; Wichterlová, B.; Dedecek, J. *J. Catal.* **2016**, 344, 157–172.
- (15) Jones, A. J.; Iglesia, E. Angew. Chem., Int. Ed. 2014, 53, 12177–12181
- (16) Di Iorio, J. R.; Gounder, R. Chem. Mater. 2016, 28, 2236-2247.
- (17) Paolucci, C.; Parekh, A. A.; Khurana, I.; Di Iorio, J. R.; Li, H.; Albarracin Caballero, J. D.; Shih, A. J.; Anggara, T.; Delgass, W. N.; Miller, J. T.; Ribeiro, F. H.; Gounder, R.; Schneider, W. F. *J. Am. Chem. Soc.* **2016**, *138*, 6028–6048.
- (18) Zones, S. I. *J. Chem. Soc., Faraday Trans.* **1991**, 87, 3709–3716. (19) Burton, A. W.; Zones, S. I. *Stud. Surf. Sci. Catal.* **2007**, 168, 137–179.
- (20) Park, M. B.; Ahn, S. H.; Nicholas, C. P.; Lewis, G. J.; Hong, S. B. *Microporous Mesoporous Mater.* **2017**, 240, 159–168.
- (21) Shantz, D. F.; Schmedt auf der Günne, J.; Koller, H.; Lobo, R. F. J. Am. Chem. Soc. **2000**, 122, 6659–6663.
- (22) Cundy, C. S.; Cox, P. A. Microporous Mesoporous Mater. **2005**, 82, 1–78.
- (23) Lewis, G. J.; Miller, M. A.; Moscoso, J. G.; Wilson, B. A.; Knight, L. M.; Wilson, S. T. *Stud. Surf. Sci. Catal.* **2004**, *154*, 364–372.
- (24) Park, M. B.; Lee, Y.; Zheng, A.; Xiao, F.-S.; Nicholas, C. P.; Lewis, G. J.; Hong, S. B. *J. Am. Chem. Soc.* **2013**, *135*, 2248–2255.
- (25) Carr, R. T.; Neurock, M.; Iglesia, E. J. Catal. 2011, 278, 78-93.
- (26) Jones, A. J.; Carr, R. T.; Zones, S. I.; Iglesia, E. J. Catal. 2014, 312, 58-68.
- (27) Ghorbanpour, A.; Rimer, J. D.; Grabow, L. C. ACS Catal. 2016, 6, 2287–2298.
- (28) Bligaard, T.; Bullock, R. M.; Campbell, C. T.; Chen, J. G.; Gates, B. C.; Gorte, R. J.; Jones, C. W.; Jones, W. D.; Kitchin, J. R.; Scott, S. L. ACS Catal. **2016**, *6*, 2590–2602.
- (29) Koros, R.; Nowak, E. Chem. Eng. Sci. 1967, 22, 470.
- (30) Eilertsen, E. A.; Arstad, B.; Svelle, S.; Lillerud, K. P. *Microporous Mesoporous Mater.* **2012**, *153*, 94–99.
- (31) Mirth, G.; Lercher, J. A.; Anderson, M. W.; Klinowski, J. J. Chem. Soc., Faraday Trans. 1990, 86, 3039–3044.
- (32) Jones, A. J.; Zones, S. I.; Iglesia, E. J. Phys. Chem. C 2014, 118, 17787–17800.
- (33) Li, Z.; Navarro, M. T.; Martinez-Triguero, J.; Yu, J.; Corma, A. Catal. Sci. Technol. **2016**, *6*, 5856–5863.
- (34) Klinowski, J.; Thomas, J.; Fyfe, C.; Gobbi, G. *Nature* **1982**, 296, 533–536.
- (35) Chang, C. D. Catal. Rev.: Sci. Eng. 1983, 25, 1-118.
- (36) Haw, J. F.; Song, W.; Marcus, D. M.; Nicholas, J. B. Acc. Chem. Res. 2003, 36, 317–326.
- (37) Zhu, X.; Hofmann, J. P.; Mezari, B.; Kosinov, N.; Wu, L.; Qian, Q.; Weckhuysen, B. M.; Asahina, S.; Ruiz-Martínez, J.; Hensen, E. J. ACS Catal. 2016, 6, 2163–2177.
- (38) Deimund, M. A.; Harrison, L.; Lunn, J. D.; Liu, Y.; Malek, A.; Shayib, R.; Davis, M. E. ACS Catal. **2016**, *6*, 542–550.
- (39) Hwang, A.; Kumar, M.; Rimer, J. D.; Bhan, A. J. Catal. 2017, 346, 154–160.
- (40) Müller, S.; Liu, Y.; Kirchberger, F. M.; Tonigold, M.; Sanchez-Sanchez, M.; Lercher, J. A. J. Am. Chem. Soc. **2016**, 138, 15994–16003.
- (41) Liu, Y.; Müller, S.; Berger, D.; Jelic, J.; Reuter, K.; Tonigold, M.; Sanchez-Sanchez, M.; Lercher, J. A. Angew. Chem. 2016, 128, 5817–5820
- (42) Song, W.; Marcus, D. M.; Fu, H.; Ehresmann, J. O.; Haw, J. F. J. Am. Chem. Soc. **2002**, 124, 3844–3845.

(43) Camblor, M. A.; Villaescusa, L. A.; Díaz-Cabañas, M. J. *Top. Catal.* **1999**, *9*, 59–76.

- (44) Deka, U.; Juhin, A.; Eilertsen, E. A.; Emerich, H.; Green, M. A.; Korhonen, S. T.; Weckhuysen, B. M.; Beale, A. M. *J. Phys. Chem. C* **2012**, *116*, 4809–4818.
- (45) Zones, S. I. Zeolite SSZ-13 and Its Method of Preparation. US4544538 A, 1985.
- (46) Zhu, Y.; Hua, Z.; Zhou, J.; Wang, L.; Zhao, J.; Gong, Y.; Wu, W.; Ruan, M.; Shi, J. Chem. Eur. J. 2011, 17, 14618–14627.
- (47) Baerlocher, C.; McCusker, L. B. Database of Zeolite Structures. http://www.iza-structure.org/databases/ (2017).
- (48) Bates, S. A.; Delgass, W. N.; Ribeiro, F. H.; Miller, J. T.; Gounder, R. J. Catal. 2014, 312, 26–36.
- (49) Di Iorio, J. R.; Bates, S. A.; Verma, A. A.; Delgass, W. N.; Ribeiro, F. H.; Miller, J. T.; Gounder, R. *Top. Catal.* **2015**, *58*, 424–424
- (50) Cybulskis, V. J.; Harris, J. W.; Zvinevich, Y.; Ribeiro, F. H.; Gounder, R. Rev. Sci. Instrum. 2016, 87, 103101.
- (51) Harris, J. W.; Cordon, M. J.; Di Iorio, J. R.; Vega-Vila, J. C.; Ribeiro, F. H.; Gounder, R. *J. Catal.* **2016**, 335, 141–154.

SUPPORTING INFORMATION

Introducing Catalytic Diversity into Single-Site Chabazite Zeolites of Fixed Composition via Synthetic Control of Active Site Proximity

John R. Di Iorio, Claire T. Nimlos, Rajamani Gounder*

Charles D. Davidson School of Chemical Engineering, Purdue University, 480 Stadium Mall

Drive, West Lafayette, IN 47907, USA

^{*}Corresponding author: rgounder@purdue.edu

Table of Contents

Section S.1. Synthesis of CHA zeolites	Pages 1-2
S.1.1. Synthesis of CHA zeolites with different Al precursors	Page 1
S.1.2. Synthesis of Na ⁺ -free CHA zeolites in OH ⁻ media	Pages 1-2
S.1.3. Synthesis of Si-CHA zeolites in F ⁻ media	Page 2
Section S.2. Characterization of CHA and MFI zeolites	Pages 3-29
S.2.1. Characterization data of all zeolites	Pages 3-4
S.2.2. X-Ray diffraction of MFI and CHA zeolites	Pages 5-8
S.2.3. Adsorption isotherms for CHA and MFI zeolites	Pages 9-14
S.2.4. Elemental analysis of CHA and MFI zeolites	Page 15
S.2.5. Quantification of organic content in as-synthesized CHA zeolites	Page 15
S.2.6. Estimation of CHA crystal diameter from SEM and DLS	Pages 16-22
S.2.7. Quantification of H ⁺ sites by NH ₃ TPD	Page 22
S.2.8. ²⁷ Al MAS NMR to characterization Al coordination environment	Pages 23-26
S.2.9. Validation of Co ²⁺ titration procedures on H-CHA-F zeolites	Pages 27-29
Section S.3. Methanol dehydration catalysis and kinetic treatments	Pages 30-50
S.3.1. Derivation of the associative dehydration rate expression	Pages 30-32
S.3.2. Derivation of the associative dehydration rate expression with inhibition	Pages 32-33
S.3.3. Derivation of the dissociative methanol dehydration rate expression	Pages 34-36
S.3.4. Estimation of associative and dissociative first and zero-order rate	Page 37
constants using a generalized rate equation	
S.3.5. Elimination of background reaction artifacts	Pages 37-38
S.3.6. Catalyst stability and time-on-stream deactivation	Pages 38-39
S.3.7. Elimination of approach to equilibrium artifacts	Pages 39-40
S.3.8. Benchmarking of measured reaction kinetics on H-MFI	Pages 40-44
S.3.9. DME formation rates (415 K) as a function of CH ₃ OH pressure	Pages 45-49
S.3.10. Estimation of associative and dissociative rate constants in CHA zeolites	Pages 50
Section S.4. Measurement of in situ IR spectra on CHA and MFI zeolites	Pages 51-52
Section S.5. Evaluation of mass transfer in CHA zeolites	Pages 53-64
S.5.1. Space velocity tests to assess external diffusion limitations	Page 53
S.5.2. Derivation of concentration gradients in spherical catalyst	Pages 54-60
particles to assess coupled reaction and internal diffusion	
S.5.3. Derivation of first and zero order effectiveness factors	Pages 61-63
Section S.6. Origin of kinetic inhibition in CHA zeolites	Pages 64-68
Section S.7. References	Page 69

Section S.1. Synthesis and ion-exchange of CHA and MFI zeolites

S.1.1. Synthesis of CHA zeolites with different Al precursors

The procedure for preparing CHA zeolites using various Al precursors is described in the main text. Table S1 shows the weights of various reagents used during crystallization.

Table S1. Weights (in grams) of synthesis reagents used in the crystallization of CHA zeolites with different Al precursors and equimolar amounts of Na⁺ and TMAda⁺ in OH⁻ media.

Al precursor used	Al source	Colloidal SiO2	5M NaOH	TMAdaOH	H ₂ O
Al(OH) ₃	0.109 g	3.150 g	1.284 g	4.432 g	10.34 g
$Al(NO_3)_3$	0.530 g	3.150 g	1.284 g	4.432 g	10.34 g
AlCl ₃	0.188 g	3.150 g	1.284 g	4.432 g	10.34 g
Al_2O_3	0.114 g	3.150 g	1.284 g	4.432 g	10.34 g
$NaAlO_2$	0.184 g	3.150 g	1.154 g	4.432 g	9.623 g
Al(O-i-Pr) ₃	0.288 g	3.150 g	1.284 g	4.432 g	10.34 g

S.1.2. Synthesis of Na⁺-free CHA zeolites in OH⁻ media

Na⁺-free CHA zeolites were synthesized in hydroxide media at different compositions (Si/Al = 15-30) following previously reported procedures.¹ Briefly, a molar ratio of 1 SiO₂/ X Al₂O₃/ 0.5 TMAdaOH/ 44 H₂O was used, where X is the desired Al content to reach a Si/Al molar ratio of 15 or 30. In a typical synthesis, an aqueous TMAdaOH solution was added to deionized water in a perfluoroalkoxy alkane (PFA) jar and stirred for 15 minutes under ambient conditions. Next, Al(OH)₃ was added to the TMAdaOH solution and the mixture was stirred for 15 minutes under ambient conditions. Then, colloidal silica was added to the mixture and the contents were stirred for 2 h at ambient conditions until a homogeneous solution was obtained. All synthesis

reagents were used without further purification. The synthesis solution was then transferred to a 45 ml Teflon-lined stainless steel autoclave and heated in a forced convection oven at 433 K and rotated at 40 RPM for 6 days.

S.1.3. Synthesis of Si-CHA zeolites in F⁻ media

Pure SiO₂ chabazite was synthesized following a previously reported procedures^{1,2} using a synthesis solution molar ratio of 1 SiO₂/ 0.5 TMAdaOH/ 0.5 HF/ 3 H₂O. In a typical synthesis, TEOS was added to a PFA jar containing an aqueous TMAdaOH solution and stirred under ambient conditions. Ethanol, formed from the hydrolysis of TEOS, and excess water were then evaporated under ambient conditions to reach target molar ratios. Once the synthesis solution had reached the desired H₂O/SiO₂ ratio, hydrofluoric acid (HF) was added dropwise to the synthesis and homogenized for 15 minutes. *Caution: when working with HF acid, use appropriate personal protective equipment, ventilation, and other safety measures.* The mixture was then left to sit uncovered under ambient conditions for 30 minutes to allow for any residual HF to evaporate before transferring the solution to a 45 ml Teflon-lined stainless steel autoclave and heated in a forced convection oven at 423 K under rotation at 40 RPM for 40 h.

Section S.2. Characterization of CHA and MFI zeolites

S.2.1. Characterization data of all zeolites

Samples are labeled using the formula prescribed in the main text: [counter-cation]-[zeolite framework]-[mineralizing agent](Si/Al_f, % paired Al). Tables S2-S5 contain characterization and kinetic data for CHA zeolites synthesized without Na⁺ in OH⁻ and F⁻ media (Table S2), with various Al precursors using equimolar amounts of Na⁺ and TMAda⁺ (Table S3), with Al(OH)₃ and equimolar amounts of Na⁺ and TMAda⁺ and inclusion of hexadecyltrimethylammonium bromide (CTAB; Table S4), and for MFI zeolites (Table S5). Each table includes micropore volumes determined from adsorption isotherms (Section S.2.3), bulk Si/Al ratio from atomic absorption spectroscopy (Section S.2.4), organic content measured by thermogravimetric analysis (Section S.2.5), H⁺/Al values measured from NH₃ temperature programmed desorption (Section S.2.6), and the fraction of isolated (Al_{iso}/Al_{tot}) and paired (Al_{pair}/Al_{tot}) Al measured from Co²⁺ titration (procedure in main text). Also presented are first and zero-order rate constants (per H⁺) for the dehydration of methanol to dimethyl ether measured at 415 K (procedure in main text; Section S.3).

Table S2. Characterization data of CHA zeolites synthesized using Al(OH)₃ as the aluminum source, without Na⁺ in OH⁻ and F⁻ media.

	Characterization and Site Distribution						Kin	etics
Sample	Si/Al _f	H ⁺ /Al _f	Micropore Volume / cm³ g-1	Organic Content / wt%	A_{iso}/Al_f	A _{pair} /Al _f	$\mathbf{k_{first}}^a$	k _{zero} b
CHA-OH(14,0%)	14	0.95	0.18	18.4	1	0	21.9	13.9
CHA-OH(17,0%)	17	1.00	0.21	22.5	1	0	22.6	12.3
CHA-OH(27,0%)	27	1.00	0.17	21.3	1	0	8.8	11.1
CHA-F(17,0%)	17	0.55	0.12	29.9	1	0	n.m.	n.m.
CHA-F(18,0%)	18	1.02	0.21	22.9	1	0	23.7	13.1

^a Units of k_{first}: 10⁻³ mol DME (mol H⁺ s kPa)⁻¹

^b Units of k_{zero}: 10⁻³ mol DME (mol H⁺ s)⁻¹

Table S3. Characterization of CHA zeolites synthesized with various Al precursors with equimolar Na⁺ and TMAda⁺ in OH⁻ media.

Synthesis	Characterization and Site Distribution						Kinetics	
Al Precursor	Si/Al _f	H ⁺ /Al _f	Micropore Volume / cm ³ g ⁻¹	Organic Content / wt%	Aiso/Alf	A _{pair} /Al _f	k _{first} a	kzero ^b
AlCl ₃	11	1.05	0.14	n.m.	0.80	0.20	n.m.	n.m.
NaAlO_2	16	1.42	0.02	19.5	0.62	0.38	n.m.	n.m.
Al(O-i-Pr) ₃	14	1.00	0.16	19.8	0.56	0.44	85.0	40.1
Al_2O_3	18	0.17	0.18	22.1	1.00	0.00	n.m.	n.m.
$Al(NO_3)_3$	19	0.65	0.21	20.0	0.80	0.10	n.m.	n.m.
Al(OH) ₃	17	0.97	0.16	21.0	0.70	0.30	39.9	34.2

 $^{^{\}rm a}$ Units of $k_{\rm first}$: $10^{\text{-}3}$ mol DME (mol H^+ s kPa) $^{\text{-}1}$

Table S4. Characterization of CHA zeolites synthesized using Al(OH)₃ and equimolar Na⁺ and TMAda⁺ in OH⁻ media. Also included is CHA-OH(16,6%) zeolite, which was synthesized using TMAda⁺ and hexyldecyltrimethylammonium bromide (CTAB) in OH⁻ media.

	Characterization and Site Distribution						Kinetics		
Sample	Si/Al _f	H ⁺ /Al _f	Micropore Volume / cm³ g-1	Organic Content / wt%	Aiso/Alf	A _{pair} /Al _f	k _{first} a	kzero ^b	
CHA-OH(15,18%)	15	1.01	0.17	21.6	0.82	0.18	36.0	27.5	
CHA-OH(16,24%)	16	1.16	0.18	20.1	0.76	0.24	32.1	22.0	
CHA-OH(17,30%)	17	0.97	0.16	21.0	0.70	0.30	39.9	34.2	
CHA-OH(16,6%)	16 ^c	0.93°	0.18	n.m.	0.94	0.06	21.9	24.7	

^a Units of k_{first}: 10⁻³ mol DME (mol H⁺ s kPa)⁻¹

Table S5. Characterization of commercial MFI zeolites (Si/Al = 30-43).

	Characterization and Site Distribution						Kinetics	
Sample	Si/Al _{tot}	H+/Altot	Micropore Volume / cm ³ g ⁻¹	Organic Content / wt%	Aiso/Altot	Apair/Altot	k _{first} a	kzero ^b
MFI(30)	30	1.15	0.14	N/A	N/A	N/A	3.9	15.5
MFI(43)	43	0.85	0.16	N/A	N/A	N/A	4.4	14.4

 $^{^{\}rm a}$ Units of $k_{\rm first}$: $10^{\text{-}3}$ mol DME (mol H^+ s kPa) $^{\text{-}1}$

^b Units of k_{zero}: 10⁻³ mol DME (mol H⁺ s)⁻¹

^b Units of k_{zero}: 10⁻³ mol DME (mol H⁺ s)⁻¹

^c Per total Al. ²⁷Al NMR spectra not measured on CHA-OH(16,6%).

^b Units of k_{zero}: 10⁻³ mol DME (mol H⁺ s)⁻¹

S.2.2. X-Ray diffraction of MFI and CHA zeolites

Crystal topologies of H-form zeolites were assessed from powder X-ray diffraction (XRD) patterns measured on a Rigaku SmartLab X-ray diffractometer with a Cu K α radiation source (λ =0.154 nm) operated at 1.76 kW. Typically, 0.50 g of zeolite powder were loaded onto a sample holder (Rigaku) and the diffraction pattern was recorded from 4-40° 20 at a scan rate of 0.04° s⁻¹. Powder XRD patterns for all synthesized materials were compared to diffraction patterns for CHA (CHA) reported in the International Zeolite Association (IZA) structure database.³ All XRD patterns reported here are normalized such that the maximum peak intensity in each pattern is set to unity. Diffraction patterns of CHA and MFI zeolites are shown in Figures S1-S6.

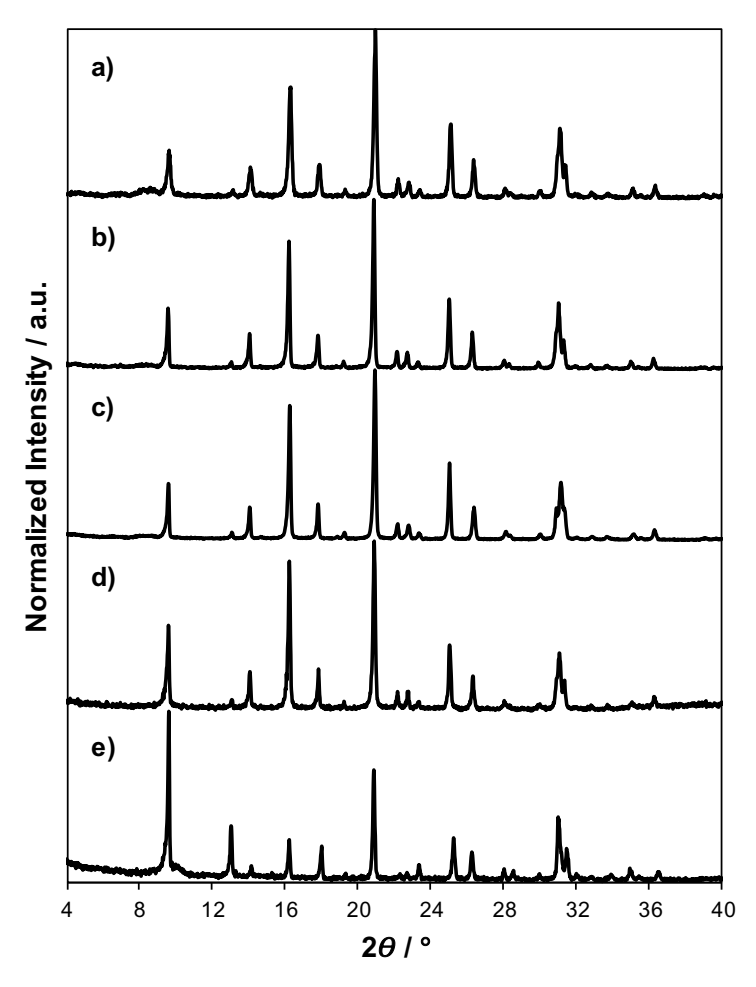


Figure S1. XRD patterns of a) CHA-F(18,0%), b) CHA-F(17,0%), c) CHA-OH(27,0%), d) CHA-OH(14,0%), and e) CHA-OH(17,0%) zeolites synthesized without Na^+ .

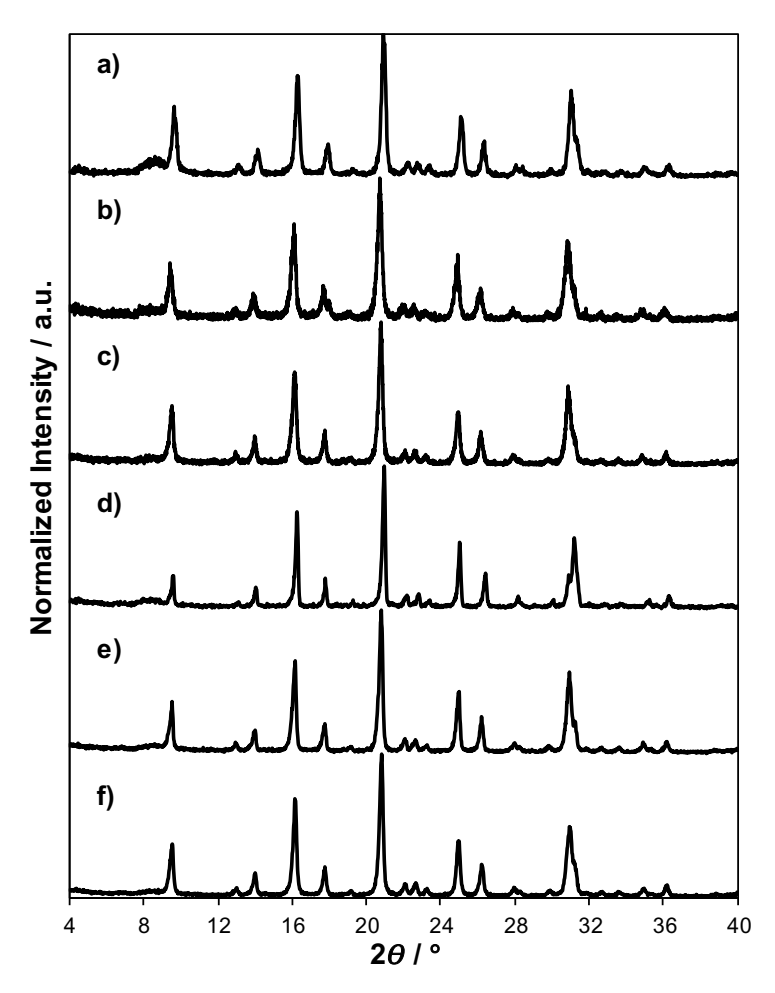


Figure S2. XRD patterns of CHA zeolites synthesized with a) AlCl₃, b) NaAlO₂, c) Al(O-i-Pr)₃, d) Al₂O₃, e) Al(NO₃)₃, and f) Al(OH)₃ and equimolar Na⁺ and TMAda⁺ in OH⁻ media.

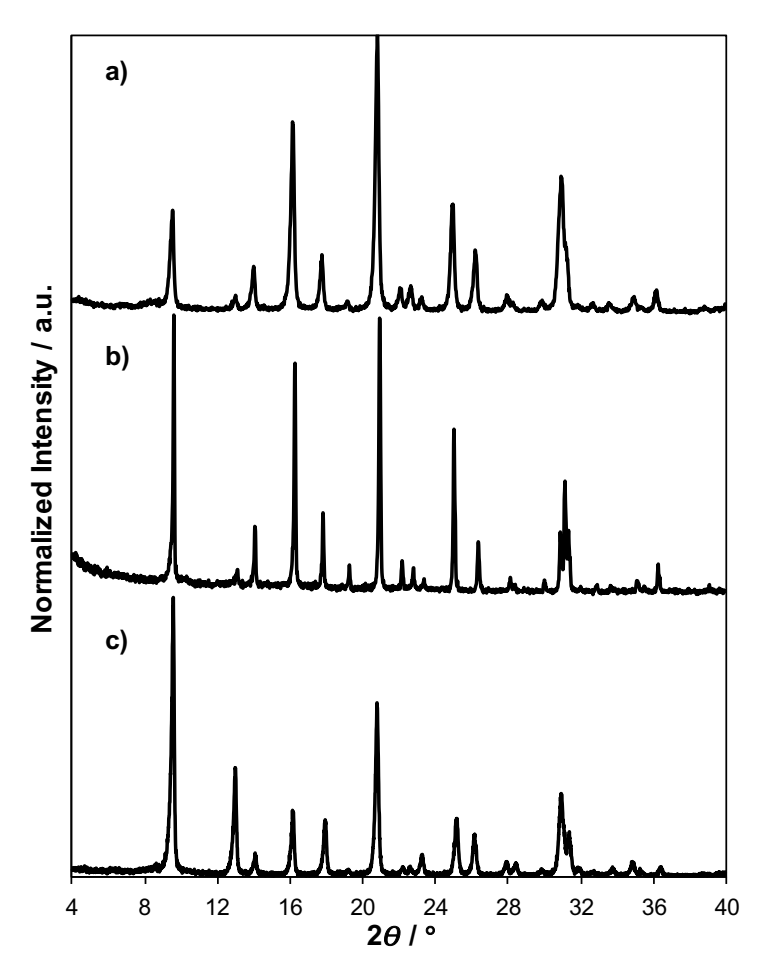


Figure S3. XRD patterns of a) CHA-OH(17,30%), b) CHA-OH(16,24%), and c) CHA-OH(15,18%) zeolites synthesized with Al(OH)₃ and equimolar Na⁺ and TMAda⁺ in OH⁻ media.

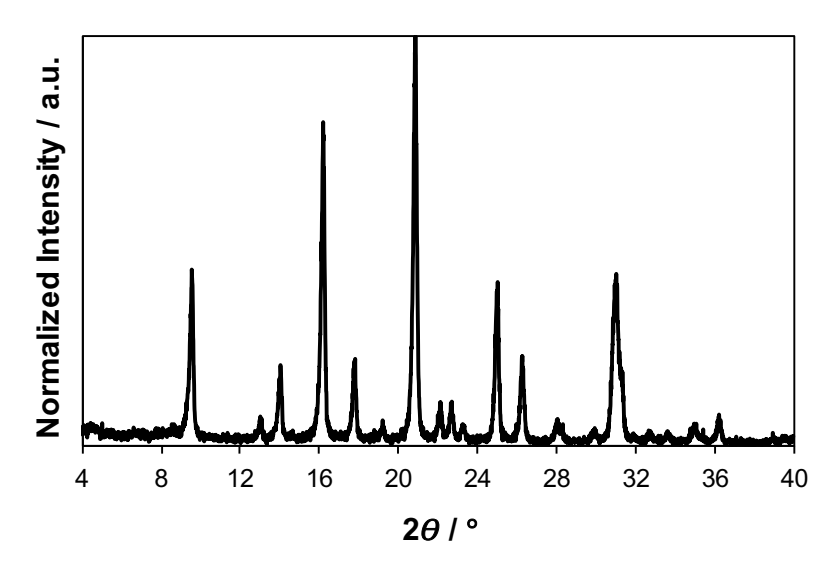


Figure S4. XRD patterns of Na⁺-free CHA-OH(16,6%) zeolite synthesized with Al(OH)₃, TMAda⁺, and CTAB in OH⁻ media.

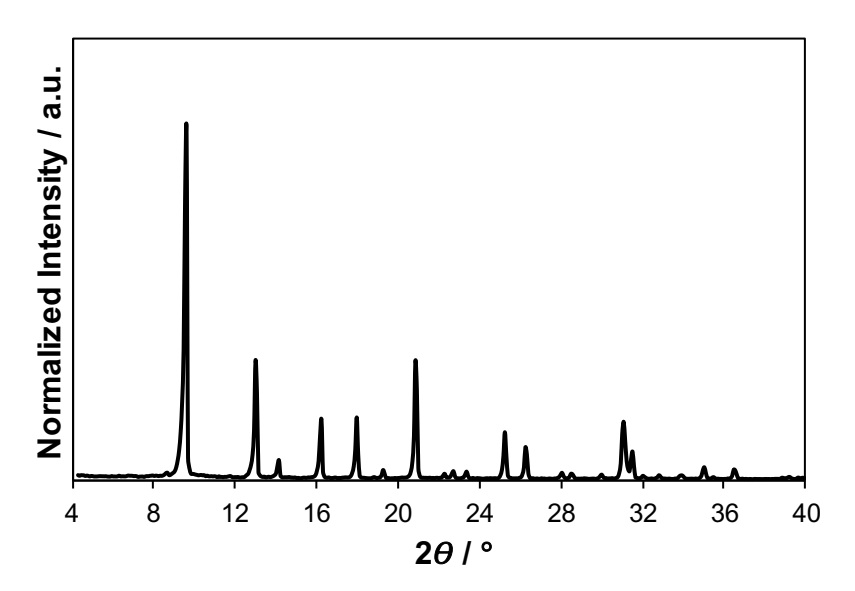


Figure S5. XRD pattern of Si-CHA synthesized with TMAda⁺ in F⁻ media.

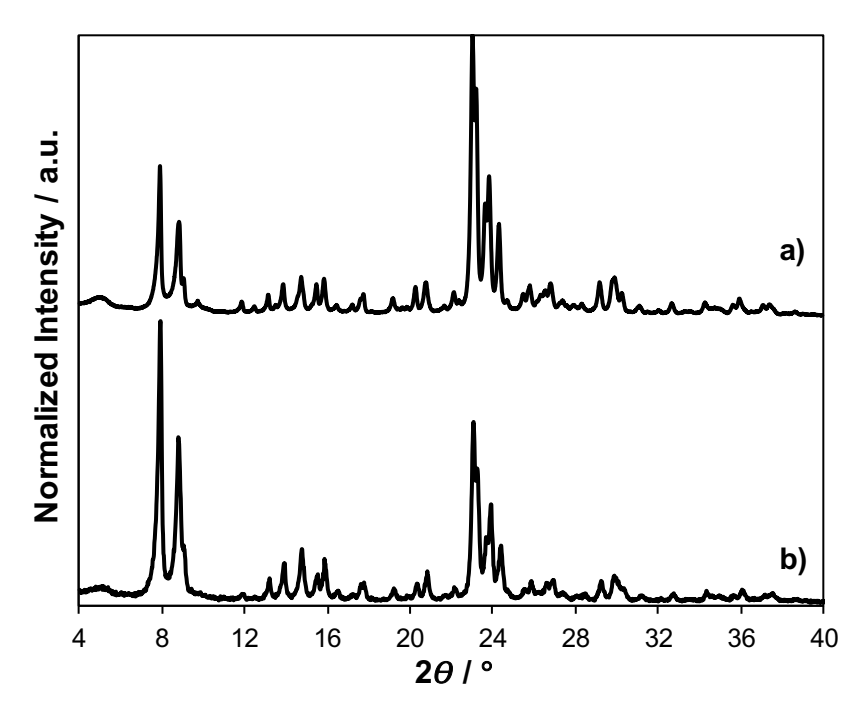


Figure S6. XRD patterns of a) H-MFI(30) and b) H-MFI(43) zeolites.

S.2.3. Adsorption isotherms to measure micropore volumes of CHA and MFI zeolites

Micropore volumes were determined on H-CHA zeolites from Ar adsorption isotherms measured at 87 K in a liquid Ar bath, and for H-MFI zeolites using N_2 adsorption isotherms held at 77 K in a liquid N_2 bath on a Micromeritics ASAP 2020 Surface Area and Porosity Analyzer. 0.03–0.05 g of sieved zeolite sample (nominal diameter between 180-250 μ m) were degassed by heating to 393 K (0.167 K s⁻¹) under vacuum (<5 μ mHg) for 2 h, and then further heating to 623 K (0.167 K s⁻¹) under vacuum (<5 μ mHg) and holding for 9 h. Standardized gas volumes (cm³ g_{cat}⁻¹ at STP) adsorbed were estimated from semi-log derivative plots of the adsorption isotherm (∂ (V_{ads})/ ∂ (ln(P/P_0)) vs. ln(P/P_0)). Micropore volumes (cm³ g_{cat}⁻¹ at STP) to liquid volumes using a density conversion factor assuming the liquid density of Ar at 87 K or N_2 at 77 K, respectively. Micropore volumes of CHA and MFI zeolites are shown in Figures S7-S12. In each figure, adsorption isotherms are offset in increments of 200 cm⁻³ g for clarity.

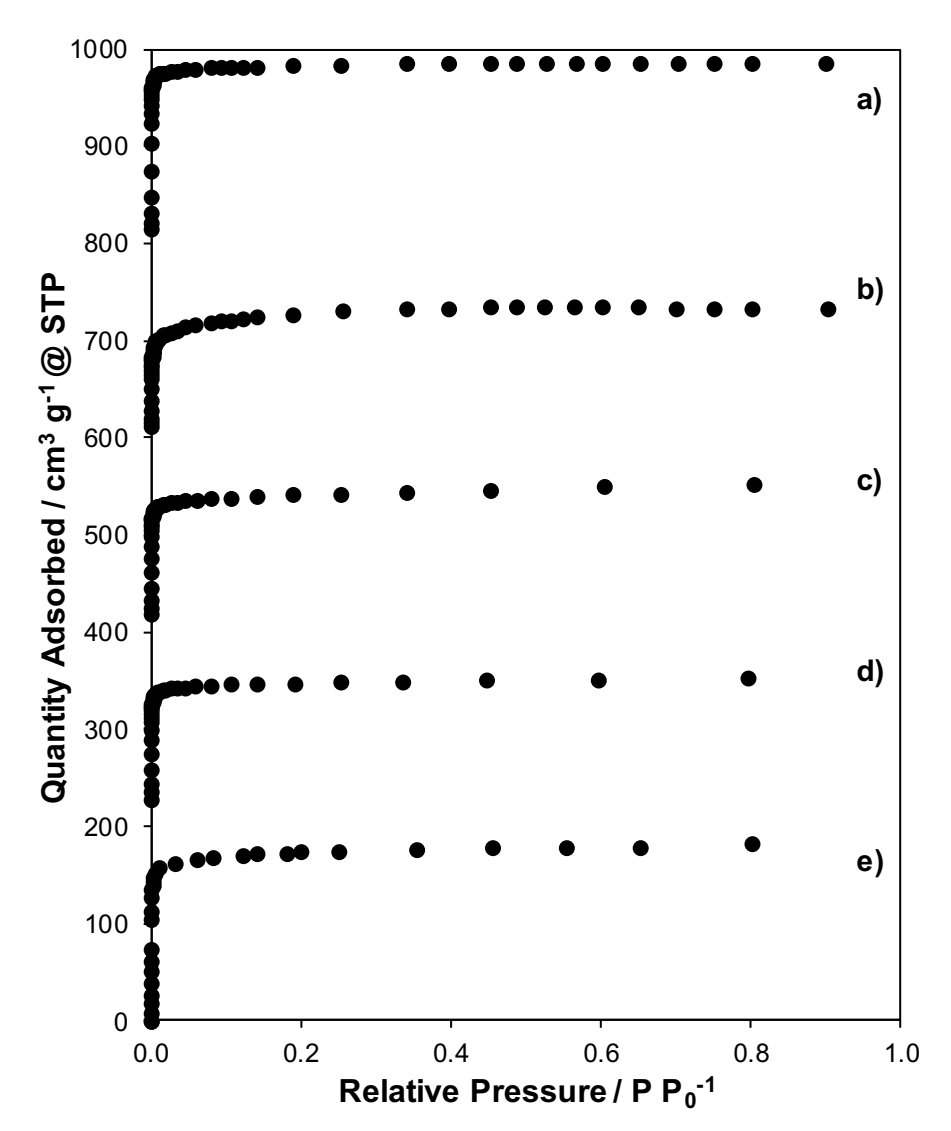


Figure S7. Ar adsorption isotherms (87 K) on a) CHA-F(18,0%), b) CHA-F(14,0%), c) CHA-OH(27,0%), d) CHA-OH(17,0%), and e) CHA-OH(18,0%) zeolites synthesized without Na⁺ using OH⁻ and F⁻ anions.

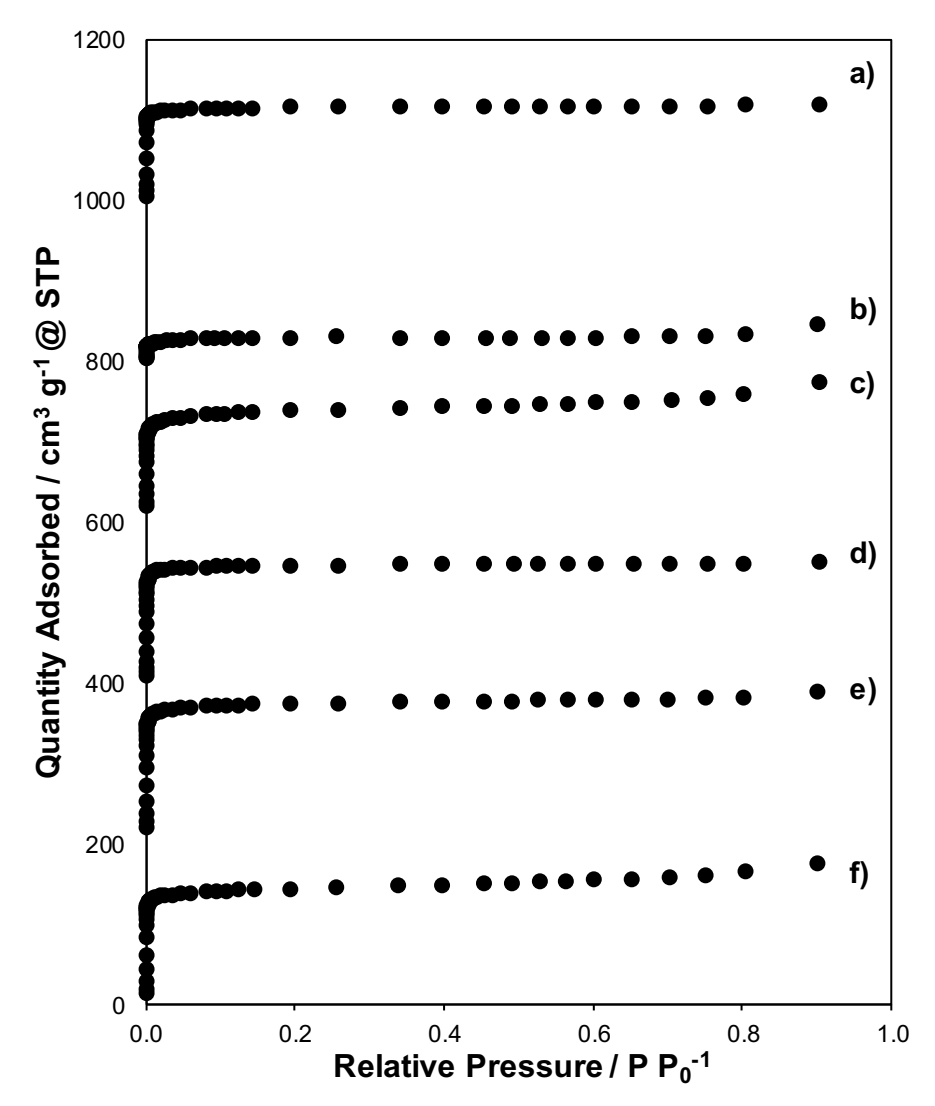


Figure S8. Ar adsorption isotherms (87 K) on CHA zeolites synthesized with a) AlCl₃, b) NaAlO₂, c) Al(O-i-Pr)₃, d) Al₂O₃, e) Al(NO₃)₃, and f) Al(OH)₃ and equimolar Na⁺ and TMAda⁺ in OH⁻ media.

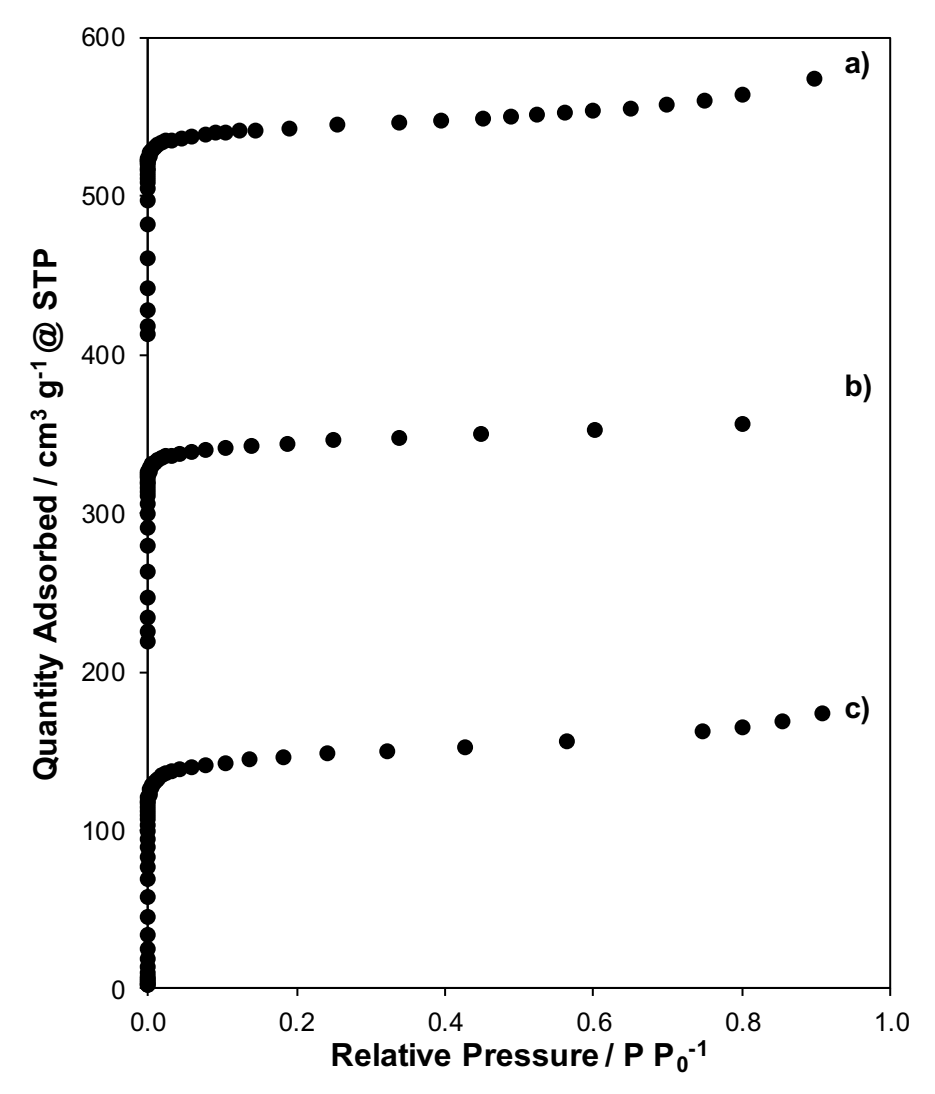


Figure S9. Ar adsorption isotherms (87 K) on a) CHA-OH(17,30%), b) CHA-OH(16,24%), and c) CHA-OH(15,18%) zeolites synthesized with Al(OH)₃ and equimolar Na⁺ and TMAda⁺ in OH-media.

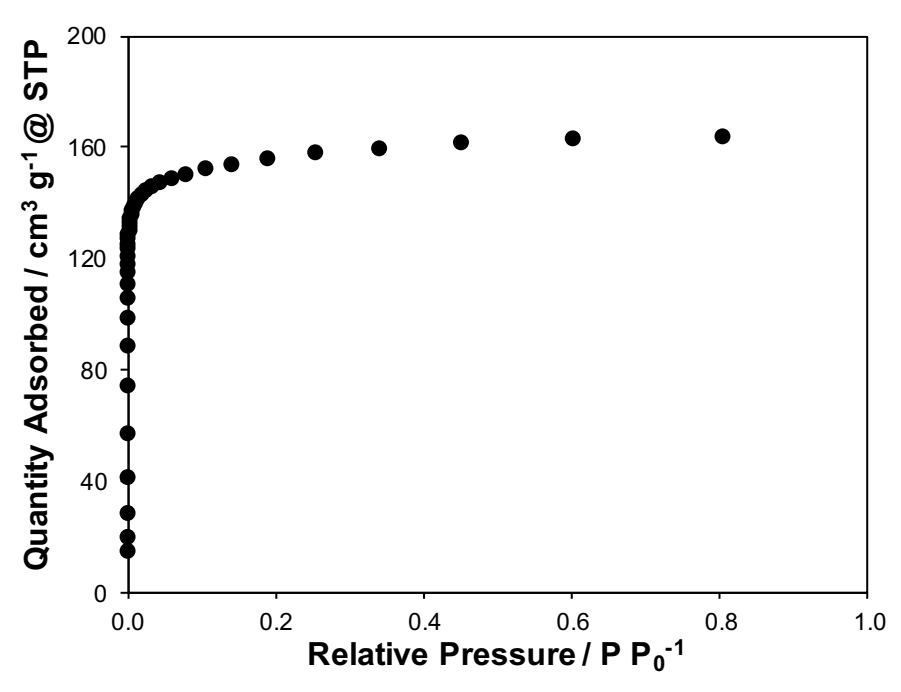


Figure S10. Ar adsorption isotherms (87 K) on Na+-free CHA-OH(16,6%) zeolite synthesized with Al(OH)₃, TMAda⁺, and CTAB in OH⁻ media.

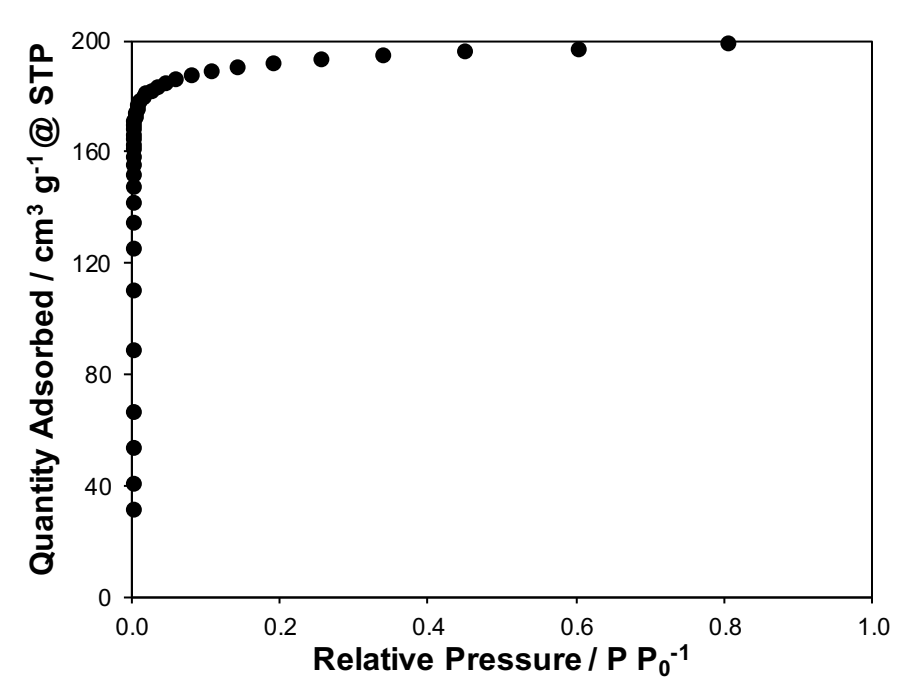


Figure S11. Ar adsorption isotherms (87 K) on Si-CHA zeolite synthesized with TMAda⁺ in F⁻ media.

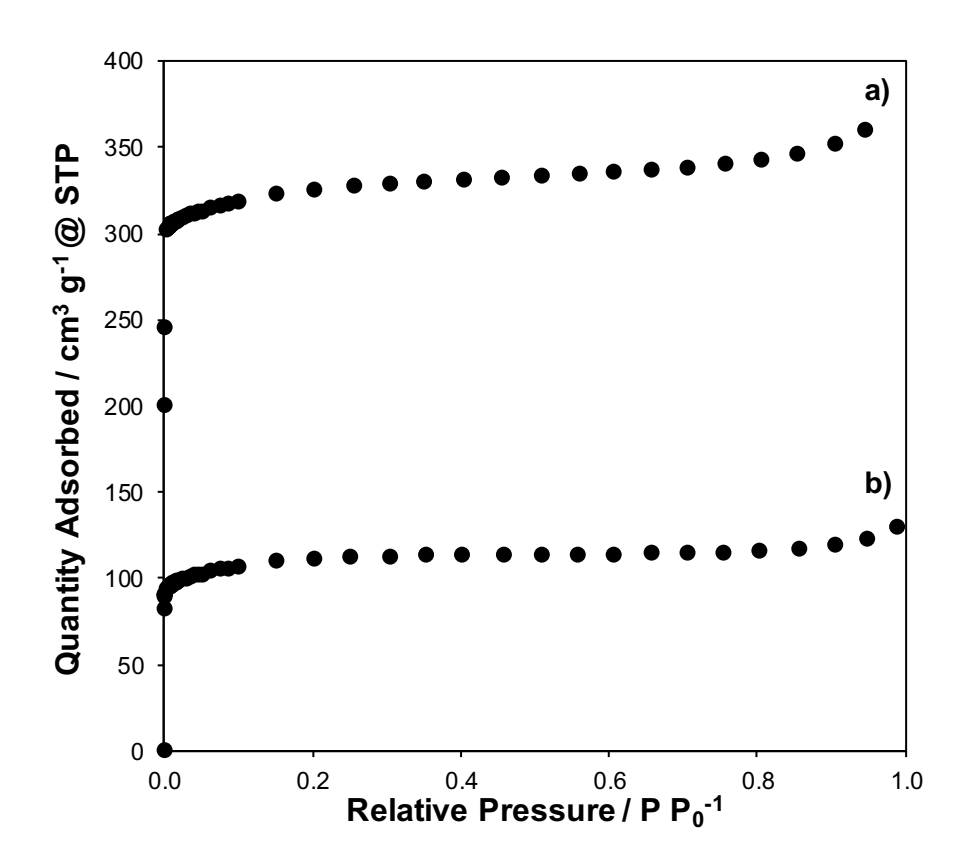


Figure S12. N₂ adsorption isotherms (77 K) on a) H-MFI(30) and b) H-MFI(43) zeolites.

S.2.4. Elemental analysis of CHA and MFI zeolites

Atomic absorption spectroscopy (AAS) was used to quantify the total Al, Na, and Co elemental content of each sample using a Perkin Elmer AAnalyst 300 Atomic Absorption Spectrometer. AAS samples were prepared by dissolving 0.02 g of zeolite in 3 g of concentrated HF acid (48 wt%, Sigma Aldrich), letting the solution sit overnight (at least 8 hours), and then diluting with 50 g of deionized water (18.2 MΩ). *Caution: when working with HF acid, use appropriate personal protective equipment, ventilation, and other safety measures.* Absorbances were measured using radiation sources at wavelengths of 309.3 nm for Al, in a reducing acetylene/nitrous oxide flame, and at 589.0 and 240.7 nm for Na and Co, respectively, in an oxidizing acetylene/air flame. Elemental compositions were determined from calibration curves derived from standard solutions of known composition. Al and Na contents were determined after removal of organic content in zeolites by oxidative treatment (853 K, 10 h).

S.2.5. Quantification of organic content in as-synthesized CHA zeolites

Thermogravimetric analysis (TGA) experiments were performed on as-synthesized CHA zeolites using a TA Instruments SDT Q600 thermogravimetric analyzer and differential scanning calorimeter (TGA-DSC) by heating 0.02 g of as-synthesized CHA in 83.3 cm³ s⁻¹ gcat⁻¹ dry air (UHP, 99.999%, Indiana Oxygen) to 523 K (0.167 K s⁻¹) and holding for 0.5 h to remove physisorbed water before further heating to 1073 K (0.167 K s⁻¹). Removal of the occluded TMAda⁺ molecule was characterized by a sharp exothermic heat flow centered around 773 K, which was accompanied by a sharp decrease in mass. All CHA zeolite samples exhibited a weight loss of about 20% due to combustion of one TMAda⁺ molecule per CHA cage, consistent with reported organic weight loss of CHA zeolites synthesized with TMAda⁺.4,5

S.2.6. Estimation of CHA crystal diameter using SEM and DLS

Scanning electron microscopy (SEM) micrographs of H-CHA zeolites were taken on a FEI Quanta 3D FEG Dual-beam SEM with an Everhart-Thornley attachment for high vacuum imaging and images were taken using the focused beam mode at 5 kV with a 3 µm spot size. Crystal diameters of all CHA zeolites were estimated by averaging over a distribution of individual crystals (~40-50) taken from multiple micrographs of different regions of the SEM slide. SEM micrographs shown in Figures S13-S21 are representative images of each sample.

SEM images of CHA-OH(14-27,0%) (Figures S13-S15) and CHA-F(18,0%) (Figure S16) show the presence of cubic crystal formations typical of CHA zeolites, but all images also contain smaller particles that appear to be under-developed crystals. Despite the non-uniformity of the crystal size distribution, XRD patterns show that CHA-OH(14-27,0%) zeolites are free of phase impurities. Images of CHA-OH(15,18%) and CHA(16,24%) show a more uniform distribution of crystal sizes (Figures S17-S18) than Na⁺-free CHA zeolites, but there do appear to be aggregates of very small particles (<250 nm) distributed throughout the sample. These small particles were not including in the average diameter of these CHA samples, which would result in an overestimation of the average crystal diameter and, due a larger estimated diffusion path length, would lead to a larger Thiele modulus (further discussion in Section S.5). CHA-OH(17,30%) and CHA-OH(14,44%) appear to be completely composed of aggregates of smaller, crystalline CHA zeolites (Figures S19-S20). Determination of the average crystal diameter was difficult due to the overlapping of crystal agglomerates and the diameter was conservatively estimated from intermediate sized aggregates consisting of a few smaller particles. CHA-OH(16,6%) zeolites synthesized from TMAda⁺ and CTAB contain smooth crystals and have a very uniform distribution of particle sizes (Figure S21).

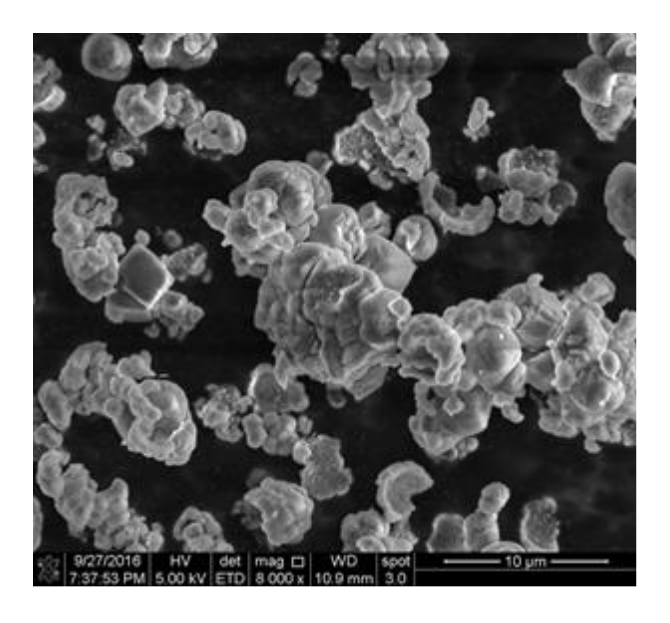


Figure S13. SEM image of the bulk sample of CHA-OH(14,0%).

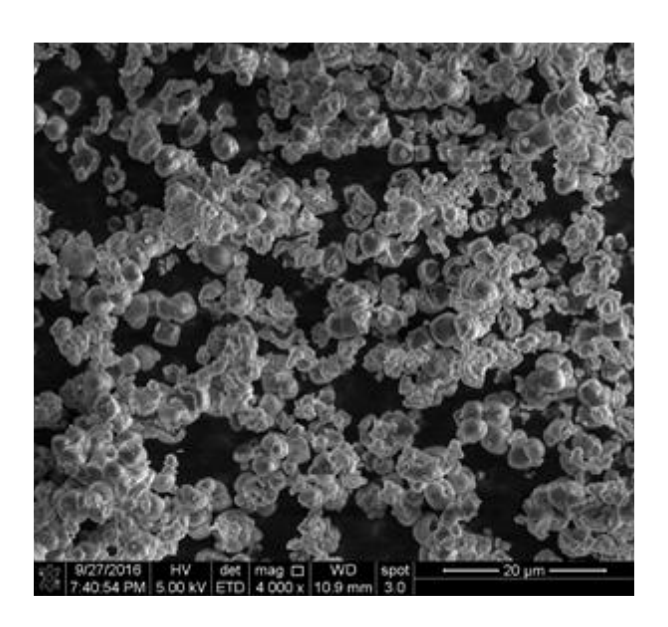


Figure S14. SEM image of the bulk sample of CHA-OH(17,0%).

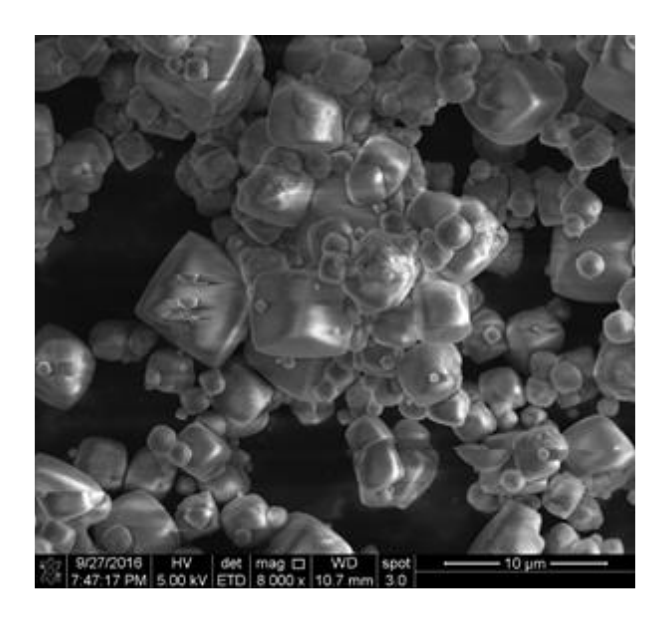


Figure S15. SEM image of the bulk sample of CHA-OH(27,0%).

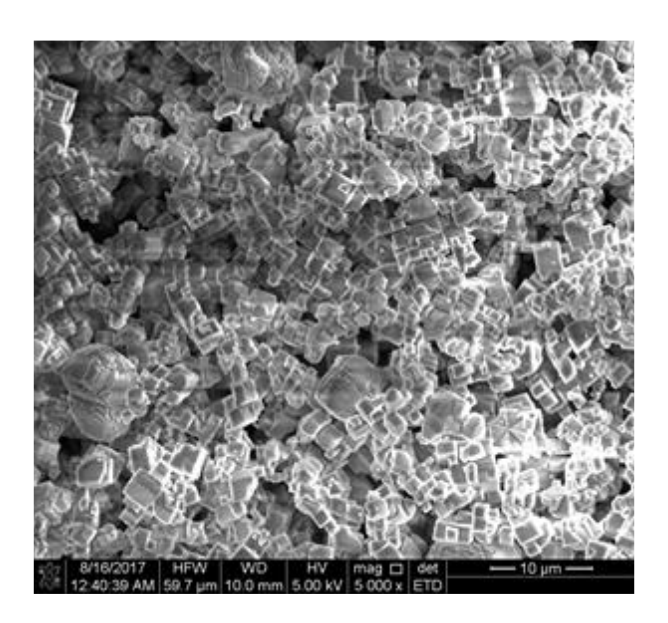


Figure S16. SEM image of the bulk sample of CHA-F(18,0%).

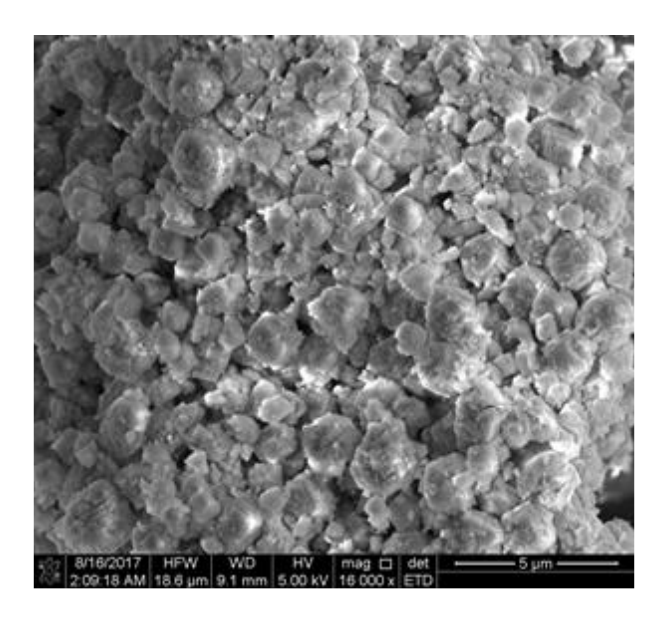


Figure S17. SEM image of the bulk sample of CHA-OH(15,18%).

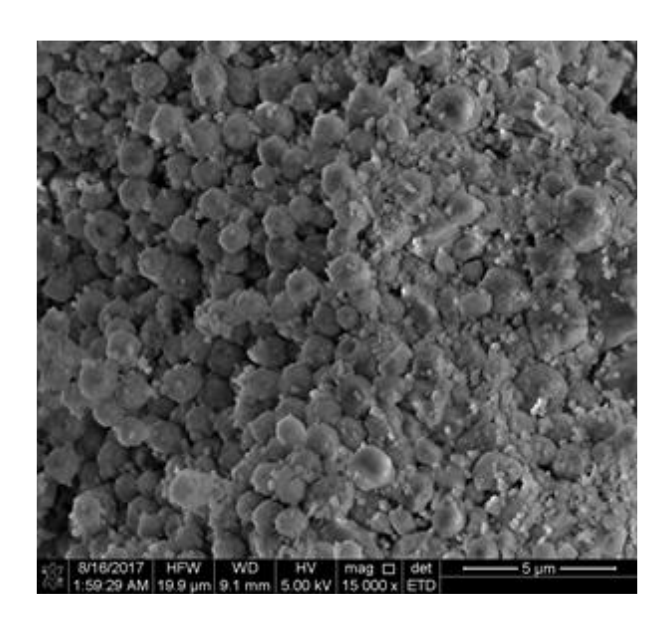


Figure S18. SEM image of the bulk sample of CHA-OH(16,24%).

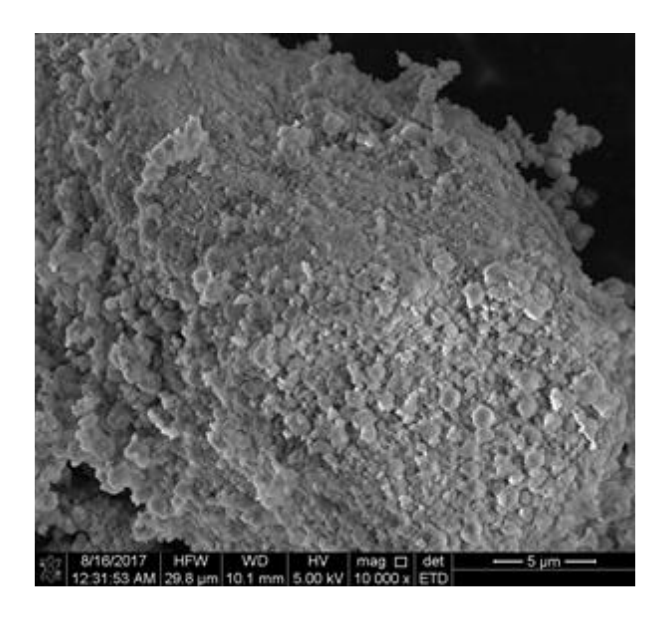


Figure S19. SEM image of the bulk sample of CHA-OH(17,30%).

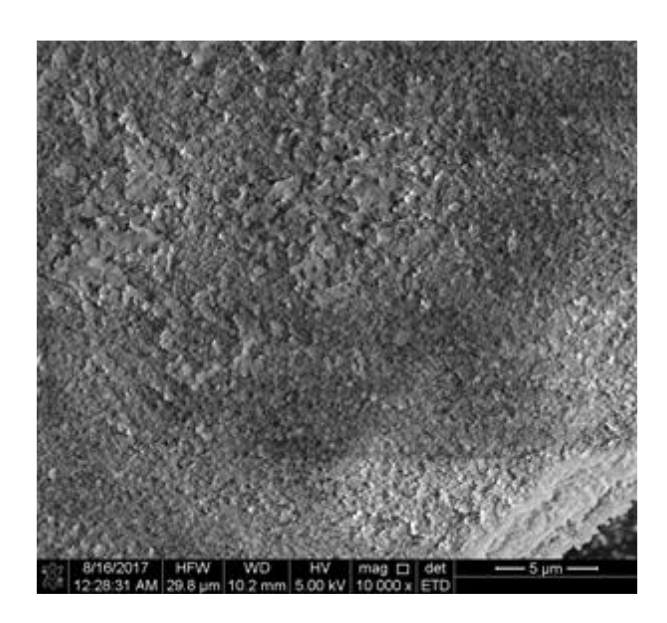


Figure S20. SEM image of the bulk sample of CHA-OH(14,44%).

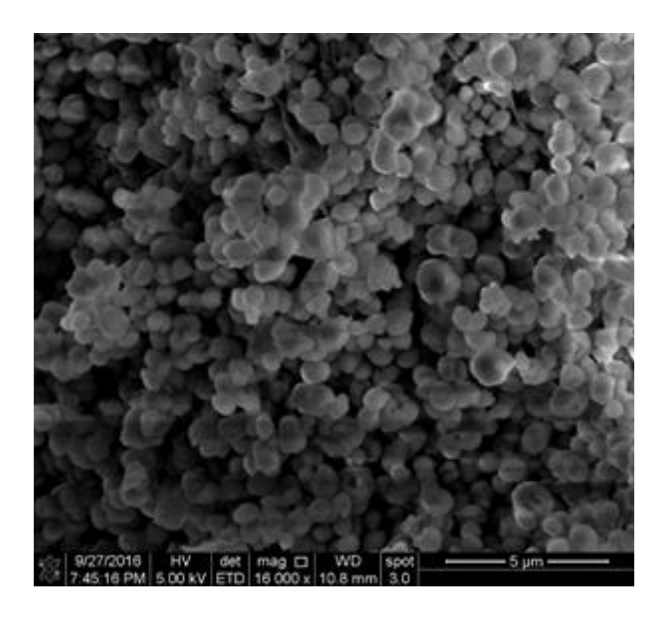


Figure S21. SEM image of the bulk sample of CHA-OH(16,6%).

Dynamic light scattering (DLS) was also used to estimate crystallite diameters and to corroborate particle size estimates from SEM micrographs. DLS measurements were performed on a Brookhaven ZetaPALS instrument at a wavelength of 659 nm at 298 K using the Particle Sizing Software (version 3.60). Zeolite samples were diluted with water until a translucent suspension was obtained (typically 1 mg zeolite per 20 cm³ H₂O), and suspended via agitation using a vortex mixer. Small aliquots (~4.5 cm³) of the zeolite suspension were placed within square acrylic cuvette cells prior to analysis. DLS measurements were recorded over a 10 minute period and averaged over three repeat measurements. Table S6 lists the crystallite diameters measured from DLS and from SEM micrographs for the samples listed in Table 1 of the main text.

Table S6. Crystallite diameters (μ m) of CHA zeolites with different fractions of paired Al (Table 1, main text) estimated from DLS and SEM micrographs.

Sample	SEM / μm	DLS / μm
CHA-OH(14,0%)	2±1	1.5±0.3
CHA-OH(17,0%)	2±1	n.m.
CHA-OH(27,0%)	6±1	4.6 ± 1.8
CHA-F(18,0%)	1±1	n.m.
CHA-OH(16,6%)	0.8 ± 1	0.8 ± 0.2
CHA-OH(15,18%)	1±1	1.1±0.3
CHA-OH(16,24%)	1±1	1.6±0.4
CHA-OH(17,30%)	1±1	0.9 ± 0.4
CHA-OH(14,44%)	0.3±1	0.7±0.3

S.2.7. Quantification of H⁺ sites by NH₃ TPD

The number of H⁺ sites on H-zeolites was quantified by NH₃ TPD after aqueous ion-exchange with NH₄⁺, while the number of H⁺ sites remaining after Cu or Co-exchange of CHA zeolites was quantified using gas-phase NH₃ titration and purge treatments shown to retain only NH₄⁺ species, as reported elsewhere.^{6,7} Briefly, gas-phase titrations were performed by saturating zeolite samples (0.03-0.05 g) in flowing gaseous NH₃ (500 ppm NH₃ in balance He, Matheson) at 433 K for 4 h and a total flow rate of 20 cm³ s⁻¹ g⁻¹. NH₃-saturated samples were then purged in wet, flowing He (~3% H₂O, 20 cm³ s⁻¹ g⁻¹) at 433 K for 8 h prior to TPD. Data for each sample in Tables S2-S5 (H⁺ per Al_f) and in Tables S7-S9 (H⁺ per Al_{tot}).

S.2.8. ²⁷Al MAS NMR to characterization Al coordination environment

²⁷Al magic angle spinning nuclear magnetic resonance (MAS NMR) spectra were recorded under ambient conditions on H-CHA zeolites to quantify framework and extraframework Al fractions. Spectra were recorded on a Chemagnetics CMX-Infinity 400 spectrometer in a widebore 9.4 Tesla magnet (Purdue Interdepartmental NMR Facility) and were acquired using a 2.3 μs pulse (~30 degrees), an acquisition time of 12.8ms and a relaxation delay of 1s, and were measured at 104.24 MHz and a MAS rate of 5 kHz. ¹H decoupling was used during acquisition, employing a two-pulse phase modulation (TPPM) scheme. Samples were hydrated by storing for >48 h in a hydrator containing a saturated potassium chloride (KCl) solution prior to packing in a 4mm ZrO₂ rotor. All ²⁷Al MAS NMR spectra are referenced to a static sample of AlCl₃ dissolved in D₂O (0 ppm ²⁷Al line). Spectra are normalized so that the maximum intensity in each spectrum is set to unity and are shown in Figures S22-S24. Fractions of framework (Al_f) and extraframework Al (Al_{ex}) per total Al are listed in Tables S7-S9 and the error associated with each is ±0.05

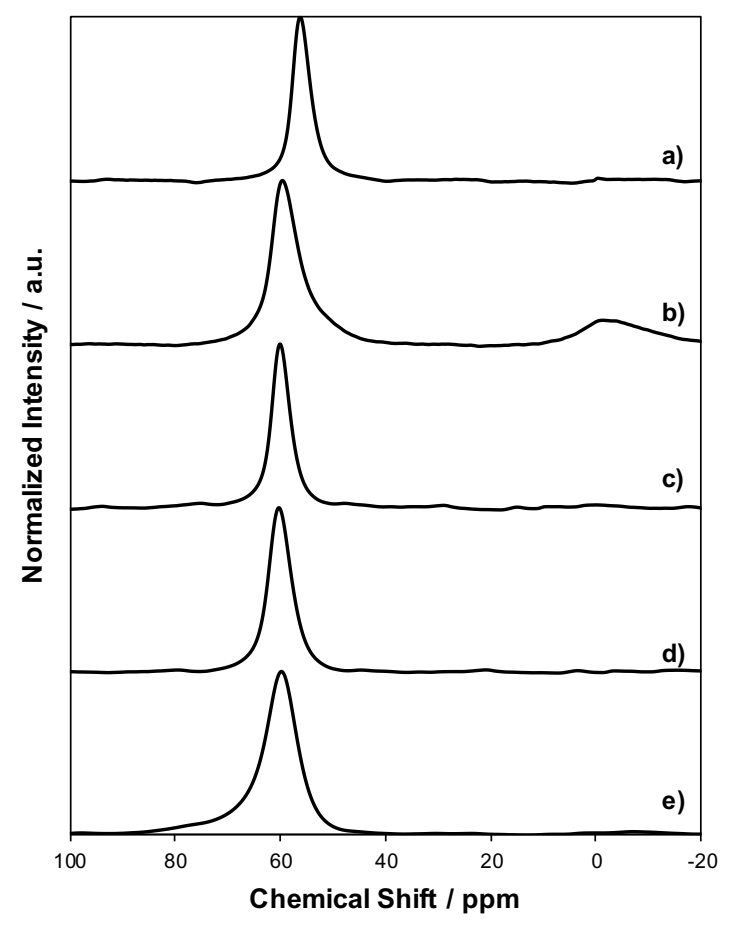


Figure S22. ²⁷Al MAS NMR spectra of a) CHA-F(18,0), b) CHA-F(17,0), c) CHA-OH(27,0), d) CHA-OH(14,0), and e) CHA-OH(17,0) zeolites synthesized without Na⁺ using OH⁻ and F⁻ anions.

Table S7. Fraction of framework Al atoms (Al_f/Al_{tot}) from ^{27}Al NMR and H^+/Al_f for each CHA zeolites synthesized without Na⁺ in OH⁻ and F⁻ media.

Sample	Si/Al _{tot}	H ⁺ /Al _{tot}	A _f /Al _{tot}	Si/Al _f	H ⁺ /Al _f
CHA-OH(14,0%)	14	0.95	1.00	14	0.95
CHA-OH(17,0%)	16	0.96	0.95	17	1.00
CHA-OH(27,0%)	26	0.97	0.97	27	1.00
CHA-F(17,0%)	14	0.44	0.80	17	0.55
CHA-F(18,0%)	18	1.02	1.00	18	1.02

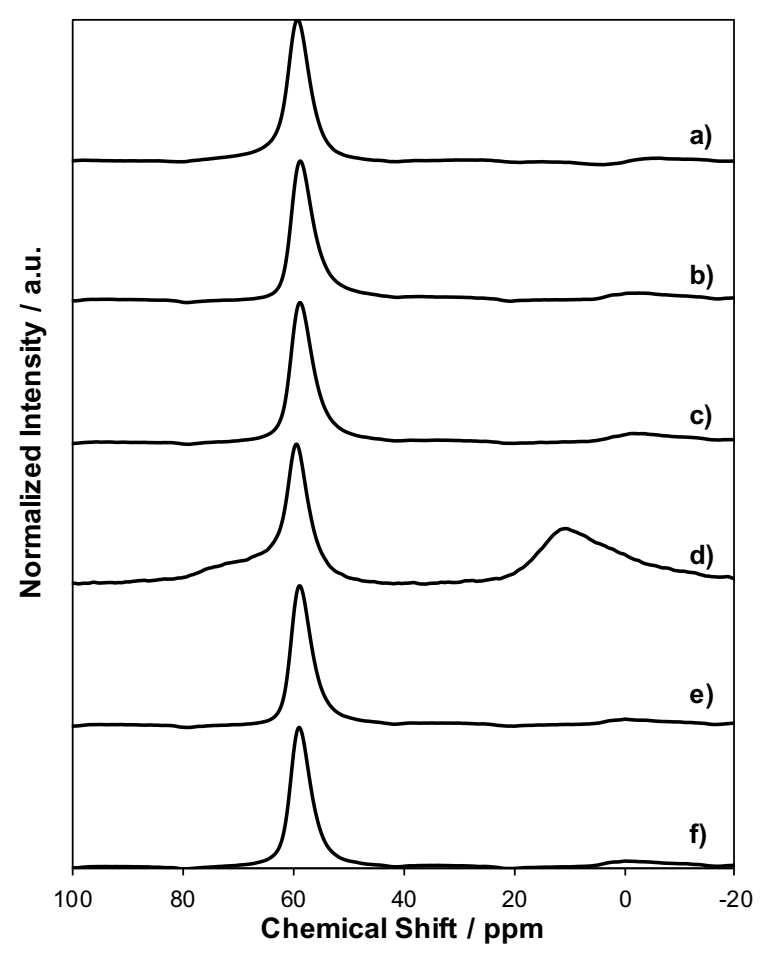


Figure S23. ²⁷Al MAS NMR spectra of CHA zeolites synthesized with a) AlCl₃, b) NaAlO₂, c) Al(O-i-Pr)₃, d) Al₂O₃, e) Al(NO₃)₃, and f) Al(OH)₃ and equimolar Na⁺ and TMAda⁺ in OH⁻ media.

Table S8. Fraction of framework Al atoms (Al_f/Al_{tot}) from 27 Al NMR and H⁺/Al_f for each CHA zeolites synthesized with various Al precursors and equimolar amounts of Na⁺ and TMAda⁺ in OH⁻ media.

Al Precursor	Si/Altot	H ⁺ /Altot	A _f /Al _{tot}	Si/Al _f	H ⁺ /Al _f
AlCl ₃	11	1.02	0.97	11	1.05
NaAlO_2	13	1.18	0.83	16	1.42
Al(O-i-Pr) ₃	12	0.83	0.83	14	1.00
Al_2O_3	9	0.09	0.52	18	0.17
$Al(NO_3)_3$	16	0.55	0.85	19	0.65
Al(OH) ₃	15	0.84	0.87	17	0.97
		•			

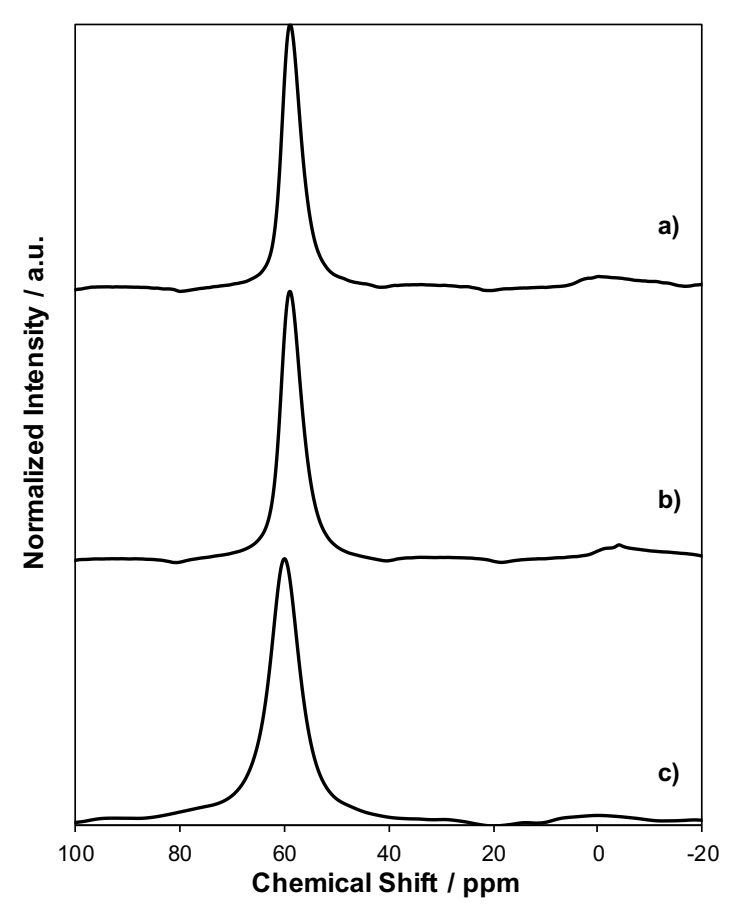


Figure S24. ²⁷Al MAS NMR spectra of a) CHA-OH(17,30%), b) CHA-OH(16,24%), and c) CHA-OH(15,18%) zeolites synthesized with Al(OH)₃ and equimolar Na⁺ and TMAda⁺ in OH⁻ media.

Table S9. Fraction of framework Al atoms (Al $_f$ /Al $_{tot}$) from 27 Al NMR and H $^+$ /Al $_f$ for different CHA zeolites synthesized with equimolar amounts of Na $^+$ and TMAda $^+$ in OH $^-$ media.

Sample	Si/Al _{tot}	H ⁺ /Al _{tot}	A _f /Al _{tot}	Si/Al _f	H ⁺ /Al _f
CHA-OH(15,18%)	15	0.99	0.98	15	1.01
CHA-OH(16,24%)	14	1.02	0.88	16	1.16
CHA-OH(17,30%)	15	0.84	0.87	17	0.97

S.2.9. Validation of Co²⁺ titration procedures on H-CHA-F zeolites

CHA zeolites crystallized with only TMAda⁺ cations in F⁻ media at Si/Al<15 contained a large fraction of Al atoms unable to stabilize NH₄⁺ cations (H⁺/Al_{tot} = 0.44), consistent with previous observations suggesting that TMAda⁺ cations alone are unable to stabilize CHA zeolites with Si/Al<15.1 CHA-F zeolites with Si/Al>15 contained nearly all of their Al atoms in the framework (H⁺/Al_{tot} = 1.02 from NH₃ titrations; Table S2), yet were unable to exchange divalent Co²⁺ cations. Co²⁺ exchange isotherms (0.25-1M Co(NO₃)₂, 150 cm³ solution g⁻¹, ambient temperature, no pH adjustment) were measured at different conditions (Co²⁺ molarity, repeat exchanges) to assess whether Co²⁺ exchange behavior was influenced by the hydrophobic nature of the framework resulting from fluoride-assisted crystallization.² Saturation Co²⁺ exchange capacities of zero, within experimental error, were measured for all H-CHA-F zeolites (Figure S25 and S.26). To further demonstrate that H-CHA-F zeolites contain only isolated Al atoms, Cu²⁺ ionexchanges were performed and the residual number of H⁺ sites, remaining after Cu²⁺-exchange, were quantified with gas-phase NH₃ titrations using previously reported procedures to determine the Cu-exchange stoichiometry (Table S10). Cu-exchange and subsequent NH₃ titration data on CHA-OH(16,24%)⁸ and CHA-OH(14,0%)¹ zeolites are included as references for CHA zeolites containing exclusively Cu²⁺ and [CuOH]⁺, respectively. Both CHA-F zeolites (Si/Al = 17-18) contain exclusively isolated [CuOH]⁺ cations, consistent with the 1 H⁺ per Cu²⁺ exchange stoichiometry (Table S10, Figure S27), indicating that all framework Al is present as isolated sites. The possibility that [CuOH]⁺ preferentially exchanges before divalent Cu²⁺ cations is inconsistent with experimentally-measured Cu²⁺-exchange isotherms (stoichiometry determined from NH₃ titration), and DFT-calculated adsorption energies show that Cu²⁺ preferentially exchanges at paired Al sites before [CuOH]⁺ species exchange at isolated H⁺ sites.⁸

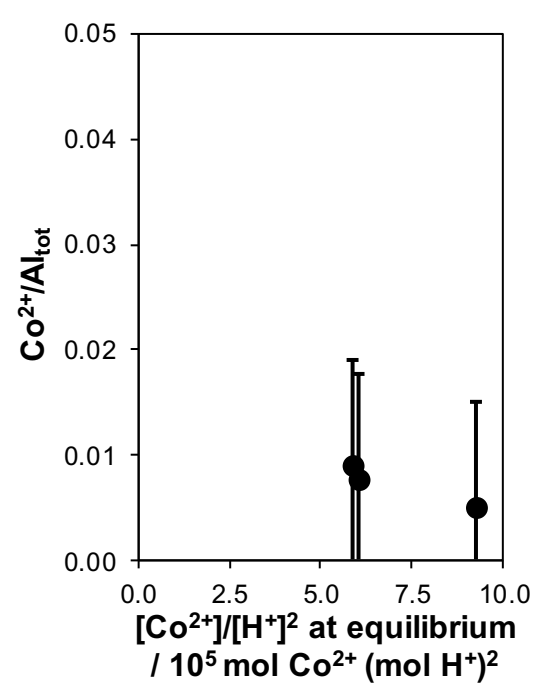


Figure S25. Amount of exchanged Co²⁺ retained on H-CHA-F(18,0%) as a function of the Co²⁺ concentration in solution at equilibrium.

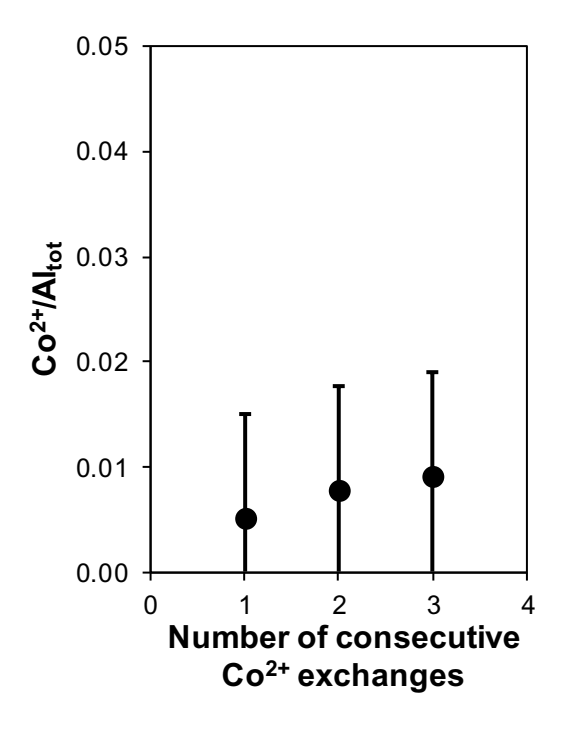


Figure S26. Amount of Co retained on H-CHA-F(18,0%) as a function of successive Co^{2+} titrations with a 0.5M $Co(NO_{3)2}$ solution.

Table S10. Titration of residual H^+ sites on CHA-OH(16,24%), CHA-OH(14,0%), CHA-F(17,0%), and CHA-F(18,0%) after Cu^{2^+} ion-exchange.

Sample	Si/Altot	H ⁺ /Al _{tot} (on H-form)	Cu wt%	Cu/Altot	Measured H ⁺ /Al _{tot} ^a	H ⁺ /Cu
CHA-OH(16,24%)	14	1.02	0.2	0.03	0.95	2.3
CHA-OH(14,0%)	14	0.95	0.8	0.11	0.82	1.2
CHA-F(17,0%)	14	0.44	0.7	0.10	0.36	0.8
CHA-F(18,0%)	17	1.02	0.7	0.12	0.93	0.8

^a H⁺/Al_{tot} measured on Cu-exchanged CHA zeolites

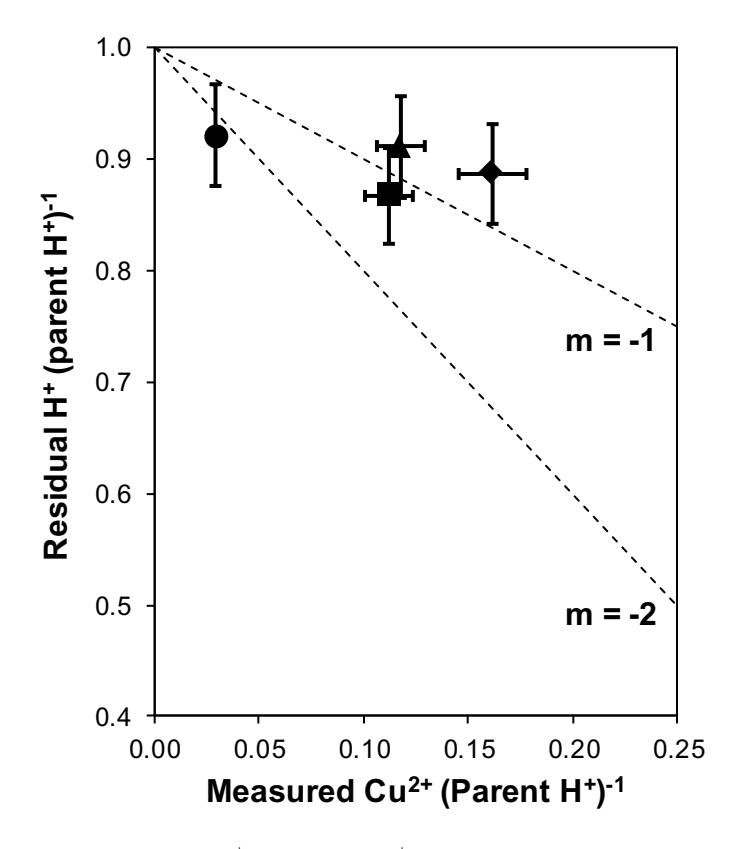


Figure S27. The number of residual H^+ sites (per H^+ site on the H-form parent zeolite) as a function of the Cu-loading (per H^+ site on the H-form parent zeolite) for CHA-OH(16,24%) (circle), CHA-OH(14,0%) (square), CHA-F(17,0%) (diamond), and CHA-F(18,0%) (triangle) zeolites. Dashed lines represent the expected exchange stoichiometry for exclusively Cu^{2+} (m = -2) or $[CuOH]^+$ (m = -1).

Section S.3. Methanol dehydration catalysis

S.3.1. Derivation of the associative methanol dehydration rate expression

A rate expression can be derived for the associative pathway using the pseudo-steady state hypothesis (PSSH) on reactive surface intermediates, and from assumptions about the irreversible or quasi-equilibrated nature of elementary steps. The concentrations of all surface intermediates (defined using square brackets), at steady-state, are described using PSSH:

$$\frac{d[c_{j^*}]}{dt} \approx 0 \tag{S1}$$

where $[C_j^*]$ is the concentration of surface species j. Density functional theory calculations show that the formation of dimethyl ether from the methanol-pair intermediate is irreversible and the rate-limiting elementary step for the associative dehydration pathway⁹ and, as a result, the net rate of dimethyl ether formation from the associative pathway $(r_{DME,A})$ can be expressed by the following expression:

$$r_{DME,A} = k_{DME,A}[P *]$$
 (S2)

Applying PSSH to the M*, D*, and P* intermediates, defined in the sequence of elementary steps in Scheme 2 (main text), yields the following expressions:

$$\frac{d[M*]}{dt} = k_M P_{CH_3OH}[*] + k_{-D}[D*] - k_{-M}[M*] - k_D P_{CH_3OH}[M*] \approx 0$$
 (S3)

$$\frac{d[D*]}{dt} = k_D P_{CH_3OH}[M*] + k_{-P}[P*] - k_{-D}[D*] - k_P[D*] \approx 0$$
 (S4)

$$\frac{d[P^*]}{dt} = k_P[D^*] - k_{-P}[P^*] - k_{DME,A}[P^*] \approx 0$$
 (S5)

where k_j and k_{-j} are the forward and reverse rate constants for each elementary step, respectively, and P_{CH3OH} is the gas phase methanol partial pressure. Assuming that methanol monomers and gas-phase methanol, methanol monomers and protonated dimers, and the intermediate methanol pairs and protonated dimers are all in quasi-equilibrium with each other, based on density

functional theory calculations performed on unconfined, isolated H^+ sites, 9 steady-state surface concentrations are given by the representative equilibrium constants (K_j) :

$$[M *] = \frac{k_M}{k_{-M}} P_{CH_3OH}[*] = K_M P_{CH_3OH}[*]$$
(S6)

$$[D *] = \frac{k_D}{k_{-D}} P_{CH_3OH}[M *] = K_D K_M P_{CH_3OH}^2[*]$$
(S7)

$$[P *] = \frac{k_P}{k_{-P}}[D *] = K_P K_D K_M P_{CH_3OH}^2[*]$$
(S8)

Substituting the expression for [P*] (Eq. S8) into Eq. S2, the rate expression become second-order in methanol partial pressure:

$$r_{DME,A} = k_{DME,A} K_P K_D K_M P_{CH_3OH}^2[*]$$
 (S9)

where the concentration of empty sites ([*]) can be defined using a site balance to conserve the total number of sites involved in the reaction:

$$[L] = [*] + [M *] + [D *] + [P *] + [E *]$$
(S10)

Here, [L] represents the total number of active sites (accessible to reactants) and can be quantified through direct titration by amine bases (e.g. *ex situ* NH₃ titration, *in situ* pyridine titration). The total number of empty sites is assumed to be negligible because equilibrium between gas-phase methanol and vacant H⁺ sites and adsorbed methanol monomers (Step 1 in Scheme 2) favors the formation of methanol monomers adsorbed at H⁺ sites (K_M>>1),⁹ consistent with the observation that bridging OH vibrational bands are immediately and completely perturbed upon contact with gas-phase methanol during *in situ* IR experiments (Figure S39-S.41).¹⁰ The concentration of dimethyl ether ([E*]) and methanol-pair intermediates ([P*]) are also assumed to be negligible because equilibrium concentrations favor protonated methanol dimers and desorption of dimethyl ether into the gas-phase.⁹ With these assumptions and substitution of Eqs. S6 and S7 into the site

balance (Eq. S10), an expression for the concentration of empty sites can be obtained when methanol monomers and protonated dimers are the most abundant surface intermediates (MASI):

$$[*] = \frac{[L]}{K_M P_{CH_3OH} + K_D K_M P_{CH_3OH}^2}$$
 (S11)

Substitution of Eq. S11 into Eq. S9, yields a rate law in terms of only measurable quantities, equilibrium, and rate constants:

$$\frac{r_{DME,A}}{[L]} = \frac{k_{DME,A}K_{P}K_{D}P_{CH_{3}OH}}{1 + K_{D}P_{CH_{3}OH}}$$
(S12)

This rate law can now be rearranged to yield an expression in terms of measurable first and zeroorder apparent rate constants:

$$\frac{r_{DME,A}}{[L]} = \frac{k_{first}P_{CH_3OH}}{1 + \frac{k_{first}}{k_{zero}}P_{CH_3OH}}$$
(S13)

where k_{first} is the apparent first order rate constant and given by:

$$k_{first} = k_{DME,A} K_P K_D \tag{S14}$$

and k_{zero} is the apparent zero-order rate constant and given by:

$$k_{zero} = k_{DME,A} K_P (S15)$$

S.3.2. Derivation of the inhibited associative methanol dehydration rate expression

In order to account for the observed inhibition in the dimethyl ether formation rate (415 K, per H⁺) at high methanol partial pressures, an additional term involving an inhibitory methanol species ([I*]) needs to be added to the associative rate law. An additional methanol adsorption step involving methanol adsorbed at existing methanol dimers to form an inhibitory methanol trimer can be added to the existing set of elementary steps. The justification for including this step is described in detail in Section S.6. This new adsorption step to form methanol clusters can be assumed to be in equilibrium with protonated methanol dimers and a gas-phase methanol species

and an equilibrium constant can be defined to describe the concentration of these species on the surface:

$$[I *] = \frac{k_I}{k_{-I}} [D *] P_{CH_3OH} = K_I K_D K_M P_{CH_3OH}^3 [*]$$
(S16)

Including these methanol clusters as a MASI species, along with methanol monomers and protonated dimers, a new site balance can be derived:

$$[*] = \frac{[L]}{K_M P_{CH_3OH} + K_D K_M P_{CH_3OH}^2 + K_P K_D K_M P_{CH_3OH}^3}$$
(S17)

Substitution of Eq. S17 into Eq. S9, yields a new rate law in terms of only measurable quantities, and rate and equilibrium constants:

$$\frac{r_{DME,A}}{[L]} = \frac{k_{DME,A} K_P K_D P_{CH_3OH}}{1 + K_D P_{CH_3OH} + K_I K_D P_{CH_3OH}^2}$$
(S18)

S.3.3. Derivation of the dissociative methanol dehydration rate expression

Rates of dimethyl ether formation via the dissociative pathway are governed by the rate at which methanol/methoxy pairs form dimethyl ether and, assuming this step to be irreversible, the rate expression becomes:

$$r_{DME,D} = k_{DME,D}[MMe*]$$
 (S19)

The elimination of water from methanol monomers to form surface methoxy groups can be considered irreversible, because the equilibrated adsorption of methanol at surface methoxy species and the subsequent reaction to form dimethyl ether are considered to be much faster than the hydration of surface methoxy species to form methanol. By applying PSSH to the M*, Me*, and MMe* intermediates, defined in Scheme 3 (main text), the following expressions are obtained:

$$\frac{d[M*]}{dt} = k_M P_{CH_3OH}[*] - k_{-M}[M*] - k_{elim}[M*] \approx 0$$
 (S20)

$$\frac{d[Me*]}{dt} = k_{elim}[M*] + k_{-MMe}[MMe*] - k_{MMe}[Me*] P_{CH_3OH} \approx 0$$
 (S21)

$$\frac{d[MMe^*]}{dt} = k_{MMe}[Me^*] P_{CH_3OH} - k_{DME,D}[MMe^*] - k_{-MMe}[MMe^*] \approx 0$$
 (S22)

where k_j and k_{-j} are the forward and reverse rate constants for each elementary step, respectively, and P_{CH3OH} is the gas phase methanol partial pressure. Eqs. S20- S22 can be rearranged to solve for [M*], [Me*], and [MMe*]:

$$[M *] = \frac{k_M P_{CH_3OH}[*]}{k_{-M} + k_{elim}}$$
 (S23)

$$[Me *] = \frac{k_{elim}[M*] + k_{-MMe}[MMe*]}{k_{MMe}P_{CH_3OH}}$$
(S24)

$$[MMe *] = \frac{k_{MME}[Me*]P_{CH_3OH}}{k_{DME,D} + k_{-MME}}$$
(S25)

Substitution of Eqs. S23 and S25 into Eq. S.24 yields an expression that can be explicitly solved for to find [Me*]:

$$[Me *] = \frac{k_{elim} \left(\frac{k_M[*]}{k_{-M} + k_{elim}}\right)}{k_{MMe}} \left(\frac{k_{DME,D} + k_{-MMe}}{k_{DME,D}}\right)$$
(S26)

Further substitution of Eq. S26 back into Eq. S25 results in an expression that can be solved explicitly for [MMe*]:

$$[MMe *] = \frac{k_{elim}}{k_{DME,D}} \left(\frac{k_M P_{CH_3OH}[*]}{k_{-M} + k_{elim}} \right)$$
 (S27)

The adsorption of methanol to form methanol monomers, protonated dimers, and methanol/methoxy pairs can be considered quasi-equilibrated relative to the formation of dimethyl ether and surface methoxy groups and as a result k_M , k_{-M} , k_{MMe} , and k_{-MMe} are much greater than k_{elim} and $k_{DME,D}$. This allows Eqs. S23, S26, and S27 to be written directly in terms of only forward rate constants, equilibrium constants, and measurable quantities:

$$[M *] = K_M P_{CH_3OH}[*]$$
 (S28)

$$[Me *] = \frac{k_{elim}K_M}{k_{DME}pK_{MMe}}[*]$$
 (S29)

$$[MMe *] = \frac{k_{elim}}{k_{DME,D}} K_M P_{CH_3OH}[*]$$
 (S30)

The formation of protonated dimers can also be considered to be quasi-equilibrated and the surface concentration of such species can be expressed using Eq. S7. The rate of dimethyl ether formation can now be expressed in terms of quantifiable values by substitution of Eq. S30 into Eq. S19:

$$r_{DME,D} = k_{elim} K_M P_{CH_2OH}[*] \tag{S31}$$

Considering methanol monomers, protonated dimers, and surface methoxy as MASI, the site balance for the dissociative pathway can be expressed as:

$$[L] = [M *] + [D *] + [Me *]$$
 (S32)

and the number of vacant sites can be solved for by substitution of Eqs. S7, S28, and S29 into Eq. S32:

$$[*] = \frac{[L]}{K_M P_{CH_3OH} + \frac{k_{ellm} K_M}{k_{DME,D} K_{MMe}} + K_D K_M P_{CH_3OH}^2}$$
(S33)

Substitution of Eq. S33 into S31 and dividing through by $\frac{k_{elim}K_M}{k_{DME,D}K_{MMe}}$, yields a new rate expression

in terms of only measurable quantities, rate constants, and equilibrium constants:

$$\frac{r_{DME,D}}{[L]} = \frac{k_{DME,D} K_{MMe} P_{CH_3OH}}{1 + \frac{k_{DME,D}}{k_{elim}} K_{MME} P_{CH_3OH} + \frac{k_{DME,D}}{k_{elim}} K_{MMe} K_D P_{CH_3OH}^2}$$
(S34)

S.3.4. Estimation of associative and dissociative first and zero-order rate constants using a generalized rate equation

Apparent first and zero-order rate constants can be predicted for both the dissociative and inhibited-associative dehydration pathways through a weighted-average of both dehydration pathways using the relative fraction of paired and isolated H⁺ sites in each CHA zeolite:

$$\frac{r}{[H^+]} = \gamma_{iso} \frac{k_A^{first} C_M}{1 + \frac{k_A^{first}}{k_A^{first}} C_M + \frac{k_D^{first}}{k_A^{first}} C_M} + \gamma_{pair} \frac{k_D^{first} C_M}{1 + \frac{k_D^{first}}{k_D^{eero}} C_M + \frac{k_D^{first}}{k_D^{inverse}} C_M^2}$$
(S35)

Here the subscript "A" refers to the associative pathway that occurs on the fraction of isolated H⁺ sites (γ_{iso}) and the subscript "D" refers to the dissociative pathway that occurs on the fraction of paired H⁺ sites (γ_{pair}).

S.3.5. Elimination of background reaction artifacts

Several tests were performed to eliminate the contributions of background reactions from measured methanol dehydration rates. Rates of dimethyl ether formation were measured at 433 K and 3.5 kPa in an empty quartz reactor (per volume), over quartz wool (per gram), and over Si-CHA (per gram; pressed and sieved to a particle diameter of 180-250 μ m and held between two quartz wool plugs) after pretreatment to 773 K (0.033 K s⁻¹) in 5% O₂/He (0.83 cm³ s⁻¹; 99.999%, Indiana Oxygen) for 4 hours. For comparison, the dimethyl ether formation rate was also measured over an H-MFI catalyst (per gram; pelleted and sieved to a particle diameter of 180-250 μ m and held between two quartz wool plugs), in order to establish a baseline for comparison of the background reaction. Dimethyl ether formation rates were calculated by assuming differential conversions and validated by an observed linear increase in the methanol conversion with increasing reactor residence time. Contributions from quartz wool were subtracted from the

reaction rate measured on Si-CHA and H-MFI. Measured rates of reaction of the blank reactor, quartz wool, Si-CHA, and H-MFI are presented in Table S11. Dimethyl ether formation rates (433 K, 3.5 kPa) in the gas-phase, on quartz wool, and on Si-CHA are more than six orders of magnitude lower than those measured on H-MFI (per gram). Thus, these background contributions were ignored when calculating rates of reaction on H-MFI and H-CHA catalysts.

Table S11. Conversions and rates of DME formation (per gram) for various control materials measured at 433 K and 3.5 kPa CH₃OH.

	CH ₃ OH Conversion / %	DME Formation Rate / mol DME (g _{cat} s) ⁻¹	DME Formation Rate / mol DME (L s) ⁻¹
Blank Quartz Reactor	3.9 x 10 ⁻³	n.m.	2.1 x 10 ⁻⁹
Quartz Wool	1.1 x 10 ⁻²	1.4 x 10 ⁻⁹	n.m.
Si-CHA	1.3 x 10 ⁻²	1.2 x 10 ⁻⁹	n.m.
H-MFI(43)	12	4.8×10^{-3}	n.m.

S.3.6. Catalyst stability and time-on-stream deactivation

Deactivation of the catalyst was monitored by measuring methanol dehydration rate return points at a set of reference conditions (2.5 kPa CH₃OH, 415 K) at the beginning and end of every new catalyst loading (Figure 5 in main text and Figures S32-S37) and no significant decrease in rate was observed as a function of time-on-stream for any of the catalysts reported here (<5% after ~5 h time-on-stream; Figure S28).

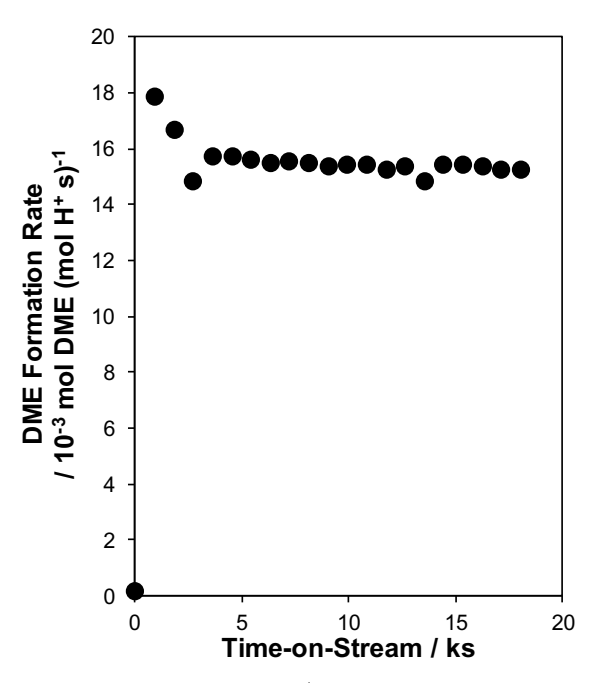


Figure S28. Methanol dehydration rates (per H⁺, 415 K) on H-CHA-OH(14,0%) zeolites as a function of time-on-stream under 2.5 kPa CH₃OH.

S.3.7. Elimination of approach to equilibrium artifacts

In addition to considering background artifacts contributing to the observed reaction rate, the proximity to the equilibrium conversion between methanol and dimethyl ether must also be considered. Thermal equilibrium occurs when the ratio of the product and reactant thermodynamic activities are related by the equilibrium constant:

$$K = \frac{a_{DME}a_{H_2O}}{a_{CH_3OH}^2} \tag{S36}$$

where the a_j terms are the thermodynamic activities of each species, j, and K is the equilibrium constant. These activities are related to the gas-phase concentrations and can be rewritten as:

$$a_j = \gamma_j RTC_j \tag{S37}$$

Here, γ_j is the activity coefficient of species j, R is the gas constant, T is the temperature, and C_j is the concentration of species j. Substituting Eq. S37 into Eq. S36, and assuming each species

behaves ideally (i.e. $\gamma_i = 1$), the equilibrium constant can now be rewritten in terms of the concentrations of each species:

$$K = \frac{c_{DME}c_{H_2O}}{c_{CH_3OH}^2} \tag{S38}$$

Each of the concentration terms can now be written in terms of conversion to yield a final expression that describes the gas-phase equilibrium for methanol and dimethyl ether:

$$K = \frac{\frac{1}{4}X_{CH_3OH}^2}{\left(1 - X_{CH_3OH}\right)^2} \tag{S39}$$

The equilibrium constant can be expressed in terms of the free energies of reaction:

$$K = e^{\frac{-\Delta G_{RXN}^0}{RT}} \tag{S40}$$

Where the free energy of reaction can be estimated from the standard free energies of formation for each species (ΔG^{o}_{i}) and the stoichiometric coefficient defined by the reaction chemistry (ν_{i}):

$$\Delta G_{RXN}^o = \sum \Delta G_j^o \frac{v_j}{v_{CH_3OH}} = \frac{1}{2} \Delta G_{DME}^o + \frac{1}{2} \Delta G_{H_2O}^o - \Delta G_{CH_3OH}^o = -9.65 \ kJ \ mol^{-1}$$
 (S41)

The equilibrium constant can now be calculated at 433 K and gives K = 14.59, which can be used to calculate an equilibrium conversion of 0.88 (433 K). The approach to equilibrium was estimated to be <0.01 at low conversions (<15%) and measured reaction rates should be uncorrupted by equilibrium.

S.3.8. Benchmarking of measured reaction kinetics on H-MFI

In order to validate the measured kinetic data, methanol dehydration rates as a function of methanol partial pressure were measured on H-ZSM(30) and H-MFI(43) and compared with reported literature data at 433 K (Figure S29). Characterization data of H-MFI catalysts can be found in Table S5. DME formation rates (per H⁺, 433 K) measured on both H-ZSM(30) and H-

MFI(43) were nearly four times larger than those reported by Jones et al. under similar methanol partial pressures (0.1-20 kPa) and temperature (433 K).¹¹

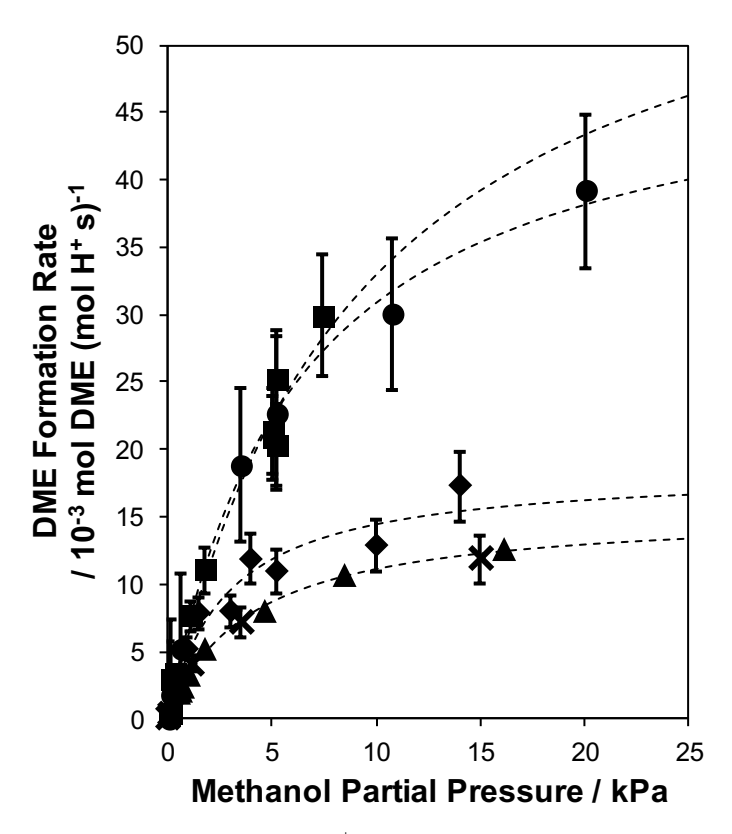


Figure S29. Methanol dehydration rates (per H⁺) on H-MFI(30) (squares) and H-MFI(43) (circles) at 433 K and on H-MFI(30) (diamonds) and H-MFI(43) (crosses) at 415 K. Triangle data points are methanol dehydration rates on H-MFI (Si/Al = 30) at 433 K reported by Jones et al. ¹¹ Dashed lines are regressions of the data to the associative pathway (Eq. S13).

In order to verify that this is not an error due to improper quantification of the number of Brønsted acid sites, *in situ* titration of H⁺ sites during steady state methanol dehydration using pyridine was performed. Pyridine was chosen as the titrant because it is able to reversibly titrate available H⁺ sites within MFI and negligibly adsorbs on Lewis acid sites under steady state methanol dehydration conditions.¹¹ Methanol dehydration rates (433 K, per gram) decreased linearly with increasing amounts of pyridine dosed to the catalyst and were completely suppressed upon contact with sufficient amounts of pyridine (Figure S30).

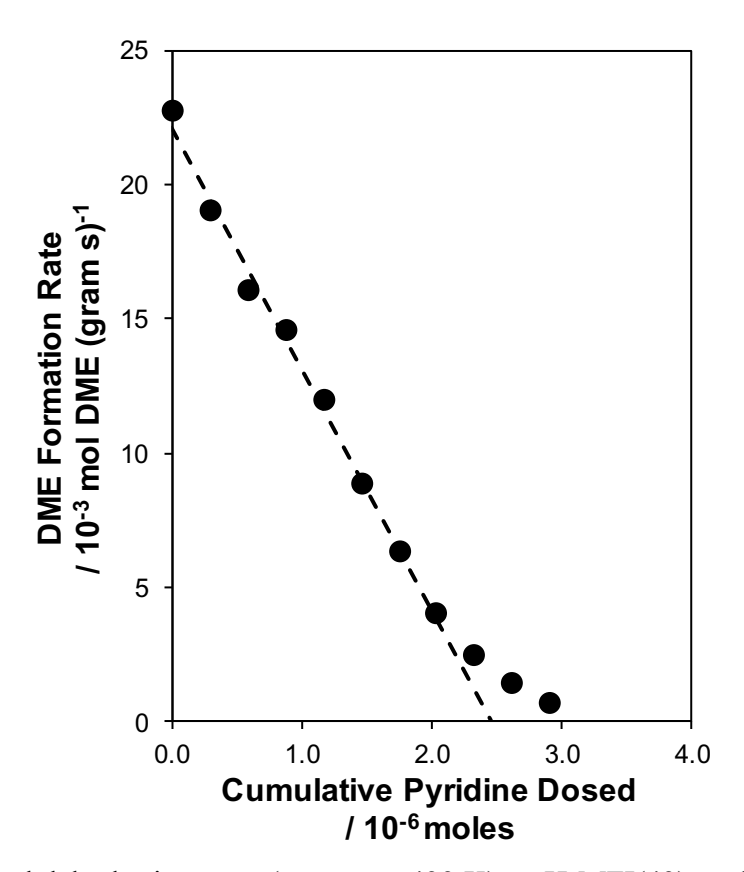


Figure S30. Methanol dehydration rates (per gram, 433 K) on H-MFI(43) zeolites as a function of cumulative moles of pyridine dosed. The dashed line is a linear regression to the data (last three points omitted).

Linear extrapolation of measured rates as a function of pyridine uptake to zero rate provides an estimate for the total number of catalytically active Brønsted acid sites and gives a H⁺/Al = 0.87, in agreement with the number of protons measured by NH₃ titration (H⁺/Al = 0.85 from NH₃ TPD). Rates of DME formation (433 K) were fully recovered after treatment to 773 K (0.033 K s⁻¹) in 5% O₂/He (0.83 cm³ s⁻¹; 99.999%, Indiana Oxygen) for 4 hours, indicating that pyridine exclusively coordinates to H⁺ sites and that no structural changes occurred, leading to the observed decrease in the dehydration rate. These results indicate that the *ex situ* NH₃ titrations are capable of quantifying H⁺ sites relevant for methanol dehydration chemistry in MFI zeolites and represent an accurate count of the number of active sites. Despite the confirmation that DME formation rates

are properly normalized, the discrepancy between the measured and reported methanol dehydration rates persisted.

DME formation rates (per H⁺ from pyridine) were next measured as a function of temperature at various methanol pressures (0.1-20 kPa) until measured rates agreed with reported values from Jones et al.¹¹ Both first and zero-order rate constants (per H⁺ site from pyridine) on H-MFI(30) and H-MFI(43) were reproduced within 15% of the values reported by Jones et al.¹¹ at a temperature of 415 K (Figure S29). Additionally, activation parameters (405-433 K) in both the first and zero-order kinetic regimes agreed within 20% of those reported for methanol dehydration on MFI zeolites (Figure S31, Table S12), further indicating that first and zero order rate constants are being compared under the same catalytic conditions and that the difference in measured rates at 433 K is not due to a difference in surface coverages or apparent kinetic regimes. As both the first and zero-order rate constants (per H⁺ from pyridine) and apparent activation parameters were in agreement with those reported for MFI zeolites, the temperature of 415 K was chosen for all catalysts studied and the source of the discrepancy was not further investigated.

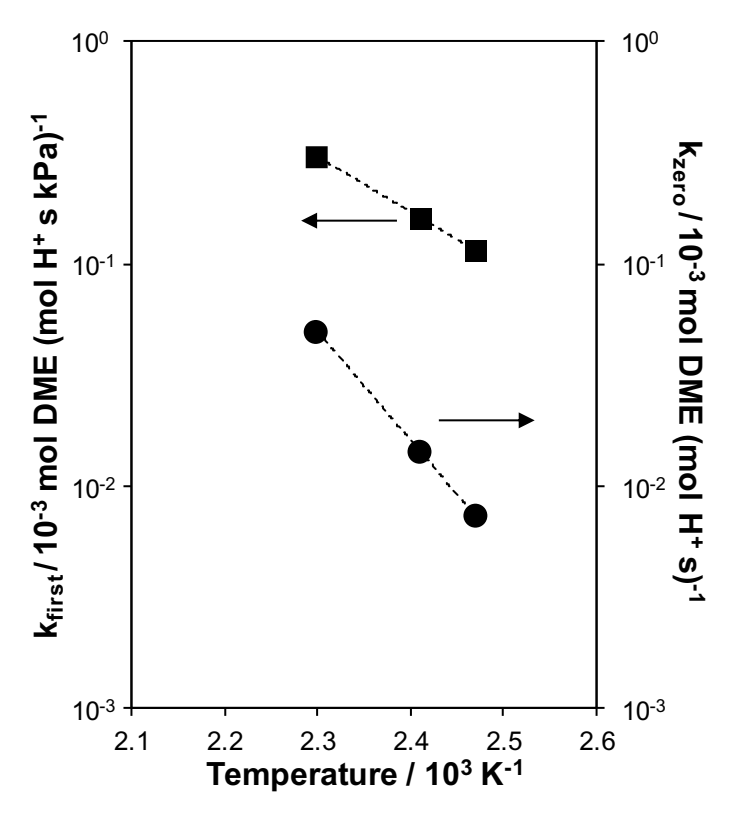


Figure S31. Associative rate first (squares) and zero (circles) order rate constants (per H⁺) on H-MFI(43) measured as a function of temperature (405-433 K).

Table S12. Activation parameters for associative rate first and zero order rate constants (per H^+) on H-MFI(43) and an H-MFI (Si/Al = 30) reported by Jones et al.¹⁰

Zeolite Sample	ΔH _{zero} / kJ mol ⁻¹	ΔH _{first} / kJ mol ⁻¹	ΔS_{zero} / J mol ⁻¹ K ⁻¹	ΔS_{first} / J mol $^{-1}$ K $^{-1}$	$\Delta G_{ m zero}$ / kJ mol $^{-1}$	ΔG _{first} / kJ mol ⁻¹
H-MFI $Si/Al = 43$	93±5	48±5	-58±7	-149±8	119±10	112±10
$H-MFI$ $Si/Al = 30^{a}$	90±2	42±2	-75±2	-160±10	123±3	111±9

^aActivation parameters reported by Jones et al. ¹⁰

S.3.9. DME formation rates (415 K) measured as a function of CH₃OH pressure

Rates of methanol dehydration (415 K, per H⁺) measured as a function of methanol partial pressure (0.05-50 kPa) are shown in Figure 5 of the main text for H-CHA-OH(14,0%), H-CHA-OH(15,18%), H-CHA-OH(16,24%), H-CHA-OH(17,30%), and H-CHA-OH(14,44%) zeolites. Figures S32-S38 show methanol dehydration rates (per H⁺, 415 K) as a function of methanol partial pressure for H-CHA-OH(16,0%), H-CHA-OH(26,0%), H-CHA-F(17,0%), H-CHA-OH(16,6%), H-MFI(17), H-MFI(30), and H-MFI(43), respectively.

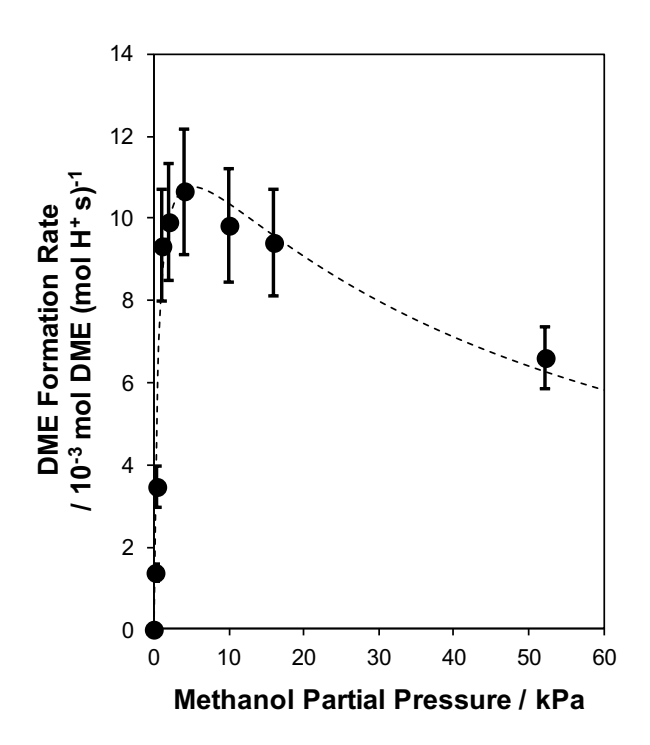


Figure S32. Methanol dehydration rates (per H⁺, 415 K) on H-CHA-OH(16,0%) as a function of methanol partial pressure. Dashed line is a regression to the generalized rate expression (Eq. S35).

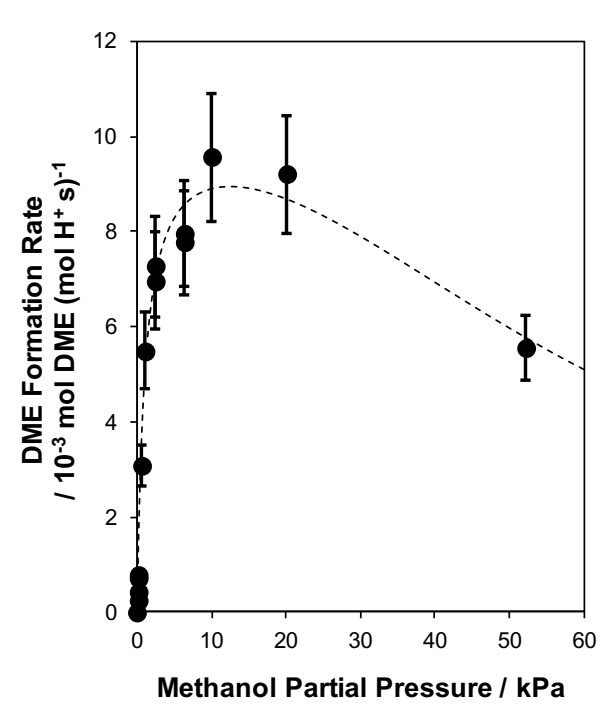


Figure S33. Methanol dehydration rates (per H⁺, 415 K) on H-CHA-OH(26,0%) as a function of methanol partial pressure. Dashed line is a regression to the generalized rate expression (Eq. S35).

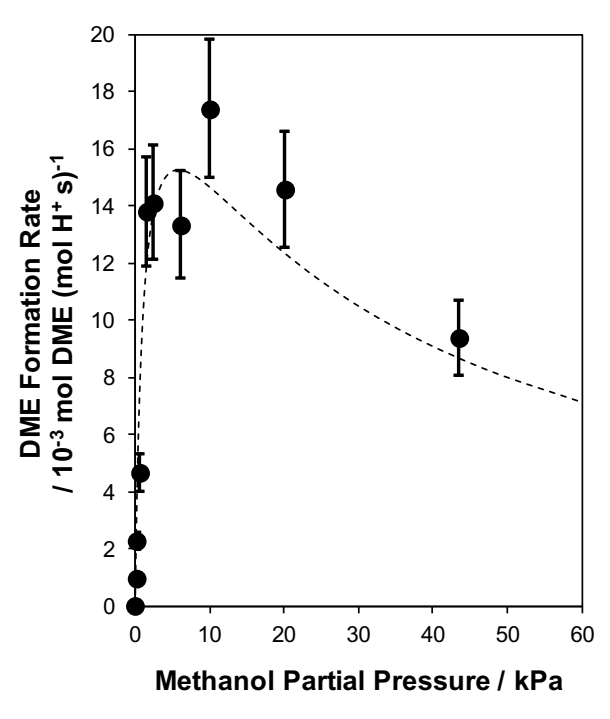


Figure S34. Methanol dehydration rates (per H⁺, 415 K) on H-CHA-F(17,0%) as a function of methanol partial pressure. Dashed line is a regression to the generalized rate expression (Eq. S35).

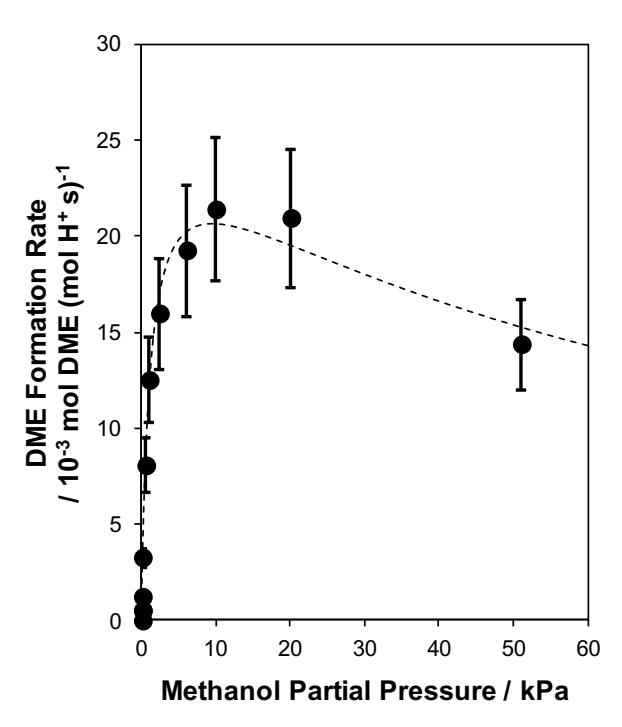


Figure S35. Methanol dehydration rates (per H⁺, 415 K) on H-CHA-OH(16,6%) as a function of methanol partial pressure. Dashed line is a regression to the generalized rate expression (Eq. S35).

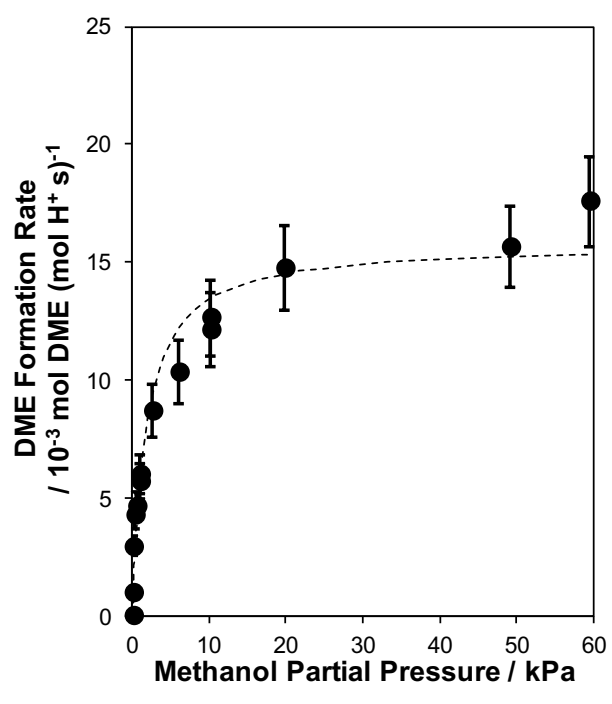


Figure S36. Methanol dehydration rates (per H⁺, 415 K) on H-MFI(17) as a function of methanol partial pressure. Dashed line is a regression to the associative rate expression (Eq. S13).

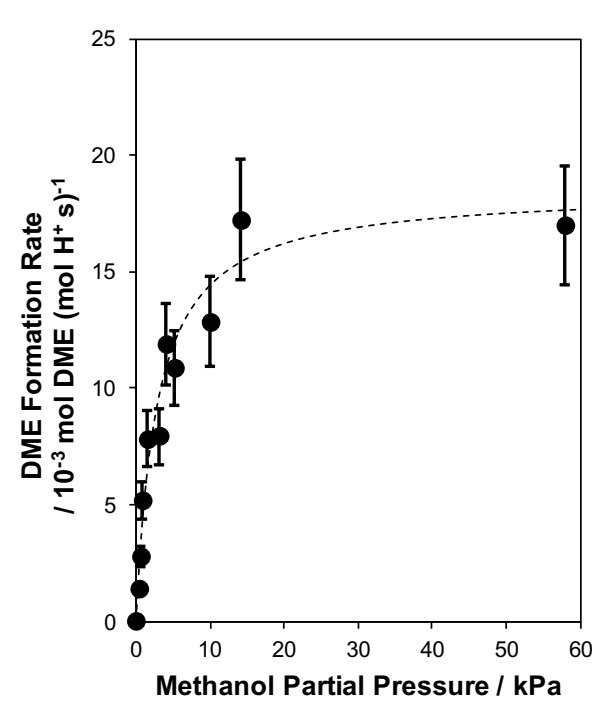


Figure S37. Methanol dehydration rates (per H⁺, 415 K) on H-MFI(30) as a function of methanol partial pressure. Dashed line is a regression to the associative rate expression (Eq. S13).

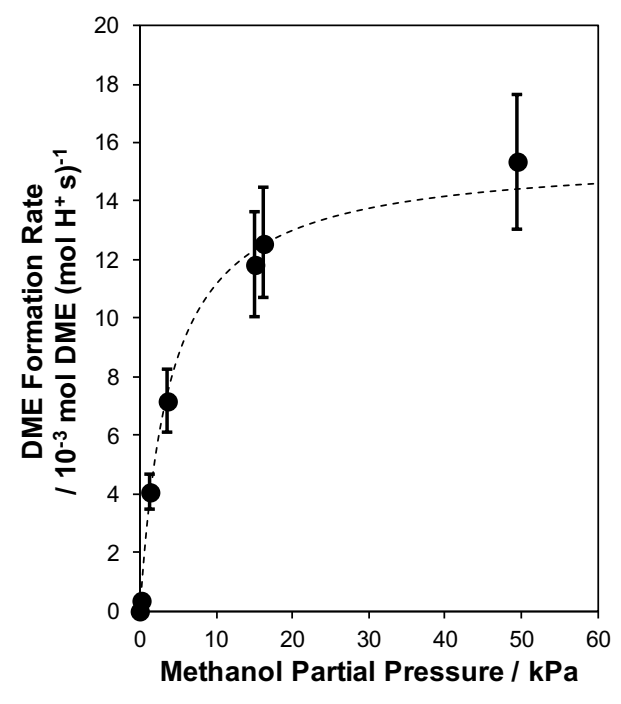


Figure S38. Methanol dehydration rates (per H⁺, 415 K) on H-MFI(43) as a function of methanol partial pressure. Dashed line is a regression to the associative rate expression (Eq. S13).

Regression of reported associative first-order rate constants (433 K, per H⁺), measured on a wide range of zeolites with varying pore size (0.5-1.2 nm free sphere diameter), ¹² allows for the estimation of first-order rate constants as a function of pore diameter and suggests that dehydration intermediates in CHA zeolites are confined in voids of size similar to that of the 6-MR and 8-MR apertures of the CHA framework (Figure S39).

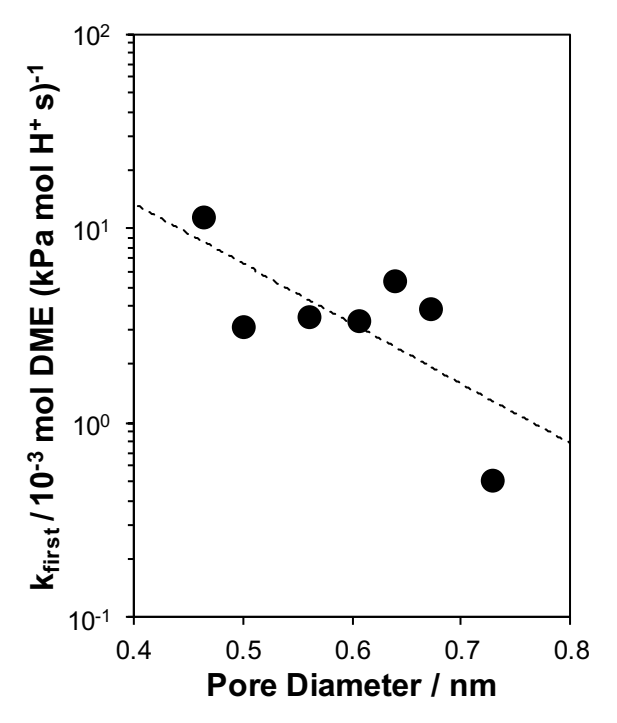


Figure S39. Associative first order rate constants (per H⁺, 433 K) as a function of pore diameter in MFI, MTT, MTW, MOR, SFH, BEA, and FAU zeolites. Dashed line is an exponential regression to the data. All data is reproduced from Jones et al.¹²

S.3.10. Estimation of dehydration rate constants on isolated and paired protons in CHA zeolites

Extraframework Al species, observed here on CHA zeolites containing ≥30% of Al in paired sites (²⁷Al NMR spectra in Section S.2, SI), do not contribute significantly to measured rates of methanol dehydration^{11,13} and the presence of extra-lattice Al moieties, which have been shown to artificially decrease the void diameter surrounding reactive intermediates, ¹³ is not responsible for the observed increase in both first and zero-order rate constants, because only firstorder dehydration rate constants are sensitive to changes in void diameter. ¹² Additionally, CHA-OH(15,18%) zeolites show first and zero-order rate constants larger than those measured on isolated protons in CHA, despite minimal amounts of extraframework Al (Figure S24), further indicating that extraframework Al species do not contribute to the observed increase in apparent rate constants as a function of the fraction of Al atoms in pairs. Using the generalized dehydration rate expression (Eq. S.35), the observed first and zero order rate constants (415 K, per H⁺) can be expressed as a function of the fraction of paired Al in each CHA catalyst. Extrapolation of the observed first and zero order rate constants to the limit of Al isolation (0% paired Al) allows for estimation of methanol dehydration rate constants for the associative pathway on isolated H⁺ sites. Additionally, extrapolation to the limit of complete pairing (100% paired Al) rate constants for the dissociative pathway on paired protons can be estimated and are nearly an order of magnitude larger than the associative rate constants (Figure 6 in main text).

Section S.4. IR spectra under steady methanol dehydration

S.4.1. Measurement of in situ IR spectra on CHA and MFI zeolites

IR spectra recorded on H-CHA-OH(14,0%), H-CHA-OH(14,44%), and H-MFI(43) under various methanol pressures (0.15-22 kPa) are shown in Figures S40-S42.

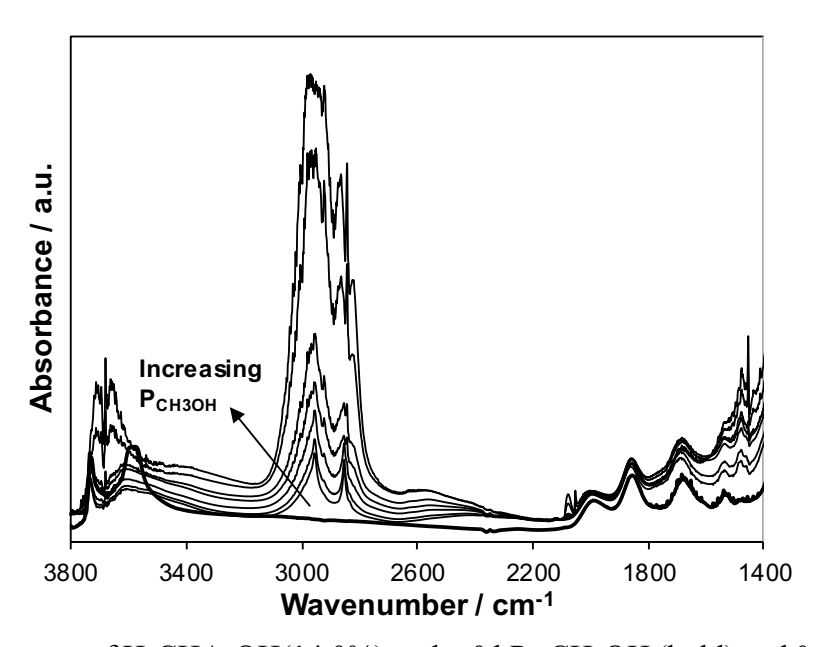


Figure S40. IR spectra of H-CHA-OH(14,0%) under 0 kPa CH₃OH (bold) and 0.15, 0.77, 1.5, 3.0, 5.9, 13.5, and 22 kPa CH₃OH (thin) at 415 K.

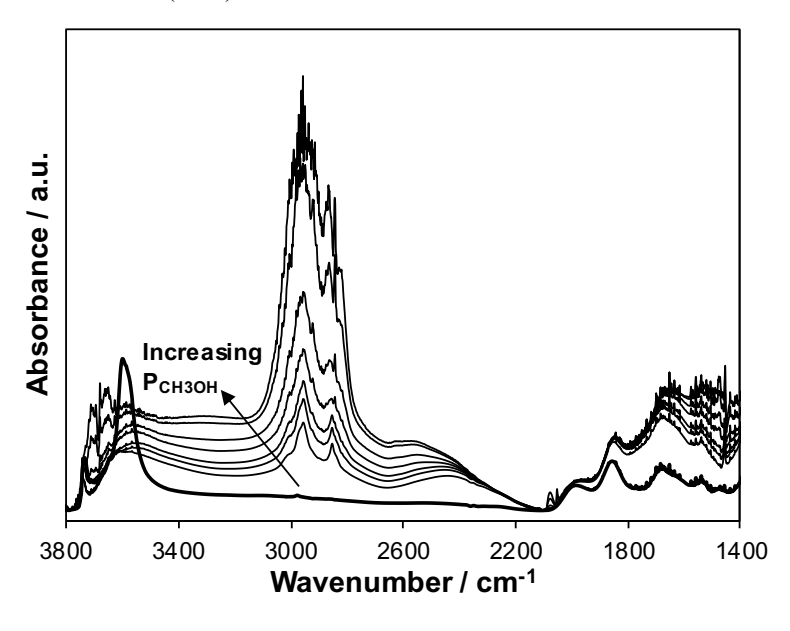


Figure S41. IR spectra of H-CHA-OH(14,44%) under 0 kPa CH_3OH (bold) and 0.15, 0.77, 1.5, 3.0, 5.9, 13.5, and 22 kPa CH_3OH (thin) at 415 K.

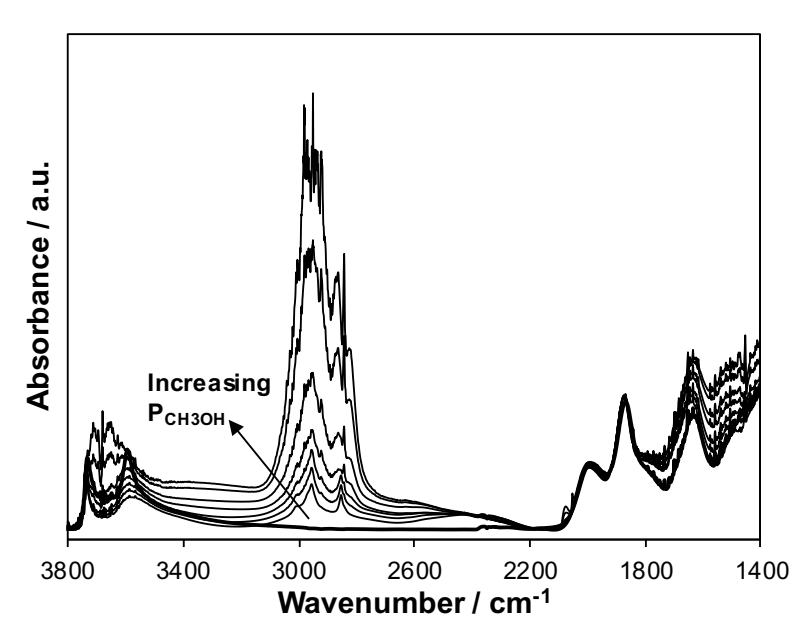


Figure S42. IR spectra of H-MFI(43) under 0 kPa CH₃OH (bold) and 0.15, 0.77, 1.5, 3.0, 5.9, 13.5, and 22 kPa CH₃OH (thin) at 415 K.

In order to establish an experimental reference for surface methoxy deformation modes, H-CHA-OH(14,0%), which was chosen because it contains a single type of active site (i.e., only isolated protons), was equilibrated under steady-state methanol pressure (0.15 kPa) and then purged in dry He (13.3 cm³ s⁻¹ g⁻¹) for 30 minutes at 523 K until the spectra remained constant. Similar procedures have been used to isolated surface methoxy species observed during IR, ^{10,14,15} ¹³C NMR, ¹⁶ and neutron scattering ¹⁷ spectroscopic studies of methanol-to-olefins chemistry.

Section S.5. Evaluation of mass transfer in CHA zeolites

S.5.1. Space velocity test to verify differential operation

Differential operation was confirmed by measuring the rate of methanol dehydration (per H⁺, 415 K) as a function of inverse space velocity (i.e. residence time) at fixed methanol partial pressures on each MFI and CHA zeolite prior to kinetic analysis. Figure S43 shows a typical space velocity test performed at 1 kPa CH₃OH. On all catalysts tested, the CH₃OH conversion increased linearly with increasing residence time and DME formation rates (per H⁺, 415 K) were invariant with residence time at fixed CH₃OH partial pressure. These results confirm that each catalyst is operating under differential conditions and rates are independent of reactor hydrodynamics.

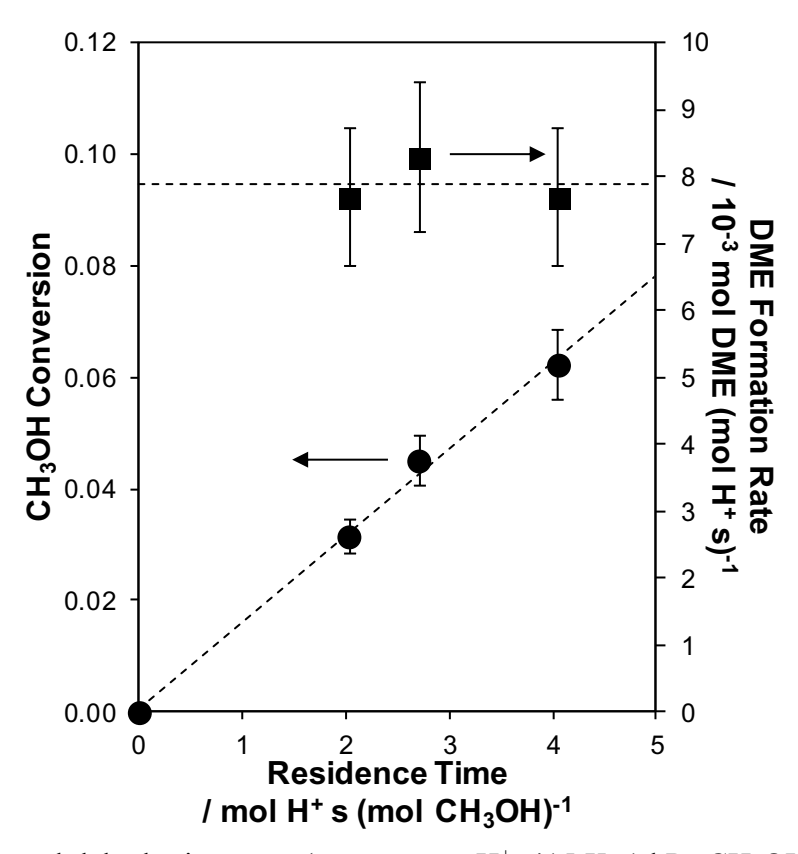


Figure S43. Methanol dehydration rates (squares; per H⁺, 415 K, 1 kPa CH₃OH) and conversion (circles) on H-CHA-OH(14,0%) as a function of residence time. Dashed lines represent a linear regression to conversion data and the average rate of DME formation.

S.5.2. Derivation of concentration gradients in spherical catalyst particles for coupled reaction and internal diffusion

When rates of internal mass transport become similar to or less than the rate of reaction, severe concentration gradients will exist within porous catalysts resulting in an inhomogeneous reaction rate and, in the process, corrupting measurements of reaction kinetics. The severity of these internal concentration gradients can be predicted through models of coupled reaction and transport phenomena and used to assess internal mass transport restrictions. For steady state reaction and diffusion within a spherical catalyst particle that is free of external mass transfer limitations (Section S.5.1), the differential equation that describes the concentration of methanol as a function of particle radius is

$$\frac{d^2C_M}{dr^2} + \frac{2}{r}\frac{dC_M}{dr} - \frac{2\rho_S}{D_e}r'_{DME} = 0$$
 (S42)

Here, C_M is the concentration of methanol (mol m⁻³), r is the distance from the center of the pellet (m), ρ_s is the proton density per volume (mol H⁺ m⁻³), \mathcal{D}_e is the effective self-diffusivity of methanol inside the pore (m² s⁻¹), and r'_{DME} is the rate of DME formation (mol DME (mol H⁺ s)⁻¹). The factor of 2 accounts for the difference in stoichiometry between the product DME and methanol reactant ($r_M = -2*r_{DME}$). The self-diffusivity of methanol within CHA was estimated from reported molecular dynamics simulations of methanol diffusion within DDR zeolites (\mathcal{D}_e (360 K) = 7.5 x 10⁻¹¹ m² s⁻¹), ¹⁸ which is similar to CHA in both limiting pore diameter (8-MR, 0.37 nm) and pore connectivity (window-cage structure), and extrapolated to the relevant reaction temperature (\mathcal{D}_e (415 K) = 9.3 x 10⁻¹¹ m² s⁻¹) using Chapman-Enskog theory:

$$\mathcal{D}_{e}(T_{2}) = \mathcal{D}_{e}(T_{1}) * \left(\frac{T_{2}}{T_{1}}\right)^{\frac{3}{2}}$$
 (S43)

The rate of DME formation (per H⁺) can be expressed using the generalized rate expression (Eq. S35) that weights the contribution from both the associative and dissociative pathways as a function of the relative population of isolated and paired Al sites, respectively and allows for Eq. S42 to be rewritten as:

$$\frac{d^2C_M}{dr^2} + \frac{2}{r}\frac{dC_M}{dr} - \frac{2\rho_s}{D_e} \left[\gamma_{iso} \frac{k_{first,A}C_M}{1 + \frac{k_{first,A}}{k_{zero,A}} C_M + \frac{k_{first,A}}{k_{inverse,A}} C_M^2}}{1 + \frac{k_{first,D}C_M}{k_{inverse,D}} C_M + \frac{k_{first,D}C_M}{k_{inverse,D}} C_M^2} \right] = 0$$
 (S44)

Figures S44-S52 show concentration profiles as a function of particle radius and concentration at 415 K for each CHA zeolite studied here. Bulk-phase methanol concentrations were chosen to be similar to those used during methanol dehydration catalysis (0.05-52 kPa CH₃OH). It is apparent that the low-aluminum CHA catalyst containing only isolated H⁺ sites (Si/Al = 30) exhibits severe concentration gradients in the first-order kinetic regime (<1 kPa), in agreement with lower observed rates of DME formation (415 K, per H⁺) than on CHA with all isolated Al sites at higher Al content (Si/Al = 15). These results are also in agreement with the measured crystallite size, which increases nearly four-fold from a particle diameter of 1.5 μ m (Si/Al = 15) to 6 μ m (Si/Al = 30). All other CHA zeolites examined at Si/Al = 15 (0-44% paired Al) contain crystallite sizes smaller than 1.5 μ m and show minimal internal concentration gradients despite rates of reaction that increased systematically with the fraction of paired Al (Figure 5 in main text).

There was, however, a general decrease in the crystallite size as a function of paired Al content and to eliminate this as a possible contributor to the increase in observed DME formation rates (415 K, per H⁺), a nano-sized CHA zeolite was synthesized using TMAda⁺ cations and the surfactant hexadecyl-trimethylammonium bromide (CTAB) in the absence of Na⁺. SEM micrographs show that the nano-sized CHA zeolite contains crystallites about 800 nm in diameter (Figure S21) and Co²⁺ titrations show that these zeolites contain a small fraction of paired Al sites

(Co/Al = 0.03), introduced by including an additional quaternary amine (i.e. CTAB). Methanol dehydration rates (415 K, per H⁺) on nano-sized CHA follow the same trend as seen for CHA zeolites prepared through conventional synthesis protocols, where both the first and zero order rate constants increase as a function of paired Al content (Figure 6 in main text; Tables S2-S4). Predicted internal concentration gradients are also negligible on nano-sized CHA (Figure S48), in line with previous observations that CHA zeolite with crystallite sizes $<2 \mu m$ are free of internal concentration gradients. These results further demonstrate that the increase in DME formation rate (per H⁺) across CHA zeolites containing different amounts of paired Al (Si/Al = 15) is solely a function of the number of paired Al sites and not a crystal size effect.

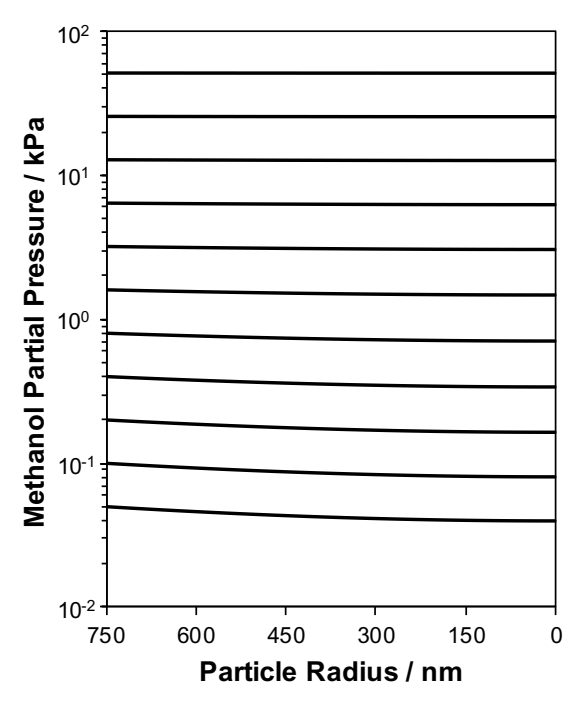


Figure S44. Methanol partial pressures in H-CHA-OH(14,0%) as a function of particle radius, where zero is the crystal center, for bulk CH₃OH pressures of 0.05, 0.1, 0.2, 0.4, 0.8, 1.6, 3.2, 6.4, 12.8, 25.6, and 51.2 kPa at 415 K.

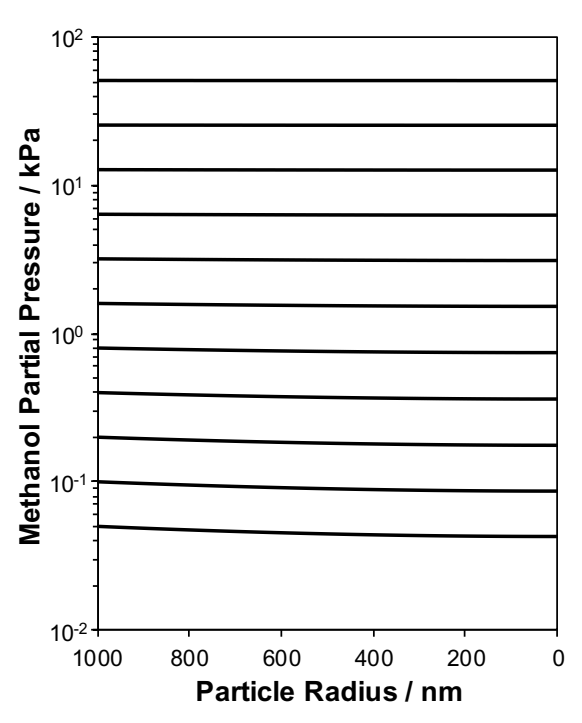


Figure S45. Methanol partial pressure in H-CHA-OH(17,0%) as a function of particle radius, where zero is the crystal center, for bulk CH₃OH pressures of 0.05, 0.1, 0.2, 0.4, 0.8, 1.6, 3.2, 6.4, 12.8, 25.6, and 51.2 kPa at 415 K.

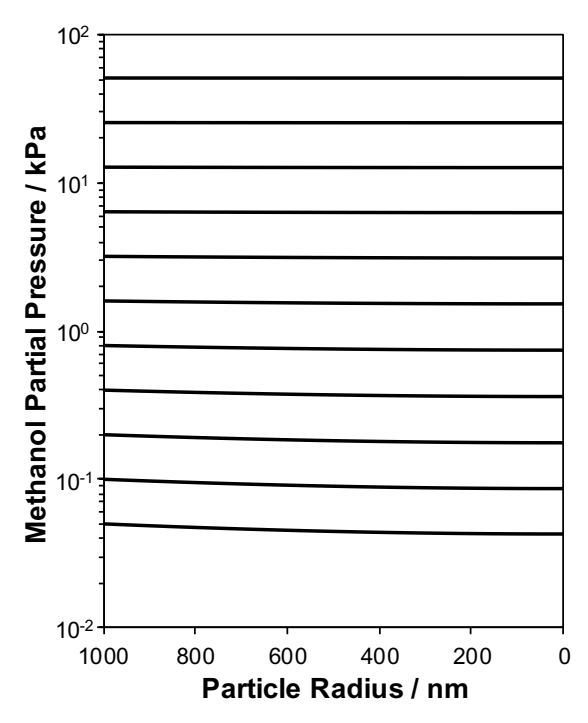


Figure S46. Methanol partial pressure in H-CHA-F(18,0%) as a function of particle radius, where zero is the crystal center, for bulk CH₃OH pressures of 0.05, 0.1, 0.2, 0.4, 0.8, 1.6, 3.2, 6.4, 12.8, 25.6, and 51.2 kPa at 415 K.

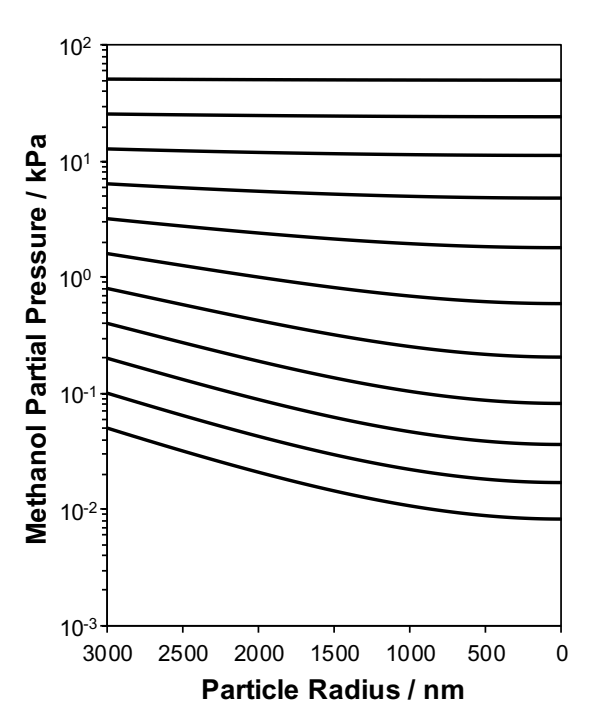


Figure S47. Methanol partial pressure in H-CHA-OH(27,0%) as a function of particle radius, where zero is the crystal center, for bulk CH₃OH pressures of 0.05, 0.1, 0.2, 0.4, 0.8, 1.6, 3.2, 6.4, 12.8, 25.6, and 51.2 kPa at 415 K.

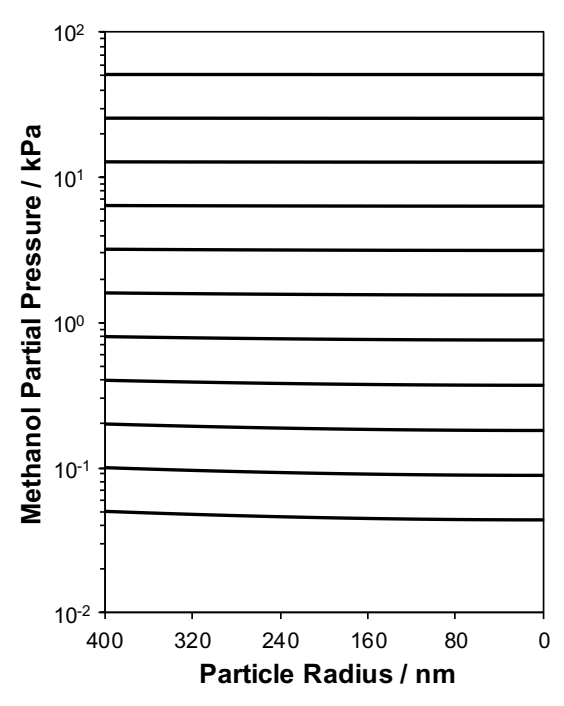


Figure S48. Methanol partial pressure in H-CHA-OH(16,6%) as a function of particle radius, where zero is the crystal center, for bulk CH₃OH pressures of 0.05, 0.1, 0.2, 0.4, 0.8, 1.6, 3.2, 6.4, 12.8, 25.6, and 51.2 kPa at 415 K.

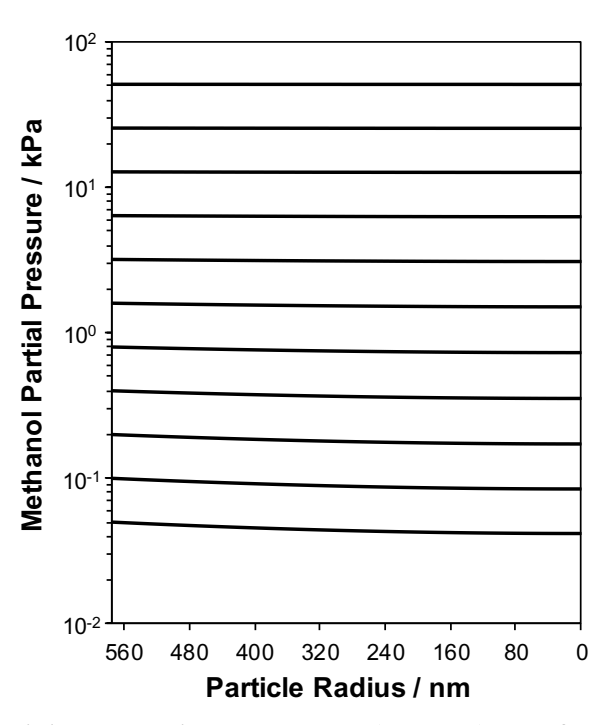


Figure S49. Methanol partial pressure in H-CHA-OH(15,18%) as a function of particle radius, where zero is the crystal center, for bulk CH₃OH pressures of 0.05, 0.1, 0.2, 0.4, 0.8, 1.6, 3.2, 6.4, 12.8, 25.6, and 51.2 kPa at 415 K.

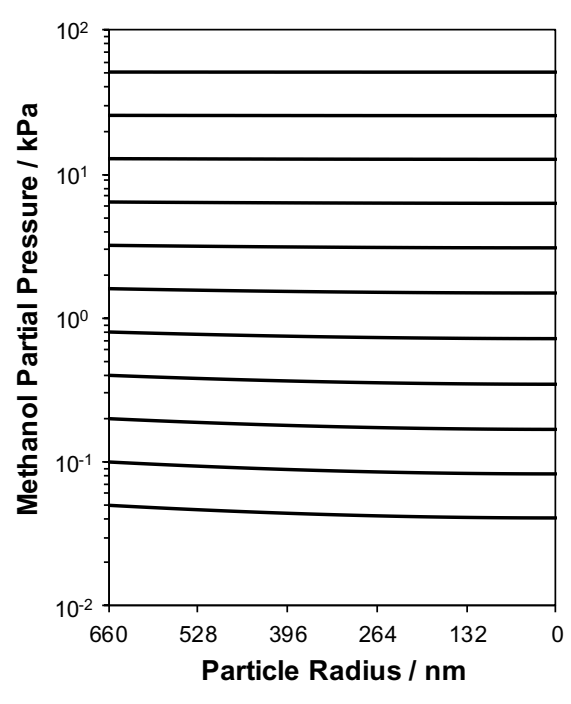


Figure S50. Methanol partial pressure in H-CHA-OH(16,24%) as a function of particle radius, where zero is the crystal center, for bulk CH₃OH pressures of 0.05, 0.1, 0.2, 0.4, 0.8, 1.6, 3.2, 6.4, 12.8, 25.6, and 51.2 kPa at 415 K.

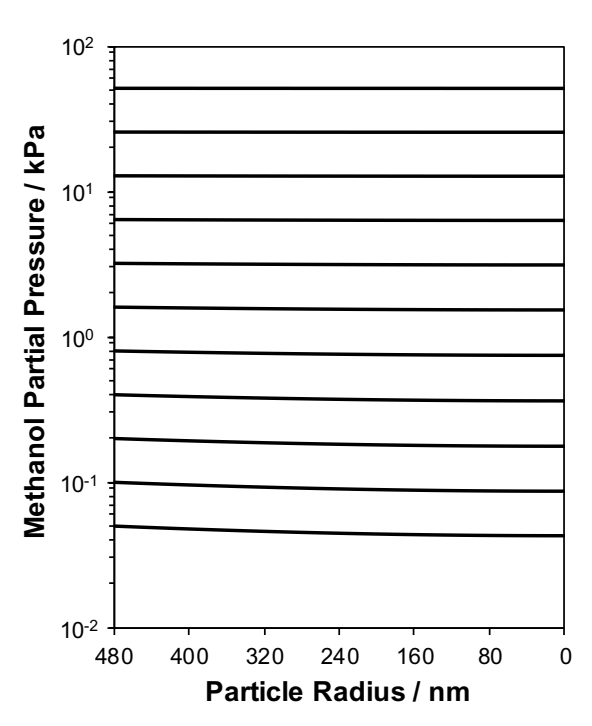


Figure S51. Methanol partial pressure in H-CHA-OH(17,30%) as a function of particle radius, where zero is the crystal center, for bulk CH₃OH pressures of 0.05, 0.1, 0.2, 0.4, 0.8, 1.6, 3.2, 6.4, 12.8, 25.6, and 51.2 kPa at 415 K.

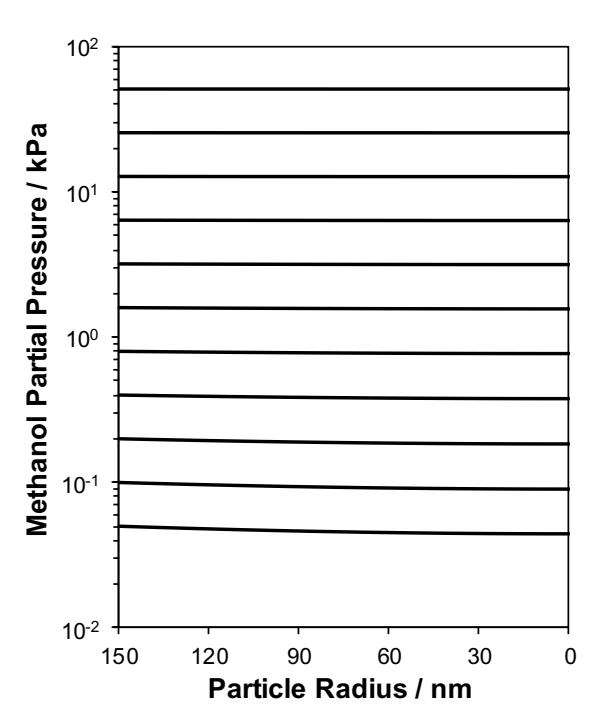


Figure S52. Methanol partial pressure in H-CHA-OH(14,44%) as a function of particle radius, where zero is the crystal center, for bulk CH₃OH pressures of 0.05, 0.1, 0.2, 0.4, 0.8, 1.6, 3.2, 6.4, 12.8, 25.6, and 51.2 kPa at 415 K.

S.5.3. Derivation of first and zero order effectiveness factors

A more quantitative evaluation of internal mass transfer can be evaluated by calculating the internal effectiveness factor as a function of the Thiele modulus for each CHA catalyst. For evaluation of the Thiele modulus, distinct first and zero order reaction rate laws were defined:

$$r'_{first} = (\gamma_{iso}k_A^{first} + \gamma_{pair}k_D^{first})C_M$$
 (S45)

$$r'_{zero} = \gamma_{iso} k_A^{zero} + \gamma_{pair} k_D^{zero}$$
 (S46)

The rate of reaction for each kinetic regime will be evaluated using a generalize rate expression (Eq. S35) that accounts for contributions from both relevant kinetic pathways that occur uniquely at isolated (e.g. associative) and paired protons (e.g. dissociative). Additionally, all sites are assumed to be saturated with kinetically-relevant intermediates in the zero-order regime.

Eq. S42 can be non-dimensionalized by normalizing by the bulk fluid concentration (C_B) and the particle radius (r_p) to yield:

$$\frac{d^2\Psi}{d\lambda^2} + \frac{2}{\lambda} \frac{d\Psi}{d\lambda} - \frac{2\rho_S r_p^2}{C_B \mathcal{D}_e} r'_{DME} = 0$$
 (S47)

where,

$$\Psi = \frac{c_m(r)}{c_B} \tag{S48}$$

$$\lambda = \frac{r}{r_p} \tag{S.49}$$

The different DME formation rates specific to each unique kinetic regime can further be rewritten using the non-dimensional concentration (Ψ) to give:

$$r'_{first} = (\gamma_{iso}k_A^{first} + \gamma_{pair}k_D^{first})\Psi C_B$$
 (S50)

$$r'_{zero} = \gamma_{iso} k_A^{zero} + \gamma_{pair} k_D^{zero}$$
 (S51)

Substitution of these rates into Eq. S47 yield the following differential equations that describe the concentration profile for each kinetic regime:

$$\frac{d^2\Psi}{d\lambda^2} + \frac{2}{\lambda} \frac{d\Psi}{d\lambda} - \frac{2\rho_s r_p^2 (\gamma_{iso} k_A^{first} + \gamma_{pair} k_D^{first})}{\mathcal{D}_e} \Psi = 0$$
 (S52)

$$\frac{d^2\Psi}{d\lambda^2} + \frac{2}{\lambda} \frac{d\Psi}{d\lambda} - \frac{2\rho_s r_p^2 (\gamma_{iso} k_A^{zero} + \gamma_{pair} k_D^{zero})}{C_B \mathcal{D}_e} = 0$$
 (S53)

A distinct Thiele Modulus (ϕ_i) can then be defined for each regime by the ratio of constants in the last term on the left-hand side as follows:

$$\phi_{first}^2 = \frac{2\rho_s r_p^2 (\gamma_{iso} k_A^{first} + \gamma_{pair} k_D^{first})}{\mathcal{D}_e}$$
 (S54)

$$\phi_{zero}^2 = \frac{2\rho_s r_p^2 (\gamma_{iso} k_A^{zero} + \gamma_{pair} k_D^{zero})}{c_B \mathcal{D}_e}$$
 (S55)

Thiele moduli were estimated from the ratio of the reaction rate, evaluated independently for each sample using either experimentally measured first-order rate constants, or those calculated from the correlation between the apparent first-order rate constant as a function of the fraction of Al in pairs (Figure 6 in main text), to diffusion rate evaluated at the gas-phase concentration. The effectiveness factor can then be expressed as the ratio of the observed reaction rate to the theoretical reaction rate evaluated at the bulk concentration:

$$\eta = \frac{r'_{DME}(c_m(r))}{r'_{DME}(c_B)}$$
 (S56)

Effectiveness factors were calculated from the ratio of the observed reaction rate, using apparent first-order rate constants, to the theoretical reaction rate evaluated at the gas-phase concentration, using first-order rate constants extracted from Figure 6 in the main text.

Equations S52 and S53 can be solved analytically for the concentration profile inside the catalyst pellet and substituted into Eqs. S50 and S51 to derive an expression for the actual rate of reaction as a function of particle radius for each unique kinetic regime. The effectiveness factor can then be evaluated as a function of the Thiele modulus for the first and zero order kinetic regimes:

$$\eta = \frac{3}{\phi_{first}^2} \left(\phi_{first} \coth(\phi_{first}) - 1 \right) \tag{S57}$$

$$\eta = 1 \tag{S58}$$

Figure 3 in main text shows the effectiveness factor for a first order reaction as a function of the Thiele modulus.

Section S.6. Origin of kinetic inhibition in CHA zeolites

Unlike MFI, and other medium and large pore zeolites, CHA zeolites, across all composition and paired Al site concentrations, exhibit increasing inhibition of DME formation rates as methanol partial pressures increase >10 kPa (415 K, per H⁺; Figure 5 in main text; Figures S32-S35). One potential source of the observed inhibition at high methanol pressures may be due to diffusion limitations of DME leaving the zeolite pores after desorption from the catalyst surface. Diffusion coefficients for DME were conservatively estimated as being one order of magnitude smaller than CH₃OH diffusion coefficients in CHA zeolites (e.g. DME: $\mathcal{D}_e(T=415 \text{ K})=7.5 \text{ x}$ 10^{-12} m² s⁻¹). Experimentally measured DME self-diffusion coefficients ($\mathcal{D}_e(T = 293 \text{ K}) = 1.2 \text{ x}$ 10⁻⁹ m² s⁻¹)²⁰ in MFI zeolites are only twice as large as methanol self-diffusion coefficients in MFI derived from molecular dynamic simulations ($\mathcal{D}_{e}(T = 300 \text{ K}) = 2.5 \times 10^{-9} \text{ m}^2 \text{ s}^{-1}$), ¹⁸ suggesting that the estimate provided here for CHA zeolites is reasonable and a conservative estimate for the CHA framework. The ratio of the rate of DME formation (mol DME per unit time) and the transport rate of DME through the catalyst (mol DME per unit time) can be evaluated as a function of the internal concentration profile (Section S.5.2) using Weisz-Prater criteria²¹ to give an order of magnitude estimate for the presence of product diffusion and is expressed by:

$$\chi < \frac{r'_{DME}\rho_s\rho_B r_p^2}{\mathcal{D}_e C_M} \tag{S59}$$

Here, r'_{DME} is the rate of DME formation per H^+ site (415 K), ρ_s is the density of H^+ sites per gram, ρ_B is the bulk zeolite density (estimated to be 2.2 g cm⁻³), r_p is the particle radius, D_e is the effective diffusivity of DME, and C_M is the gas-phase concentration of methanol. At all points within each CHA zeolite, the value of χ is $<10^{-2}$ indicating that the rate of DME formation is much slower than the rate at which DME is transported out of the catalyst and that product diffusion is not responsible for the observed inhibition of DME formation rates at high methanol pressures.

Alternatively, the presence of water formed through the dehydration process may be responsible for the inhibition at high methanol pressures, as water is known to inhibit alcohol dehydration reactions on solid acid catalysts.²² The dependence of methanol dehydration rates in CHA zeolites on water partial pressure was investigated by co-feeding water during steady state catalysis (415 K) at various water to methanol ratios ($P_{H2O}/P_{CH3OH} = 0.02-3.6$) and methanol pressures (0.05-50 kPa CH₃OH) on H-CHA-OH(14,0%) and H-CHA-OH(14,44%) catalysts and are shown in Figures S53 and S54, respectively.

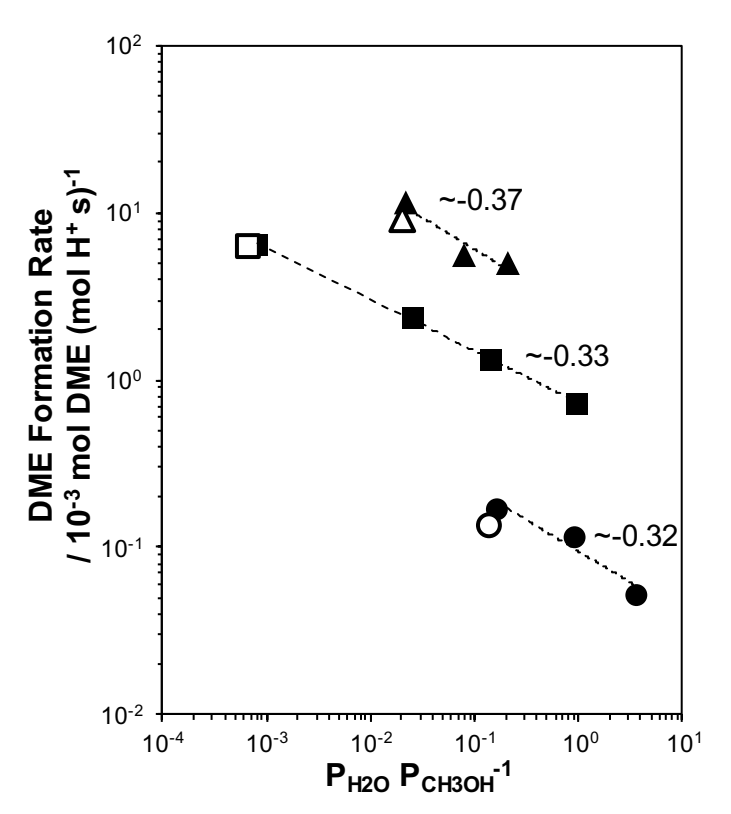


Figure S53. Methanol dehydration rates (per H⁺, 415 K) on H-CHA-OH(14,0%) as a function of water pressure at 0.05 (circles), 2.5 (triangle), and 50 (squares) kPa CH₃OH. Open points from steady state rates (415 K), without co-feeding H₂O, and water pressures are from product formation. Labels indicate the water order under each set of conditions. Dashed lines are power law regressions to the data.

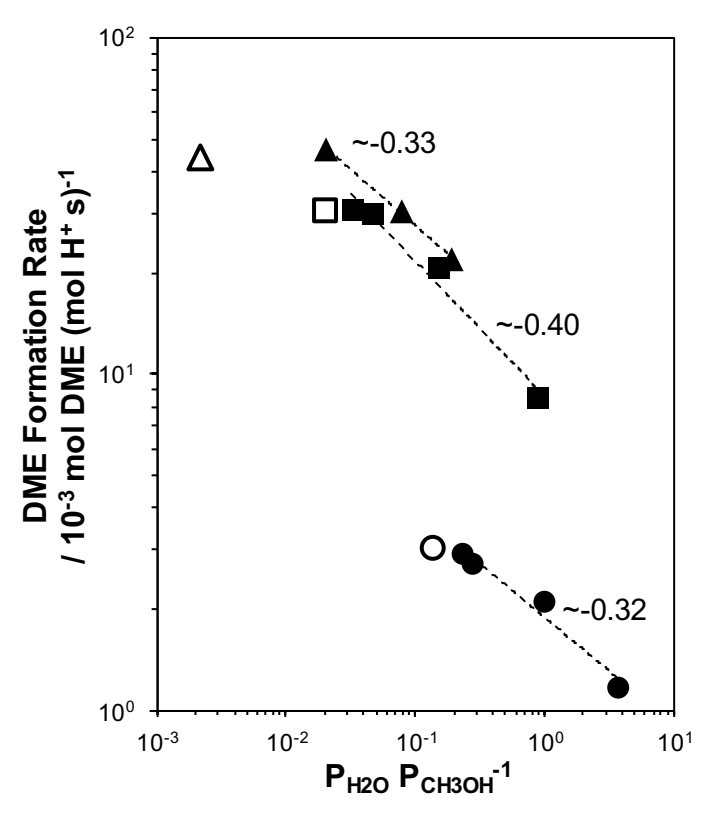


Figure S54. Methanol dehydration rates (per H⁺, 415 K) on H-CHA-OH(14,44%) as a function of water pressure at 0.05 (circles), 2.5 (triangle), and 50 (squares) kPa CH₃OH. Open points from steady state rates (415 K), without co-feeding H₂O, and water pressures are from product formation. Labels indicate the water order under each set of conditions. Dashed lines are power law regressions to the data.

Figures S53 and S54 indicate that water inhibits the rate of DME formation at 415 K under all relevant methanol partial pressures (0.05-50 kPa) for both the associative (isolated H⁺ sites) and dissociative (paired H⁺ sites) pathways. The amount of water formed during methanol dehydration catalysis (415 K) when water is not intentionally co-fed (open points in Figures S53 and S54), however, is not enough to cause a *measurable* change in the rate of reaction, because of the low conversion in the differential regime. The origin of the approximately -1/3 water order measured under every condition studied at 415 K likely reflects a fractional coverage of water on H⁺ sites and further analysis is beyond the scope of this work.

Another potential source of the inhibition observed in CHA zeolites at high methanol pressures may be due to clustering of methanol around H⁺ sites, which solvate the proton away from the zeolite lattice.²³ Under steady-state methanol dehydration conditions (415 K, P_{CH3OH} = 0.05-22 kPa), IR spectra of H-CHA (0-44% paired Al) show a broad absorption band at ~3370 cm⁻¹ that increases with increasing CH₃OH pressure, which has been attributed to the formation of methanol clusters (Figures S40 and S41).²³ Features for methanol clusters are also present in MFI zeolites at high methanol partial pressures (>5 kPa CH₃OH), but do not give rise to inhibited dehydration rates at high methanol pressures (Figures S36-S38),¹¹ suggesting that certain structural features of the zeolite framework may stabilize the formation of these extended reactant structures within the pores.

The CHA framework is unique when compared to other zeolite frameworks studied for methanol dehydration (e.g. MFI, BEA, FAU, MOR, SFH, MTW, MTT) because it is a small-pore, window-cage framework that does not contain quasi-cylindrical pores. Instead, the CHA framework is comprised of 8-MR rings (0.38 nm in diameter) that limit diffusion of molecules into larger *chab*-cavities (0.73 x 1.2 nm), which may stabilize the formation of extended methanol structures under the reaction conditions studied. Methanol dehydration rates (per H⁺, 415 K) were measured on H-AEI zeolites (AEI framework; synthesis and characterization reported elsewhere),²⁴ which is another small-pore, window-cage framework that consists of 8-MR (0.38 nm) that limit diffusion into *aei*-cavities (0.73 x 1.0 nm), to investigate if the zeolite framework is responsible for this inhibition. DME formation rates (415 K, per H⁺) measured on H-AEI zeolites (Figure S55) show similar inhibition at high methanol partial pressures as observed for all CHA zeolites, indicating that such inhibition may reflect formation of methanol clusters inside the cavities of small-pore window-cage frameworks (e.g. CHA, AEI).

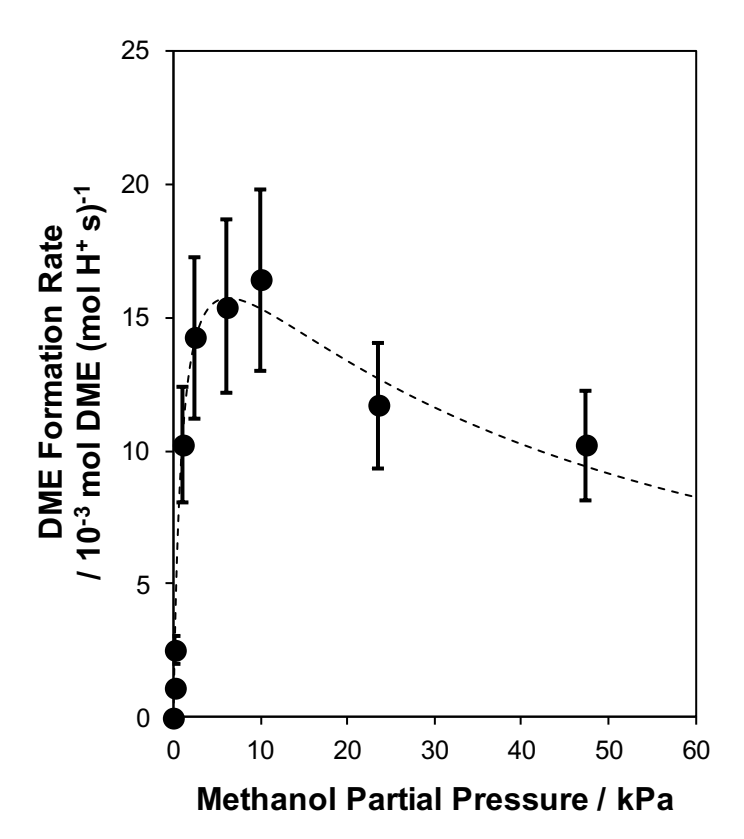


Figure S55. Methanol dehydration rates (per H⁺, 415 K) on H-AEI zeolite as a function of methanol partial pressure. Dashed line is a regression to the generalized rate expression (Eq. S35).

Section S.7. References

- (1) Di Iorio, J. R.; Gounder, R. Chem. Mater. 2016, 28, 2236-2247.
- (2) Camblor, M. A.; Villaescusa, L. A.; Díaz-Cabañas, M. J. *Top. Catal.* **1999**, *9*, 59-76.
- (3) Baerlocher, C.; McCusker, L. B. Database of Zeolite Structures. http://www.iza-structure.org/databases/ (2017)
- (4) Deimund, M. A.; Harrison, L.; Lunn, J. D.; Liu, Y.; Malek, A.; Shayib, R.; Davis, M. E. *ACS Catal.* **2015**, *6*, 542-550.
- (5) Zones, S. I. J. Chem. Soc., Faraday Trans. 1991, 87, 3709-3716.
- (6) Bates, S. A.; Delgass, W. N.; Ribeiro, F. H.; Miller, J. T.; Gounder, R. J. Catal. 2014, 312, 26-36.
- (7) Di Iorio, J. R.; Bates, S. A.; Verma, A. A.; Delgass, W. N.; Ribeiro, F. H.; Miller, J. T.; Gounder, R. *Top. Catal.* **2015**, *58*, 424-434.
- (8) Paolucci, C.; Parekh, A. A.; Khurana, I.; Di Iorio, J. R.; Li, H.; Albarracin Caballero, J. D.; Shih, A. J.; Anggara, T.; Delgass, W. N.; Miller, J. T.; Ribeiro, F. H.; Gounder, R.; Schneider, W. F. J. Am. Chem. Soc. **2016**, *138*, 6028-6048.
- (9) Carr, R. T.; Neurock, M.; Iglesia, E. J. Catal. 2011, 278, 78-93.
- (10) Jones, A. J.; Iglesia, E. Angew. Chem., Int. Ed. 2014, 53, 12177-12181.
- (11) Jones, A. J.; Carr, R. T.; Zones, S. I.; Iglesia, E. J. Catal. **2014**, *312*, 58-68.
- (12) Jones, A. J.; Zones, S. I.; Iglesia, E. J. Phys. Chem. C 2014, 118, 17787-17800.
- (13) Gounder, R.; Jones, A. J.; Carr, R. T.; Iglesia, E. J. Catal. 2012, 286, 214-223.
- (14) Salvador, P.; Kladnig, W. J. Chem. Soc., Faraday Trans. 1 1977, 73, 1153-1168.
- (15) Yamazaki, H.; Shima, H.; Imai, H.; Yokoi, T.; Tatsumi, T.; Kondo, J. N. *Angew. Chem., Int. Ed.* **2011**, *50*, 1853-1856.
- (16) Wang, W.; Buchholz, A.; Seiler, M.; Hunger, M. J. Am. Chem. Soc. 2003, 125, 15260-15267.
- (17) O'Malley, A. J.; Parker, S. F.; Chutia, A.; Farrow, M. R.; Silverwood, I. P.; Garcia-Sakai, V.; Catlow, C. R. A. *Chem. Commun.* **2016**, *52*, 2897-2900.
- (18) Krishna, R.; van Baten, J. M. *Langmuir* **2010**, *26*, 10854-10867.
- (19) Li, Z.; Navarro, M. T.; Martinez-Triguero, J.; Yu, J.; Corma, A. Catal. Sci. Technol. 2016, 6, 5856-5863.
- (20) Herrmann, C.; Haas, J.; Fetting, F. Appl. Catal. 1987, 35, 299-310.
- (21) Weisz, P.; Prater, C. Adv. Catal. 1954, 6, 143-196.
- (22) DeWilde, J. F.; Chiang, H.; Hickman, D. A.; Ho, C. R.; Bhan, A. ACS Catal. 2013, 3, 798-807.
- (23) Mirth, G.; Lercher, J. A.; Anderson, M. W.; Klinowski, J. J. Chem. Soc., Faraday Trans. **1990**, 86, 3039-3044.
- (24) Albarracin-Caballero, J. D.; Khurana, I.; Di Iorio, J. R.; Shih, A. J.; Schmidt, J. E.; Dusselier, M.; Davis, M. E.; Yezerets, A.; Miller, J. T.; Ribeiro, F. H.; Gounder, R. *React. Chem. Eng.* **2017**, *2*, 168-179.